"Turbulence Model Validation through Joint Experimental / Computational Studies of Separated Flow Over a Three-Dimensional Tapered Bump"

ONR Contract Number N00014-20-2-1002
NASA Contract Number 80LARC21T0001

A Final Report

Part II – Computational Investigation

Prepared by Matthew Lakebrink, PhD

Boeing Research & Technology

August, 2023

Contents

1) **Overview** 3

2) **Empty-Tunnel Simulations** 4

a) **Geometric Model** 5

b) **Comparisons Between Empty-Tunnel Measurements and CFD** 8

3) **Exploring Best Practices and Flow Physics with Splitter Plate and Bump** 11

a) **Steady-State RANS Analysis** 11

b) **Time-Accurate RANS/LES Analysis** 21

4) **Comparisons with Particle Image Velocimetry (PIV) Measurements** 32

5) **Comparisons with Oil-Film Interferometry (OFI) Measurements** 36

6) **Comparisons with Hot-Wire Measurements** 42

7) **Comparisons with Surface-Pressure Measurements** 46

8) **Comparisons with Laser Doppler Velocimetry (LDV) Measurements** 52

9) **Embedded Shear-Layer Scaling** 59

10) **Potential Impact of Hotwire Apparatus on Measured Velocity** 60

11) **References** 63

1) Overview

This report serves as documentation of activities related to Computational Fluid Dynamics (CFD) analysis applied to the Smooth Body Separation Experiment designed to produce validation-quality experimental data from wind-tunnel tests performed at the University of Notre Dame. The test article is a simple bump shape defined analytically by

$$y(x,z) = h\ \frac{1+erf\left(\left(\frac{L}{2}-2z_0-|z|\right)/z_0\right)}{2}\ exp\left(-\left(\frac{x}{x_0}\right)^2\right) \qquad \text{(Equation 1)}$$

where h is the bump height in the wall-normal, or 'y' direction, x_o is the streamwise length of the bump, z_o is the spanwise length of the bump, and L is the test-section width. For the present study $h = 0.085L$, $x_o = 0.195L$, $z_o = 0.06L$, and L is 36 inches, which results in the shape depicted in Figure 1.

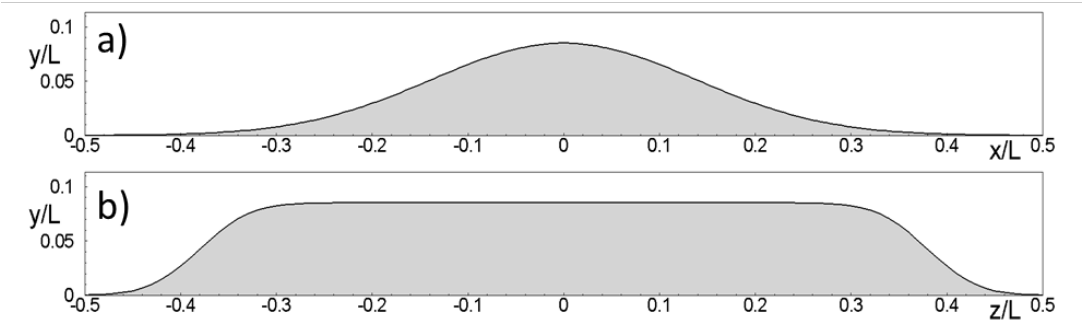

Figure 1: a) side view and b) front view of test article. Symmetry plane at z/L=0, side walls at z/L=+/-0.5.

All CFD analysis utilized the Boeing CFD (BCFD[1]) flow solver. BCFD was used to analyze flow over the Boeing Speed Bump with second-order accuracy in space and time. Inviscid fluxes were computed using the HLLE scheme for steady-state simulations, and the Low-Dissipation Roe scheme for time-accurate simulations. The working fluid was modeled as calorically perfect air using Sutherland's law for viscosity. Thermal diffusivity was determined by assuming a constant molecular Prandtl number of 0.72, and a turbulent Prandtl number of 0.9. Reynolds Averaged Navier-Stokes (RANS) simulations were conducted using the one-equation Spalart-Allmaras turbulence model[2] with rotation correction[3] and the quadratic constitutive relation[4] (SA-RC-QCR), as well as Menter's two-equation, Shear-Stress Transport (SST[5]) model. Time-accurate computations were conducted using Delayed Detached eddy Simulation (DDES[6]) with the one-equation RANS model, and Large Eddy Stress balance (LESb[7]) with the two-equation RANS model. Implicit dual-time stepping was used to achieve second-order temporal accuracy. The experimental investigation conducted during the course of this study is described in detail in an accompanying report.

ONR Contract Number N00014-20-2-1002

Unless otherwise noted, the computational domain used to simulate flow over the bump consisted of the wind-tunnel contraction, test section, test article, splitter plate, and supporting

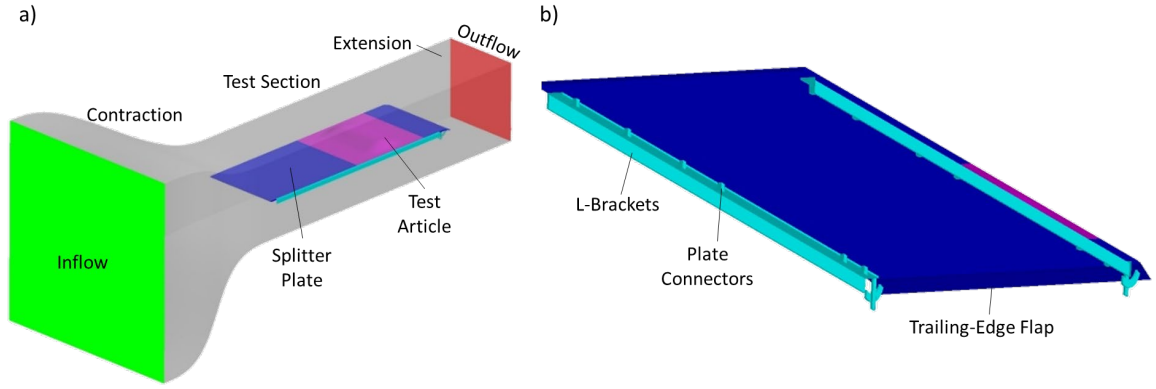

Figure 2: a) Key elements of the computational domain used for CFD simulations, with the bump located at the aft-most mounting position. b) Details of the geometric fidelity included below the splitter plate.

hardware beneath the plate (Figure 2). The cross section of the test section measures 36" by 36", and the splitter plate is positioned such that its upper surface is located 18" from the top and bottom walls. A 36" extension was also included to isolate the outflow boundary condition from the downstream end of the test section.

In order to explore sensitivity to Reynolds number for a particular test-section Mach number, the splitter plate is configured to support mounting the bump at three positions, denoted 'forward', 'middle', and 'aft' in Figure 3a. Figure 3b gives the distance from the leading edge of the splitter plate to the leading edge, apex, and trailing edge of the bump for each mounting location. An alternate forward-bump location with the apex positioned at 36" was also used to provide data

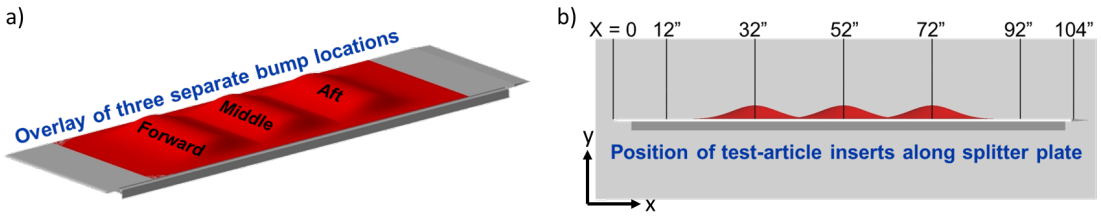

Figure 3: a) Isometric view of the splitter plate simultaneously depicting the three possible mounting locations for the bump. b) Key distances from splitter leading edge for three bump-mounting locations.

for consistent comparison with other experimental and numerical studies.

2) Empty-Tunnel Simulations

RANS CFD analysis of the empty tunnel was motivated by two primary objectives: first, it was necessary to establish a best practice for simulating the empty facility to serve as a good foundation for subsequent simulations with the splitter and bump installed, and second, for comparison with corresponding wind-tunnel measurements. Toward the first objective, sensitivities to grid resolution, grid topology, geometric model, and turbulence model were explored. The first part of this section will look at these sensitivities and the resulting best

ONR Contract Number N00014-20-2-1002

practices for simulating the empty wind tunnel, and the second part will focus on application of the best practices to a comparison between CFD and wind-tunnel measurements.

a) Geometric Model

The first attempt at simulating the empty tunnel included the contraction, test section, and diffuser. Total pressure and total temperature values of 14.33 psi and 533.6 R were prescribed at the inflow boundary. A mass-flow-rate sweep was simulated by setting the outflow boundary condition to uniform pressure at five equally spaced values ranging from 14.11 psi to 14.31 psi, which corresponds to test-section Mach numbers ranging from ~0.05 to ~0.25. Simulations were carried out using two different grid-resolution levels as described in Table 1. The 'Total Cells' and 'Total Points' columns are the total number of those respective elements in the entire computational domain. The 'Points Along One Edge' column represents the number of points placed along one of the four edges of the perimeter of the tunnel cross section. The 'Initial Wall-Normal Spacing' is the distance between the surface and the first point normal to the surface used to construct layers of anisotropic cells that resolve near-wall gradients.

Table 1: Resolution for two grids used to assess the geometric model consisting of contraction, test section, and diffuser.

Grid Name	Total Cells	Total Points	Points Along One Edge	Initial Wall-Normal Spacing [in]
N050	18,871,126	8,452,397	50	2e-4
N100	87,169,832	33,369,120	100	2e-4

Mach-number contours at several x-planes throughout the computational domain are shown in Figure 4. The images are arranged as follows: the top row shows results for the lowest flow rate (outflow pressure 14.31 psi) and the bottom row shows results for the highest flow rate (outflow pressure 14.11 psi); the left group of four images is was obtained with the SA turbulence model and the right group was obtained with the SA-RC-QCR turbulence model; finally, the left column in each group of four images is from the N050 grid, and the right column is from the N100 grid.

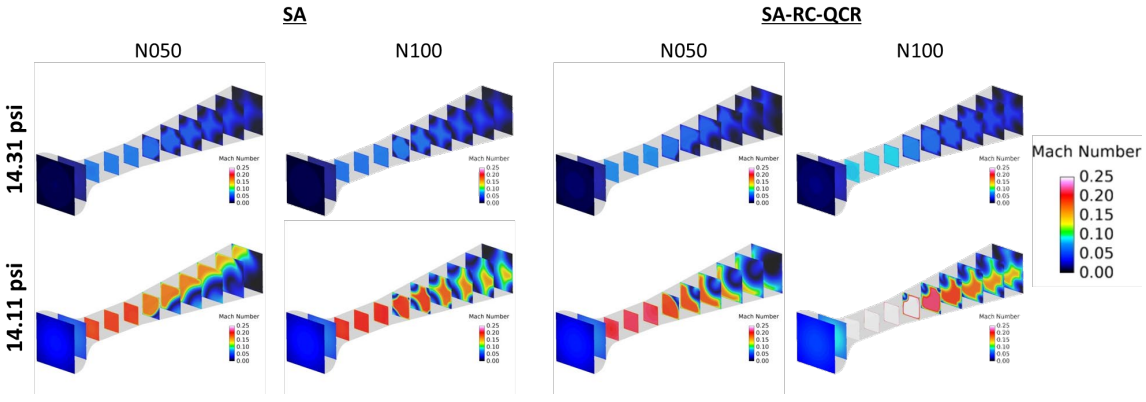

Figure 4: Mach-number contours throughout the domain for both grid resolutions at the lowest and highest flow rates. Results shown for both SA and SA-RC-QCR turbulence models.

Flow through the facility is observed to be well behaved through the test section, but in the diffuser large-scale corner flows develop. In general, the corner flows appear to become more

ONR Contract Number N00014-20-2-1002

symmetric with increasing grid resolution for the lowest flow rate, but at the highest flow rate significant asymmetry is observed for both grids. As one would expect, the size and shape of the corner flows is observed to be sensitive to whether QCR is used, which is most clearly evident in Figure 4 when comparing the N100 grid at 14.31 psi between the SA and SA-RC-QCR turbulence models. Simulations were also carried out using SST and SST-QCR with similar sensitivities to those observed for SA and SA-RC-QCR. The most important summary observation from these initial simulations is that the corner flows that develop in the diffuser hamper solution convergence and introduce unwanted sensitivities to what should be a simple and well behaved flow. This is made very clear in Figure 5 which quantitatively summarizes the

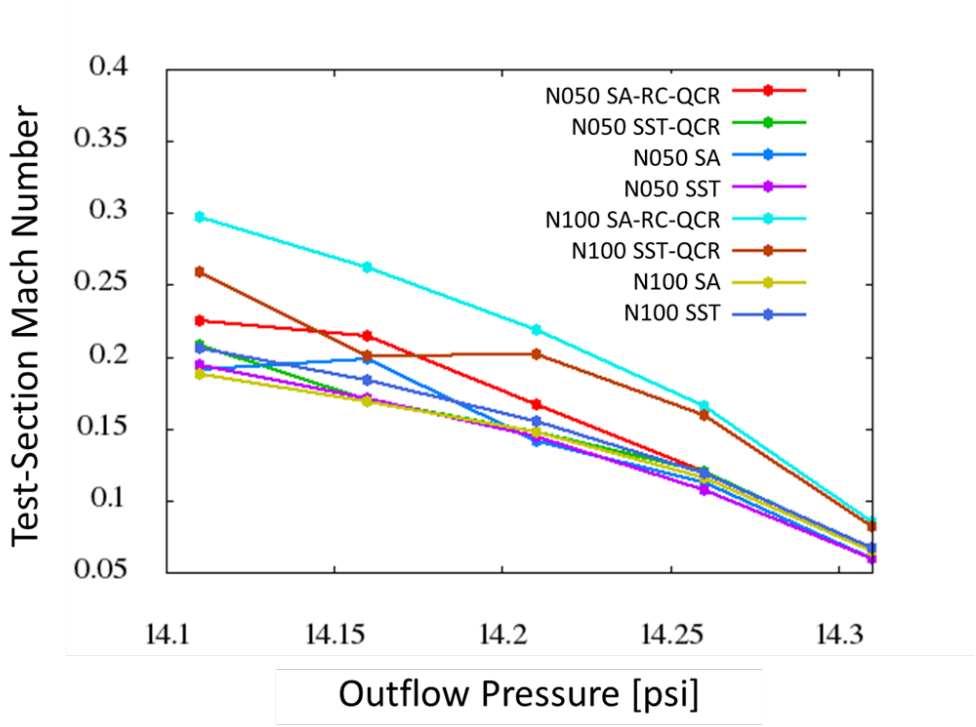

Figure 5: Sensitivity of test-section Mach number to grid resolution and turbulence model for the computational domain including the diffuser.

variation in test-section Mach number for various combinations of grid resolution and turbulence model. Each curve comprises five points corresponding to five different outflow-plane pressures, and the same group of five pressures ranging from 14.11 psi to 14.31 psi are used for each curve. Therefore, it can be seen that for a particular outflow pressure, the resulting test-section Mach number is extremely sensitive to grid resolution and turbulence model. The primary source of this sensitivity is the variation in how the diffuser corner flows develop and introduce total-pressure losses.

In an effort to eliminate the sensitivities introduced by the diffuser corner flows, a computational domain consisting of the contraction, test section, and a 36” extension to the test section was created. Two grids analogous to those used for the domain including the diffuser were generated and the resulting grid-resolution information is presented in Table 2.

Table 2: Resolution for two grids used to assess the geometric model consisting of contraction and test section.

Grid Name	Total Cells	Total Points	Points Along One Edge	Initial Wall-Normal Spacing [in]
N050r1	9,195,556	3,873,425	50	2e-4
N100r1	45,342,637	15,962,062	100	2e-4

The same outflow-pressure sweep was conducted on these grids as for those including the diffuser, and the resulting Mach-number cuts are shown in Figure 6, which reveals that not only that the flow is well behaved throughout the domain, but that there are no qualitative sensitivities to grid resolution or turbulence model, over the range of these parameters considered. Quantitative verification of this observation is shown in Figure 7, where for a particular outflow

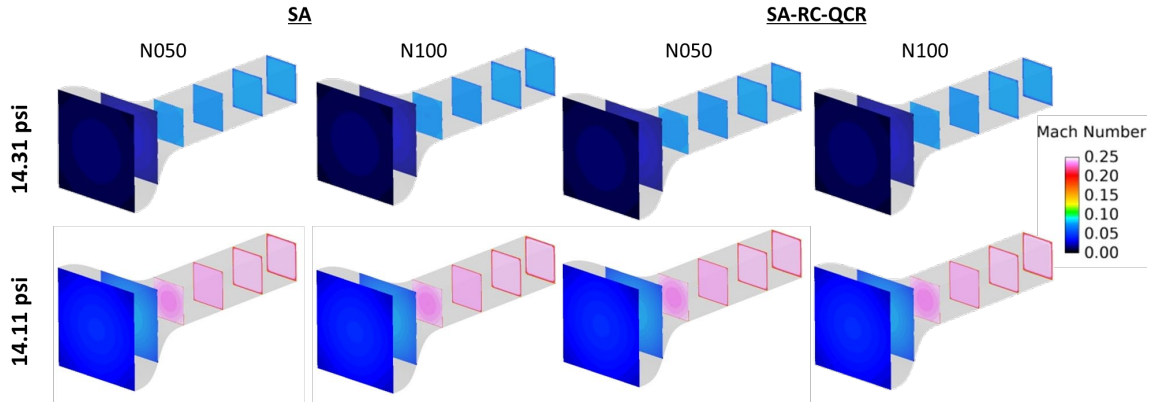

Figure 6: Mach-number contours throughout the 'no-diffuser' domain for both grid resolutions at the lowest and highest flow rates. Results shown for both SA and SA-RC-QCR turbulence models.

pressure, all combinations of grid resolution and turbulence model collapse to the same Mach number. Based on these results, the best practice for geometric modeling of the empty tunnel was determined to be a computational domain consisting of the contraction, test section, and a straight extension between the downstream end of the test section and the outflow plane.

The foregoing simulations were conducted on grids generated in AFLR[9] using a surface mesh comprising nominally isotropic triangles. AFLR advances the triangular faces into the volume to create layers of triangular prisms which are initially highly anisotropic in the wall-normal direction to capture near-wall gradients. The wall-normal spacing of the prisms grows at a rate of not more than 15% until the prisms are approximately isotropic, at which point tetrahedral elements are used to fill the remaining interior portion of the domain. In addition to this grid topology, simulations using grids comprising only hexahedral elements (quadrilateral faces on the surface) were performed. The hexahedral grids were generated to closely approximate the spacings used for the N100 AFLR grids, and simulated using the same four turbulence models (i.e., SA, SA-RC-QCR, SST, and SST-QCR). The results obtained using hexahedral grids were in very good agreement with those obtained on the AFLR grids. Based on this, and due to the relative simplicity and efficiency of generating AFLR grids compared to hexahedral grids, particularly with increasing geometric complexity, it was determined that further analysis in Year 1 would be focused on simulations using AFLR grids. Depending on results from detailed

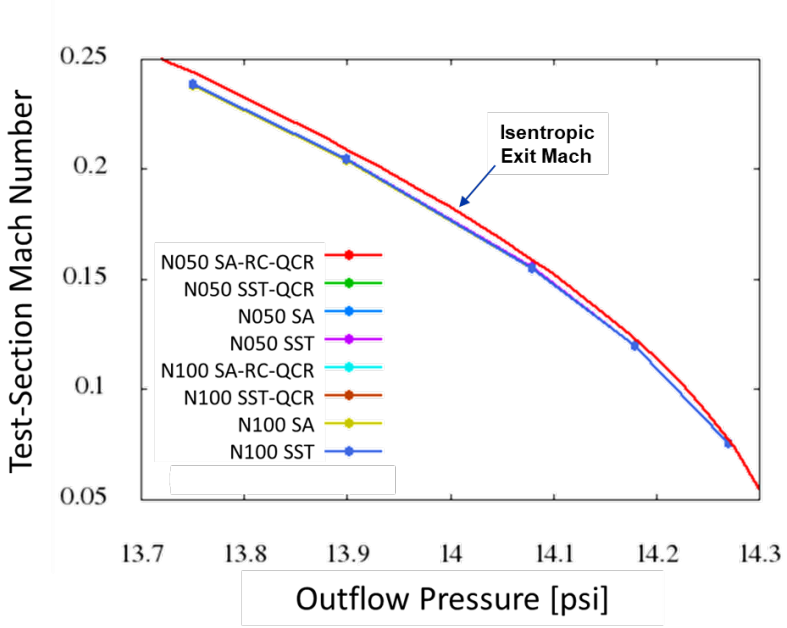

Figure 7: Sensitivity of test-section Mach number to grid resolution and turbulence model for the computational domain with a straight extension.

comparisons between test and CFD to be performed in Year 2, especially for time-accurate, hybrid RANS/LES simulations including the bump, hexahedral mesh topology may be revisited.

b) Comparisons Between Empty-Tunnel Measurements and CFD

Boundary layer profiles from each wall of the empty-tunnel test section were compared between

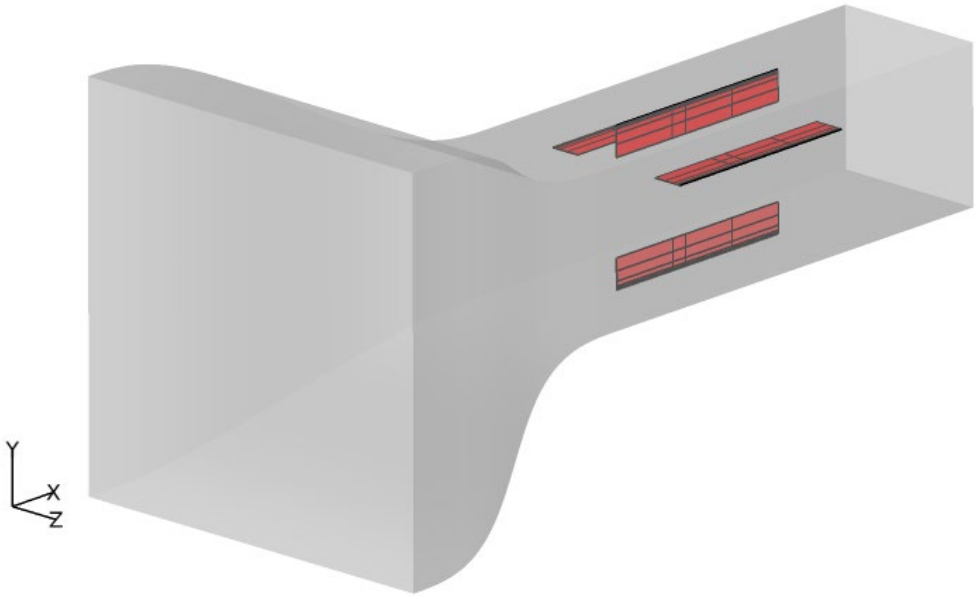

Figure 8: Boundary-layer rake locations used for comparisons between empty-tunnel test and CFD.

total-pressure probe measurements and CFD for a test-section Mach number of approximately

0.2. Total pressure and total temperature values of 14.4 psi and 550 R were prescribe at the inflow boundary, and an outflow-boundary pressure of 13.99 psi was prescribed for the CFD simulations. Comparisons were made at four streamwise locations for each of the four test-section walls. The rakes, shown in Figure 8, on the top and bottom walls are located at z=0, and the rakes on the sidewalls are located 27" from the floor. Streamwise locations of the rakes are

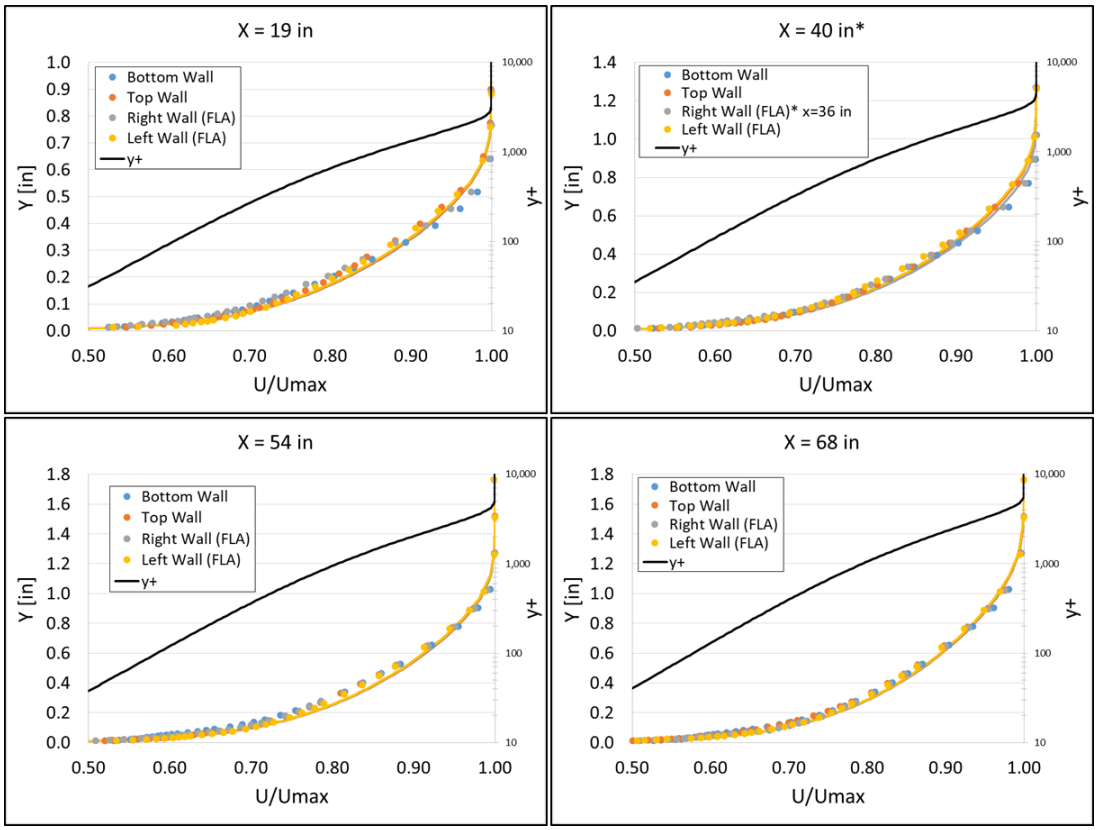

Figure 9: Comparison of velocity profiles between test (symbols) and SA-RC-QCR CFD (lines) on the left axis, and corresponding y+ on the right axis at four streamwise locations in the test section. 'Left' and 'Right' wall designations are Forward Looking Aft (FLA), i.e., looking in the +x direction.

nominally 19", 40", 54", and 68" from the entrance of the 108"-long test section, except for the second streamwise position on the right-sidewall rake, forward looking aft (FLA), which is located at 36".

Comparisons using the SA-RC-QCR turbulence model are shown in Figure 9. Excellent agreement between test and CFD is observed for the empty-tunnel boundary layers on all four walls at each streamwise location. The lower limit on the horizontal axes was chosen to begin just before the experimental measurement point closest to the wall. Computed values of y+, plotted on the right axis, indicate that the pitot-probe measurements begin at y+ ~30-40 across the range of x-stations plotted.

A similar comparison using the SST-QCR turbulence model is shown in Figure 10. Once again, excellent agreement is observed between test and CFD. When comparing SA-RC-QCR to SST-

QCR there are only very subtle differences, but it does appear that SST-QCR does a somewhat better job of fitting the experimental data, particularly near the outer edge of the boundary layer.

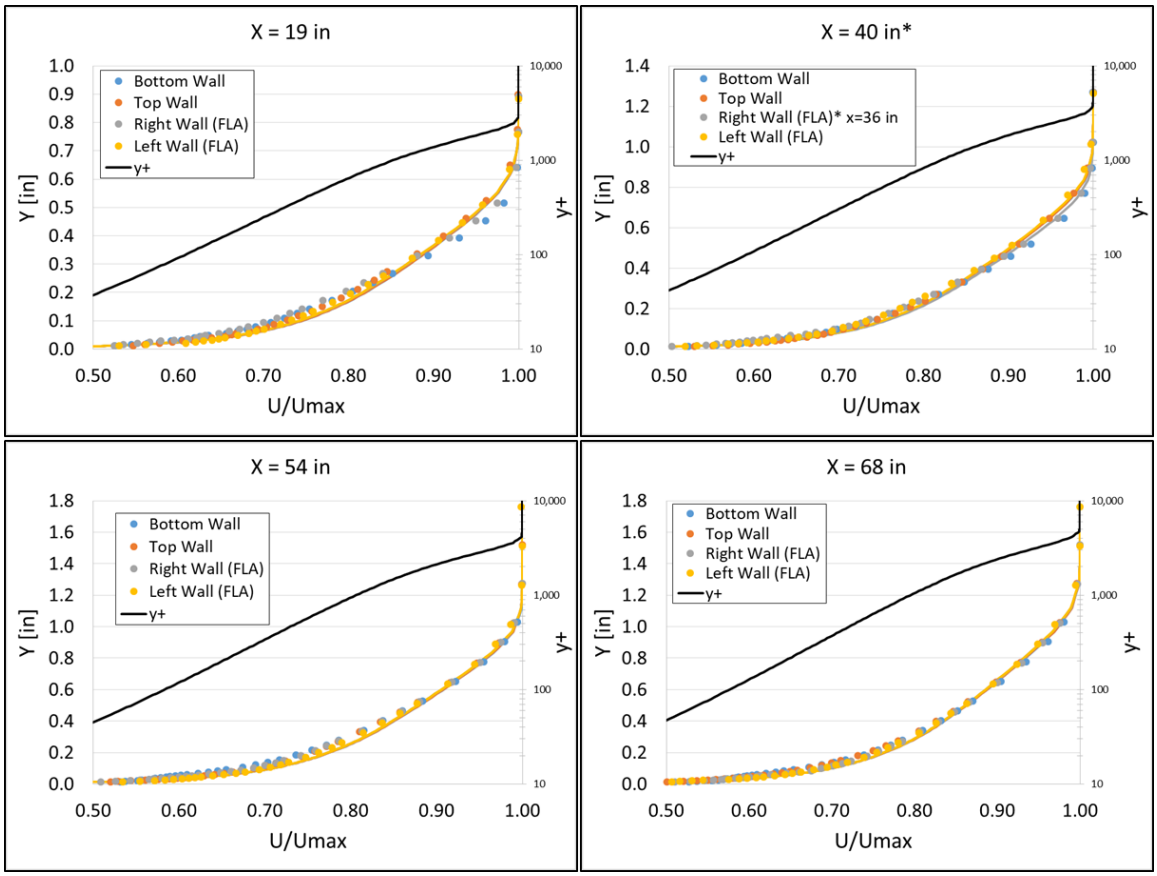

Figure 10: Comparison of velocity profiles between test (symbols) and SST-QCR CFD (lines) on the left axis, and corresponding y+ on the right axis at four streamwise locations in the test section. 'Left' and 'Right' wall designations are Forward Looking Aft (FLA), i.e., looking in the +x direction.

The foregoing velocity profiles were integrated to obtain the variation in displacement thickness throughout the test section, and the associated comparison between test and CFD is show in Figure 11. Overall agreement between test and CFD, both in terms of magnitude and growth rate of displacement thickness, is very favorable. Performing linear extrapolation of the data presented in Figure 11, the displacement thickness at the end of the test section (x = 108") is expected to be approximately 0.23", which provides some confirmation that sidewall boundary layers and associated corner flow, even for the aft-most bump position, will not interfere with the separation and reattachment over the bump. This comparison also helps verify that CFD is able to reproduce the naturally occurring

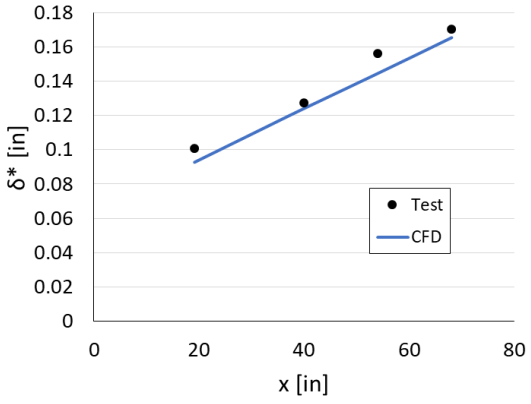

Figure 11: Displacement thickness growth through the empty-tunnel test section.

ONR Contract Number N00014-20-2-1002

streamwise pressure gradient that will be experienced by the bump, which is essential for subsequent successful validation of separation/reattachment locations, and wake-vortex development.

3) Exploring Best Practices and Flow Physics with Splitter Plate and Bump

CFD Analysis of flow over the splitter plate and bump test article utilized the geometric components shown in the computational-domain diagram in Figure 2. Sensitivities to grid resolution, turbulence model (SA-RC-QCR and SST-QCR with both RANS and hybrid RANS/LES), test-section Mach number (0.05 to 0.5), and bump location (forward to aft) were investigated. For all forward-bump results in this section, the bump apex was located at 32" downstream of the leading edge of the splitter plate. Prior to analysis of these sensitivities, it was necessary to calibrate the flap at the trailing edge of the splitter plate to obtain alignment of the stagnation line at the leading edge of the splitter plate. This section will address each of these activities, first looking at results from the steady-state RANS simulations, and then analogous results from time-accurate RANS/LES.

a) Steady-State RANS Analysis

Calibration of the trailing-edge flap was performed using the SA-RC-QCR turbulence model with total pressure and total temperature of 14.33 psi and 533.6 R prescribed at the inflow boundary. Flow rate through the test section was varied by prescribing pressures at the outflow plane ranging from 13.1 psi up to 14.3 psi. The flap was simulated at three positions starting with 16.8-degrees downward, then 8-degrees downward, and finally positioned neutrally (0 degrees). Results from the flap positioned 16.8-degrees downward are shown in Figure 12. In

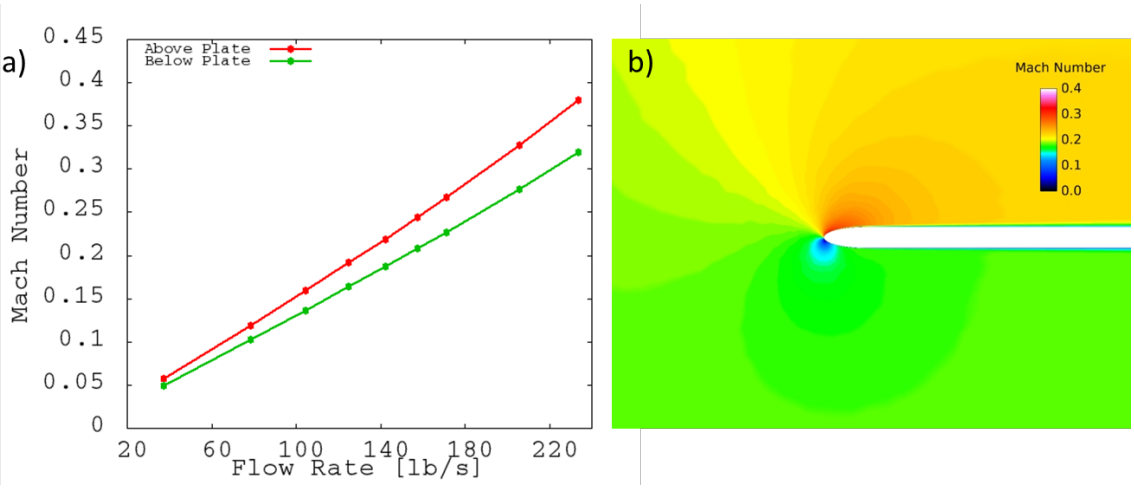

Figure 12: a) Mach numbers above and below the plate for a range of flow rates and b) Mach-number contours on the center plane of the plate leading edge. Flap down 16.8 degrees.

Figure 12a, the probe used to report Mach number above the plate was located at (x,y,z) = (14.5, 30, 2)", and Mach number below the plate was reported at (x,y,z) = (10, 9, 0)", where (x,y,z) = (0, 0, 0) is located on the floor and at the centerline entrance to the test section. It is observed that the Mach numbers above and below the plate diverge from one another with increasing flow rate, which indicates that the stagnation line is misaligned with the leading edge. This

misalignment is represented in Figure 12b where Mach-number contours at the leading-edge center plane for a flow rate of ~143 lb/s show the stagnation region located below the leading edge, which indicates that downward deflected of the trailing-edge flap is too severe, and should be lessened.

Based on these results, the downward flap angle was reduced to 8 degrees and the single flow-rate of ~143 lb/s was simulated. Results from this simulation (Figure 13) indicate that the Mach numbers above and below the plate are closer than they were for 16.8-degrees deflection, but still not close enough to achieve satisfactory alignment between the stagnation line and plate leading edge.

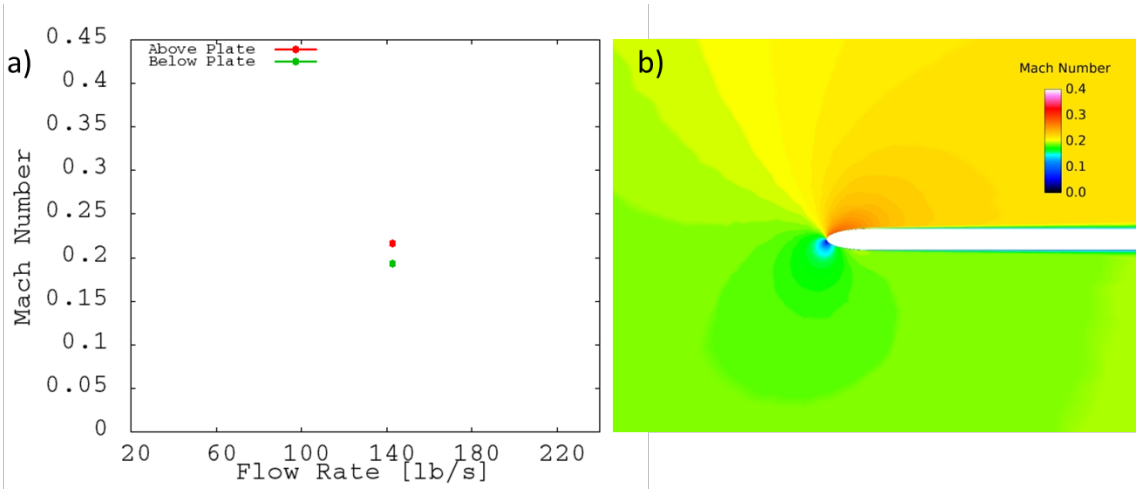

Figure 13: a) Mach numbers above and below the plate for one flow rate and b) Mach-number contours on the center plane of the plate leading edge. Flap down 8 degrees.

Given the position of the stagnation line in Figure 13b, the flap angle was further reduced to zero degrees, and simulations were carried out for three flow rates corresponding to outflow pressures of 13.5 psi, 13.9 psi, and 14.3 psi. Results for the neutral-flap flow-rate sweep are shown in

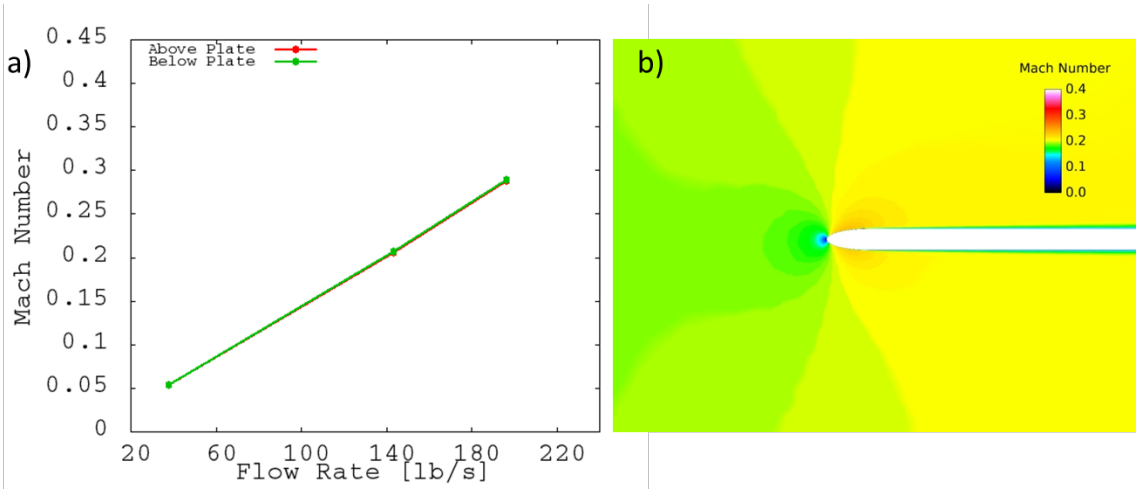

Figure 14: a) Mach numbers above and below the plate for a range of flow rates and b) Mach-number contours on the center plane of the plate leading edge. Zero-degree flap deflection.

Figure 14. Mach numbers above and below the plate are observed to collapse to nearly identical values across the flow rate, and corresponding Mach-number contours at ~143 lb/s confirm that the stagnation line is aligned very closely with the leading edge. Downstream of the leading edge, the boundary layers on the upper and lower surfaces of the plate are observed to grow in a qualitatively uniform way. These results for the neutrally positioned flap indicate that the losses introduced by the bump-induced separation above the plate very closely match the losses introduced by the L-beams, plate connectors, and flap mechanization below the plate. For this calibration exercise, the bump was located in the aft position. It is assumed that variation in losses introduced by the bump, and therefore stagnation-line location will not be significantly sensitive to the bump location or grid resolution, so the neutral flap position is utilized for all remaining simulations unless otherwise noted.

Following successful calibration of the trailing-edge flap, sensitivity to grid resolution was assessed with the bump located in the aft position. Resolution sweeps were performed using both SA-RC-QCR and SST-QCR turbulence models. Total pressure and total temperature values of 14.33 psi and 533.6 R were prescribed at the inflow boundary. Flow rate through the test section was varied by prescribing pressures of 13.5 psi, 13.9 psi, and 14.3 psi at the outflow plane. Five resolution levels, summarized in Table 3, were obtained by subsequently refining the test article beginning at the leading edge of the bump insert and extending downstream of the bump to the trailing edge of the plate. All other portions of the grid were held constant at the coarse-grid spacings.

Table 3: Metrics for five grids used in the RANS resolution study with the bump in the aft position

	Coarse	Medium	Fine	X-Fine	XX-Fine
Total Elements	38,223,780	45,577,065	68,631,809	130,998,507	312,648,878
Bump Spacing [in]	0.5	0.25	0.125	0.0625	0.03125

Each grid was used to simulate the entire flow-rate sweep except for the XX-Fine mesh, which was only used to assess the highest flow rate (i.e., 13.5 psi outflow pressure). Integrated loads computed using the SA-RC-QCR turbulence model for each grid except the XX-Fine mesh are shown at each flow rate in Figure 15. Fx and Fy in the y-axis titles denote loads in the x and y directions, respectively, as depicted in Figure 3. The '-p' and '-v' designators in the y-axis titles denote pressure and viscous loads, respectively. These results indicate that only Fx-p is sensitive to grid resolution for the SA-RC-QCR turbulence model.

Similar results for the SST-QCR turbulence model are shown in Figure 16, where it is observed that like SA-RC-QCR the Fx-p load is most sensitive to grid resolution. Another similarity between the two models is that Fx-p becomes increasingly sensitive to grid resolution with increasing flow rate. This is likely due to an increase in the severity of separation over the bump as flow rate increases. Unlike SA-RC-QCR, however, SST-QCR exhibits slight sensitivity to grid resolution in Fx-v and Fy-v. It is also observed that Fx-p is significantly more sensitive to grid resolution with SST-QCR than SA-RC-QCR, particularly on the coarser end of the resolution spectrum.

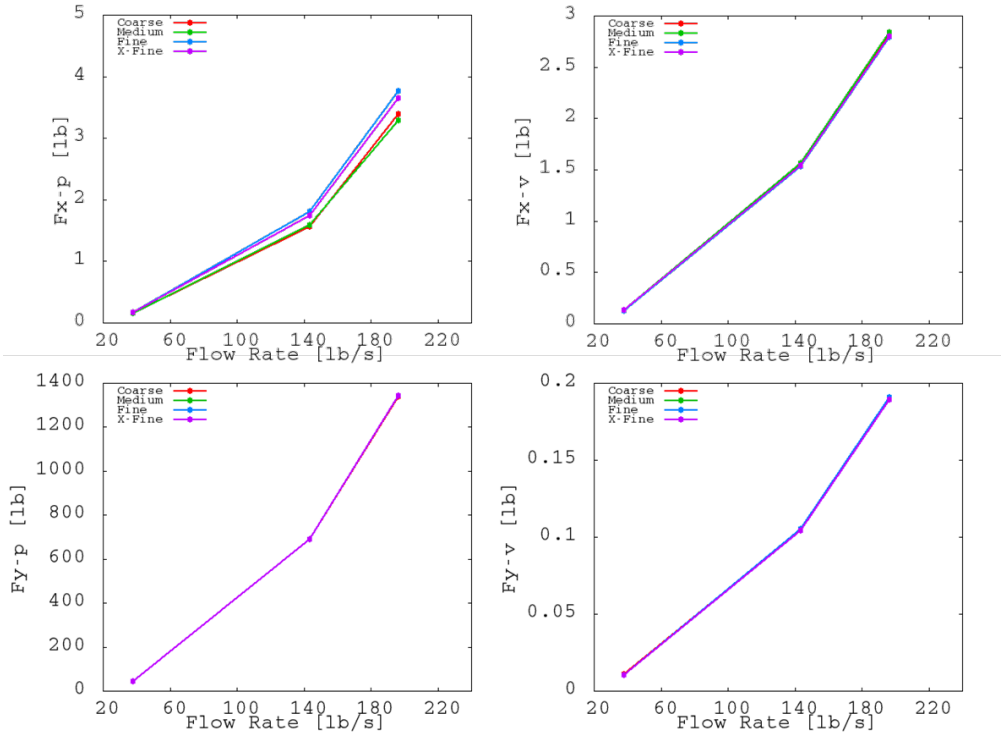

Figure 15: Pressure (-p) and viscous (*-v) loads on the bump in x and y directions for various grids resolutions and flow rates using the SA-RC-QCR turbulence model.*

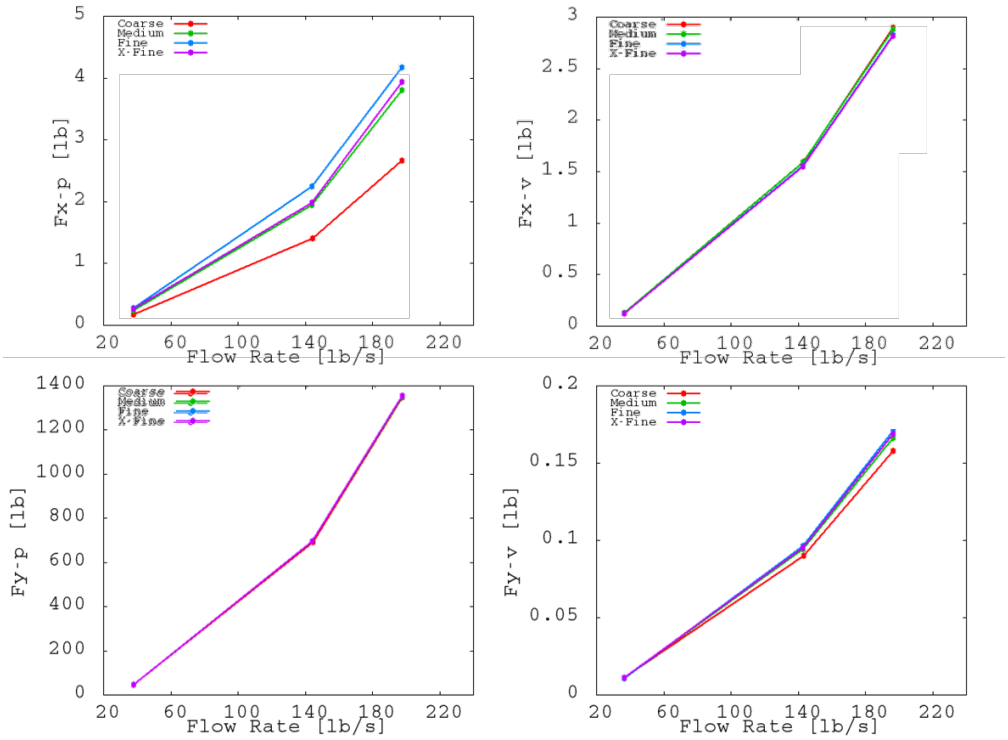

Figure 16: Pressure (-p) and viscous (*-v) loads on the bump in x and y directions for various grids resolutions and flow rates using the SST-QCR turbulence model.*

Focusing on highest flow rate, since that is where the greatest grid-resolution sensitivity was observed, Figure 17 looks at grid convergence for each load component using both SA-RC-QCR

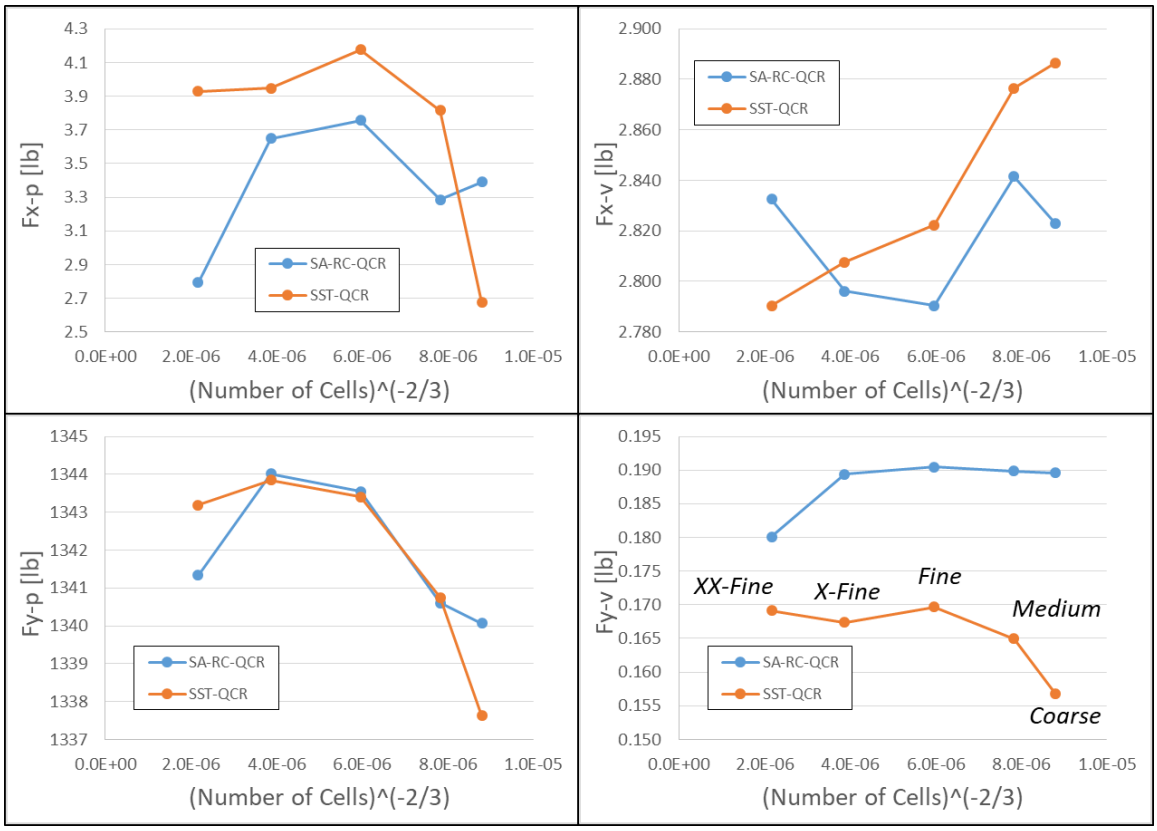

Figure 17: Grid convergence for 13.5 psi outflow pressure with SA-RC-QCR and SST-QCR.

and SST-QCR turbulence models. Grid resolution increases from right to left, as denoted in the Fy-v plot. Both turbulence models appear to be approaching near grid independence by the X-Fine mesh, and both models predict clearly different loads at this level of resolution, except for Fy-p which only differs slightly between the two models. Trends in load convergence continue in an unsurprising manner for SST-QCR when the resolution is increased from X-Fine to XX-Fine, however, SA-RC-QCR exhibits a sharp break in the trend for all loads.

The cause of this was traced back to the way near-wall prism stacks were generated. As shown in Figure 19a-c, the prism-stack height, represented by the vertical green bars in each image, reduces by roughly a factor of two with each increase in grid resolution. This corresponds to the factor-of-two reduction in surface-mesh spacing with each increasing level of grid resolution. In the fine mesh, all but the very outermost portion of the boundary layer is captured by the prisms. The percent of boundary layer resolved by prisms in the X-Fine and XX-Fine meshes drops to less than 50% and less than 25%, respectively. The impact this has on the flow solution is shown in Figure 19d-f, where a broad layer of poorly resolved, increased modeled turbulence (mut/mul) develops, which corresponds to a delay in separation location for the XX-Fine mesh relative to the Fine and X-Fine meshes. It is expected that this turbulence peak would be less diffuse and more focused about a particular distance from the wall.

ONR Contract Number N00014-20-2-1002

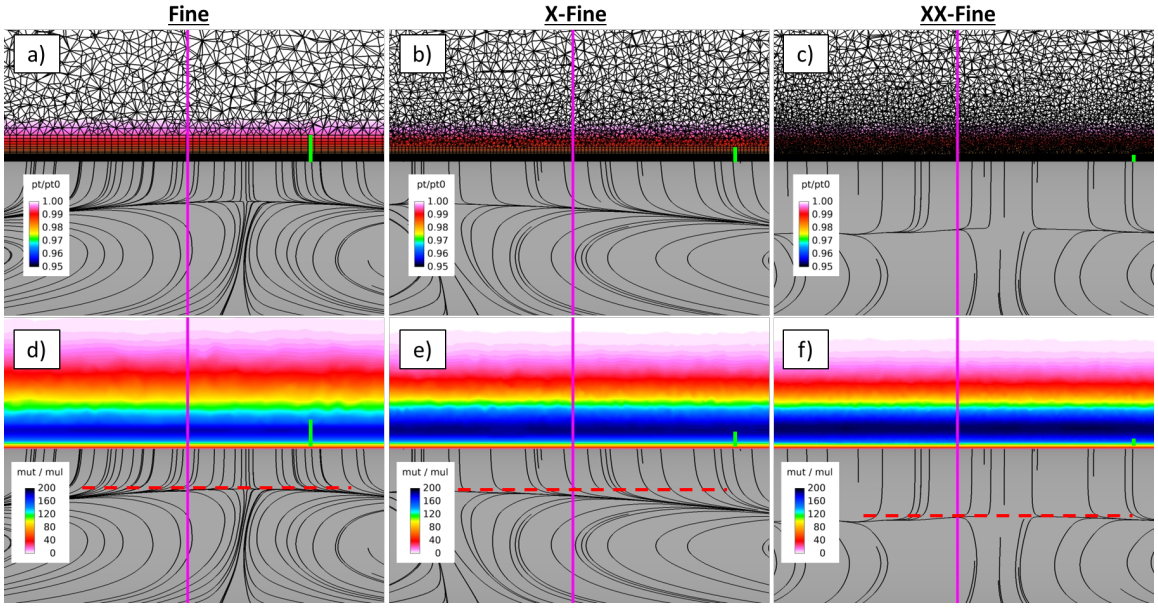

Figure 19: Impact on prism-stack height and total-pressure ratio (pt/pt0) (a-c), and turbulent viscosity normalized by molecular viscosity (mut/mul) (d-f) at the bump apex for the Fine (a,d), X-Fine (b,e), and XX-Fine (c,f) meshes using SA-RC-QCR. Purple lines represent the centerline, and green lines indicate the prism-stack height for each grid level (a-c). Dashed red lines show upstream-most separation location.

To address this issue, the Fine through XX-Fine meshes were regenerated such that the prism stack height met or exceeded the boundary layer thickness. This was accomplished by activating global prism-stack termination in AFLR by setting the parameter 'mblend' equal to one. The resulting grid and associated impact on the solution is shown for the XX-Fine mesh in Figure 18. The prism stacks are observed to reach isotropy near the same height, but rather than terminating they continue to generate isotropic prisms to just beyond the boundary-layer thickness. The resulting turbulent viscosity contains a greater and more tightly focused peak with mblend=1 than was observed without. Additionally, the leading edge of the separation

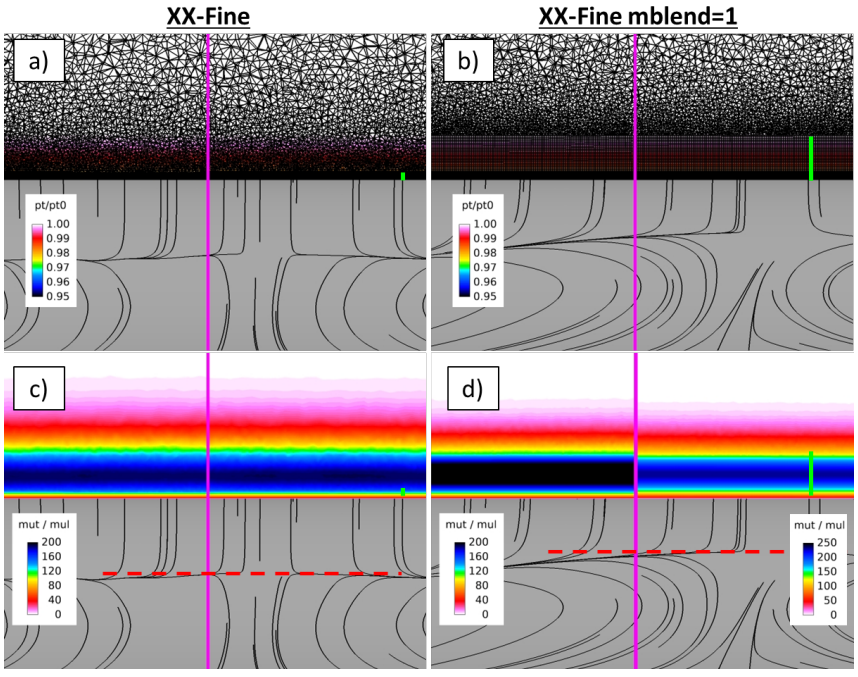

Figure 18: Impact of setting AFLR parameter mblend=1 on both prism stack height (a vs b) and modeled turbulence (c vs d). Note: different scale limits are used on each half of image d.

ONR Contract Number N00014-20-2-1002

front is observed to move upstream to a location very near what was predicted with the fine grid, where the majority of the boundary layer was resolved within the prism stack.

Grid-convergence plots including results from the three grids generated with mblend=1 are given in Figure 20. Based on these results, it was determined that an acceptable balance between grid convergence and number of elements (i.e., solution time, particularly for time-accurate simulations) is achieved with the X-Fine mesh, which was used for subsequent simulations investigating bump flow physics both with RANS and hybrid RANS/LES methods.

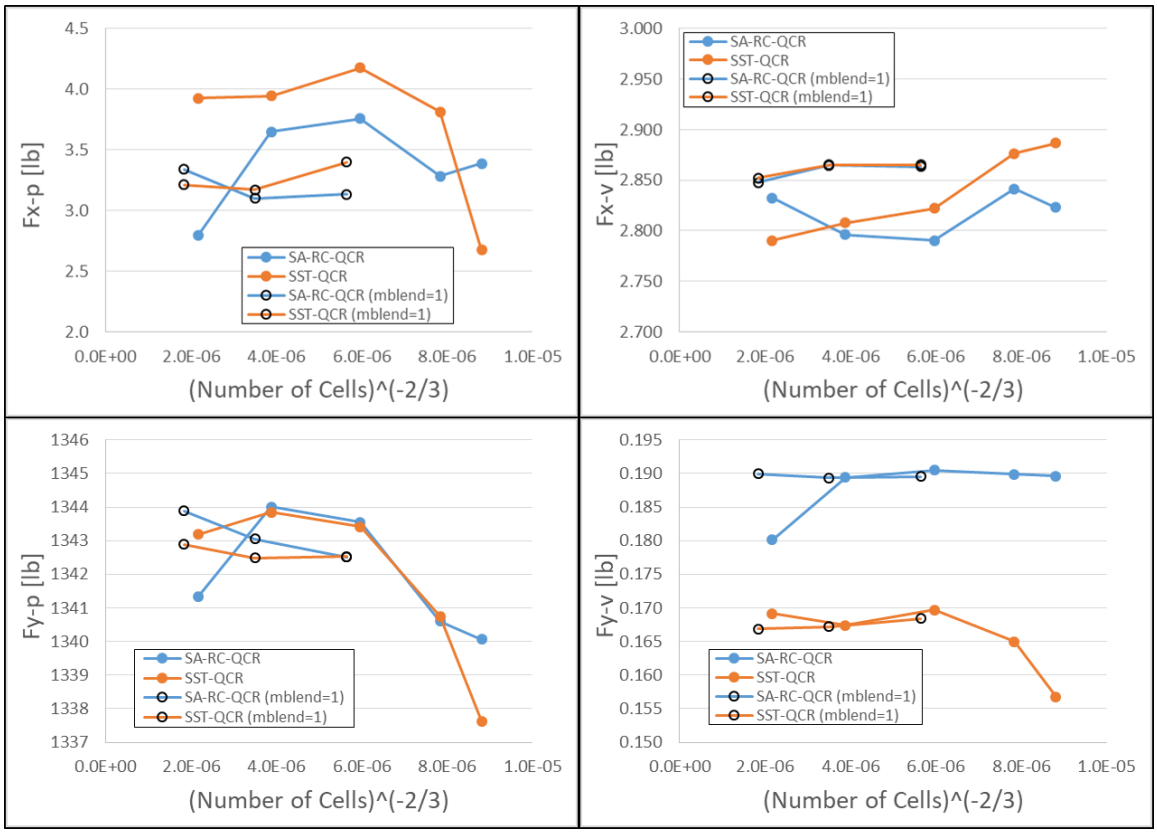

Figure 20: Grid convergence for 13.5 psi outflow pressure with SA-RC-QCR and SST-QCR.

Prior to starting time-accurate simulations, sensitivity of the flow predicted using RANS, and in particular the SST-QCR turbulence model, was assessed considering various bump locations and test-section Mach numbers. These simulations were performed on the X-Fine mesh (mblend=0) with inflow total pressure and total temperature equal to 14.33 psi and 533.6 R. The range of test-section Mach numbers was achieved by setting the outflow pressure to 14.3 psi, 13.5 psi, or 12 psi which resulted in test-section Mach numbers of roughly 0.05, 0.3, or 0.5, respectively. All three Mach numbers were considered for each of the three bump locations depicted in Figure 3.

Planform views of the bump test article from each of the nine simulations are shown in Figure 21. Surface streamlines are computed using the skin-friction vector, the surface is colored by the x-component of skin friction (Cfx), and flow is from left to right. Several similarities exist in the physics predicted by SST-QCR over the range of conditions explored. All nine flow fields

ONR Contract Number N00014-20-2-1002

exhibit a centralized separation/reattachment event which is constrained in size in the spanwise direction by the shoulders of the bump. This result serves to verify that the primary region of interest for measurements is isolated from corner-flow influence over a range of conditions broader than what is planned for wind-tunnel testing. Additionally, all simulations with the exception of the forward bump at M~0.289 indicate development of a pair streamwise-oriented, counter-rotating vortices beginning downstream of reattachment. Finally, all separation lines begin at a finite distance downstream of the bump apex, and both separation and reattachment lines are strongly three dimensional.

Although there are several commonalities between all nine simulations, a few sensitivities were

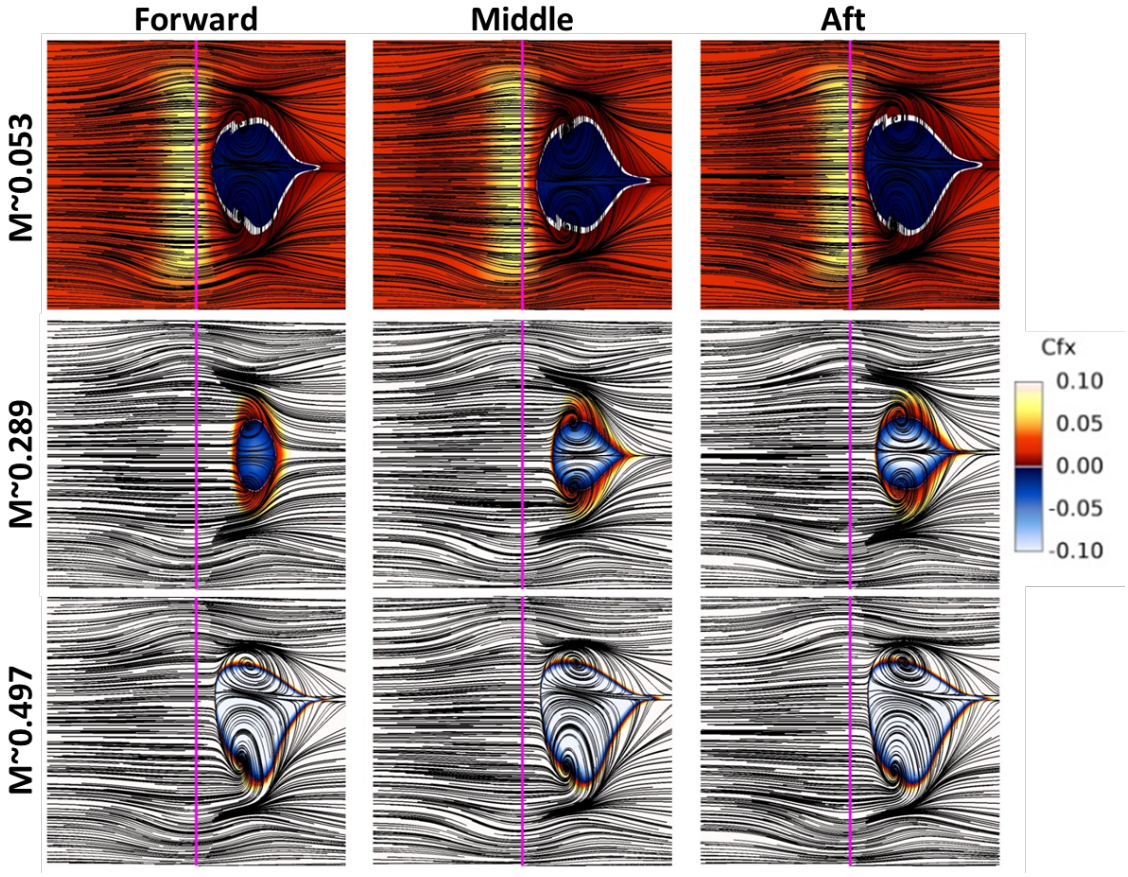

Figure 21: Planform view of surface streamlines over the bump, colored by the x-component of skin friction (Cfx), and predicted using SST-QCR. Vertical magenta lines indicate bump-apex location.

also observed. First, while spanwise symmetry is reasonable for M~0.05 and M~0.3, flow downstream of separation becomes noticeably asymmetric near M~0.5. It is assumed that this asymmetry is encouraged by the stronger and more dynamic separated-flow region experienced as Mach number increases. Another Mach-number sensitivity is observed by looking at the variation in shape and size of the reversed-flow region for a particular bump location. As Mach number increases from M~0.05 to M~0.3 the boundary layer separates farther downstream from the apex, and the reversed-flow footprint is greatly reduced. Further increasing Mach number

from ~0.3 to ~0.5 results in the separation line moving back toward the apex, and a significant increase in the reversed-flow footprint. The final sensitivity which can be seen in Figure 21, and most noticeably for M~0.3, is a slight increase in reversed-flow footprint as the bump moves downstream.

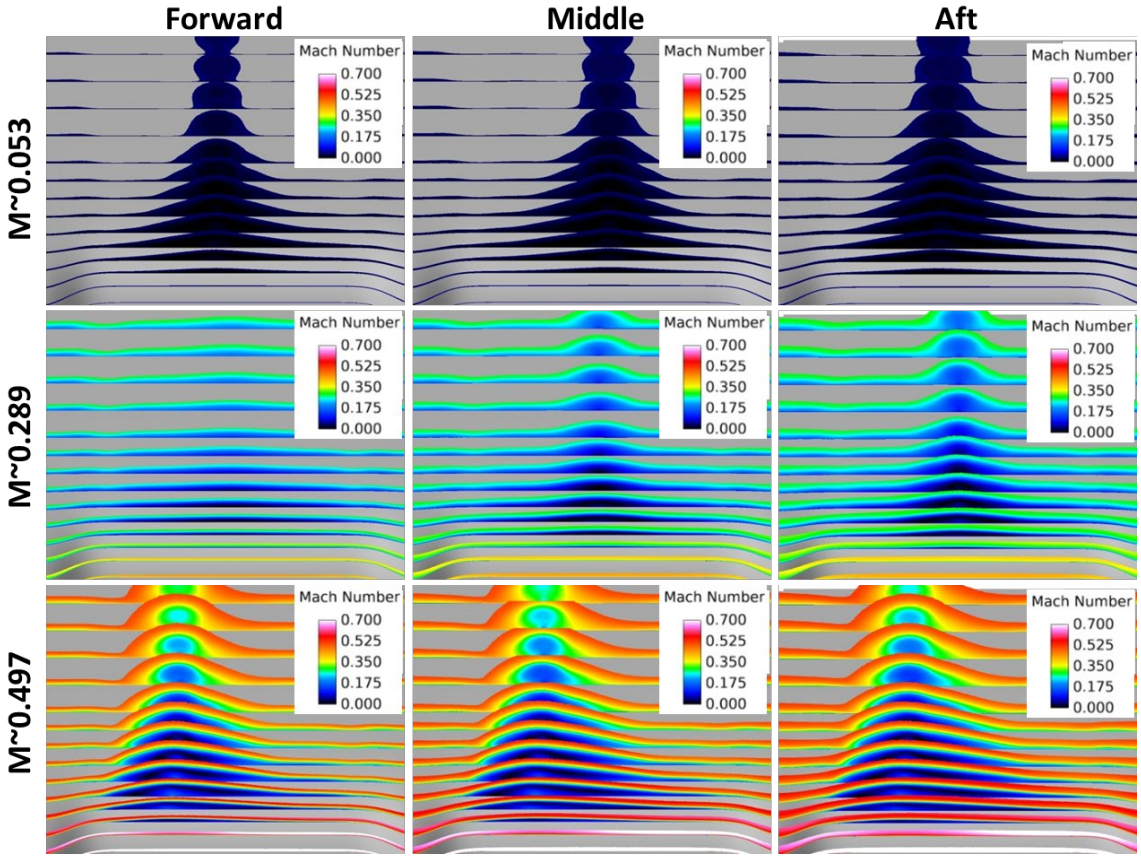

Figure 22: Constant x-coordinate cuts, with a threshold of total-pressure ratio (Pt/Pt0) less than 0.999, colored by Mach number. View is sitting on the bump looking downstream.

Off-surface views of the same nine flow simulations presented in Figure 21 are given in Figure 22. In addition to corroborating the aforementioned similarities and differences in flows between the various bump positions and Mach numbers, the images in Figure 22 provide several new insights. First, size and strength of the vortex pair which develops downstream of reattachment appears to increase subtly as the bump moves downstream. Second, variation in the size and strength of these vortices with Mach number correlates to the aforementioned variation in reversed-flow footprint with Mach number. Lastly, the wall-normal size of the recirculation and vortex pair immediately downstream of the bump is on the order of the height of the bump (~3 inches), and greatest along the centerline where a region of upwash exists between the two vortices.

In an effort to quantify the expected range of Reynolds numbers and boundary-layer thicknesses that will be encountered in the wind-tunnel tests, these quantities were computed along the centerline of the splitter plate for the bump in the aft-most position at the lowest and highest

Mach numbers simulated. To compute the thicknesses, the vorticity-layer approach described by Uzun and Malik[10] was used. The resulting boundary-layer thickness, displacement thickness, and momentum thickness, along with Reynolds numbers computed using these length scales, are plotted in Figure 23. Qualitatively it is observed that the boundary layer upstream of the bump is thinner at a particular x for the greater test-section Mach number. A pronounced dip in thickness is observed over the upstream half of the bump due to the favorable pressure gradient, where the minimum thickness aligns closely with the bump apex. This local minimum is follow by a rapid growth in thickness brought on by separation. At both Mach numbers, but more pronounced at M~0.5, the rapid rise in thickness breaks where the shear layer reattaches, and then a secondary

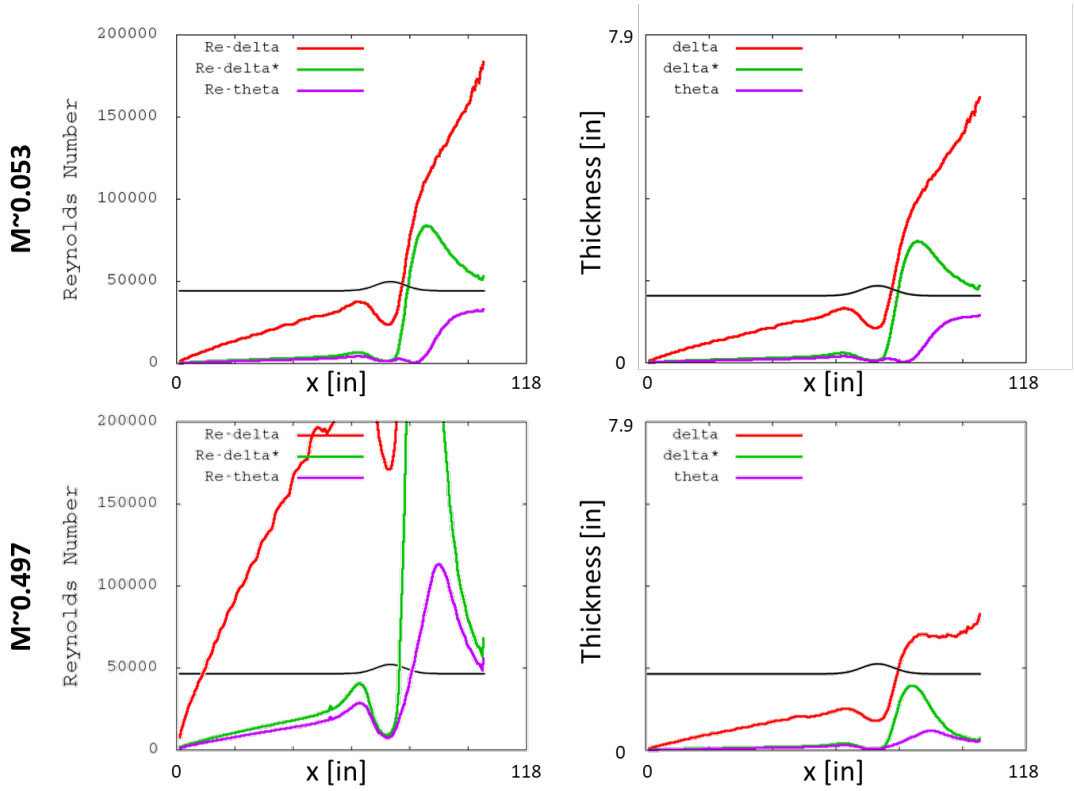

Figure 23: Boundary-layer thickness (delta), displacement thickness (delta), and momentum thickness (theta), and their corresponding Reynolds numbers along the splitter centerline. Side view of splitter/bump profiles overlaid for reference.*

rise in thickness is observed corresponding to the development and growth in the streamwise-oriented vortex pair. The thicknesses and corresponding Reynolds numbers at x = 54", which corresponds to the upstream end of the bump test article when mounted in the aft-most position, are presented in Table 4. Using this information, the Reynolds number based on bump width (L = 32"), ReL, ranges approximately from 0.92e6 to 7.8e6 with the bump in the aft-most position. Similar data at x = 14" is given in Table 5, which provides a lower bound on Reynolds numbers that would be experienced by the bump located at the forward-most position. These lower Reynolds numbers provide a more accessible point of comparison with direct numerical simulation (DNS).

Table 4: Thicknesses and Reynolds numbers upstream of the bump located in the aft-most position.

Approximate Test-Section Mach Number	Delta [in]	Delta* [in]	Theta [in]	Re-Delta	Re-Delta*	Re-Theta
0.05	1.09	0.17	0.12	31,457	4,794	3,339
0.3	0.89	0.12	0.09	134,607	18,064	13,461
0.5	0.84	0.11	0.08	203,983	26,455	19,965

Table 5: Thicknesses and Reynolds numbers upstream of the bump located in the forward-most position.

Approximate Test-Section Mach Number	Delta [in]	Delta* [in]	Theta [in]	Re-Delta	Re-Delta*	Re-Theta
0.05	0.36	0.05	0.04	10,358	1,557	1,040
0.3	0.31	0.04	0.03	46,279	5,637	4,125
0.5	0.28	0.03	0.03	68,240	8,158	6,071

b) Time-Accurate RANS/LES Analysis

Time-accurate simulations were performed using both DDES (with SA-RC-QCR) and LESb (with SST-QCR) at all three bump locations for test-section Mach numbers 0.1, 0.3, and 0.5. Inflow total pressure and total temperature were set to 14.4 psi and 550 R, and outflow pressures were prescribed as 14.3, 13.5, and 12 psi to achieve the above test-section Mach numbers. All time-accurate simulations were restarted from RANS simulations performed with the same boundary conditions. Time steps used for each outflow pressure were computed using the bump-surface element edge length (~0.06") and velocity magnitude in the middle of the separated shear layer, and are given in Table 6.

Table 6: Time steps used for the time-accurate simulations.

Outflow Pressure [psi]	Approximate Test-Section Mach Number	Time Step [s]
12	0.5	1.2e-5
13.5	0.3	2.4e-5
14.3	0.1	7.5e-5

After the simulations were restarted from RANS, they were run through a 'transitional' period prior to collecting statistics. The transition-period duration was determined individually for each simulation based upon how long it took for the bump loads, test-section Mach number, and test-section flow rate to reach a limit cycle. The number of transitional time steps along with the corresponding convective distance in 110-inch plate lengths is given for all 18 time-accurate simulations in Table 7. Following the transitional period in the simulation, statistics were collected for 10-20 plate lengths, which corresponds to 30-60 bump lengths.

Table 7: Data for transition-period duration for each time-accurate simulation.

Bump Position	Outflow Pressure [psi]	Turbulence Model	Time Steps	Plate Lengths
fwd	14.3	DDES	10907	5.95

fwd	13.5	DDES	15360	8.38
fwd	12	DDES	15043	8.21
fwd	14.3	LESb	16567	9.04
fwd	13.5	LESb	17390	9.49
fwd	12	LESb	23935	13.06
mid	14.3	DDES	12932	7.05
mid	13.5	DDES	12850	7.01
mid	12	DDES	12839	7.00
mid	14.3	LESb	17766	9.69
mid	13.5	LESb	17837	9.73
mid	12	LESb	14068	7.67
aft	14.3	DDES	21868	11.93
aft	13.5	DDES	20986	11.45
aft	12	DDES	21893	11.94
aft	14.3	LESb	30041	16.39
aft	13.5	LESb	31362	17.11
aft	12	LESb	33174	18.09

Several time-averaged quantities were plotted to help describe key elements of the flow field and its sensitivity to turbulence model, bump location, and test-section Mach number. The first quantity, plotted in Figure 24, is the x-component of time-averaged vorticity for the forward bump location. The primary features, as previously seen from the RANS simulations, is the

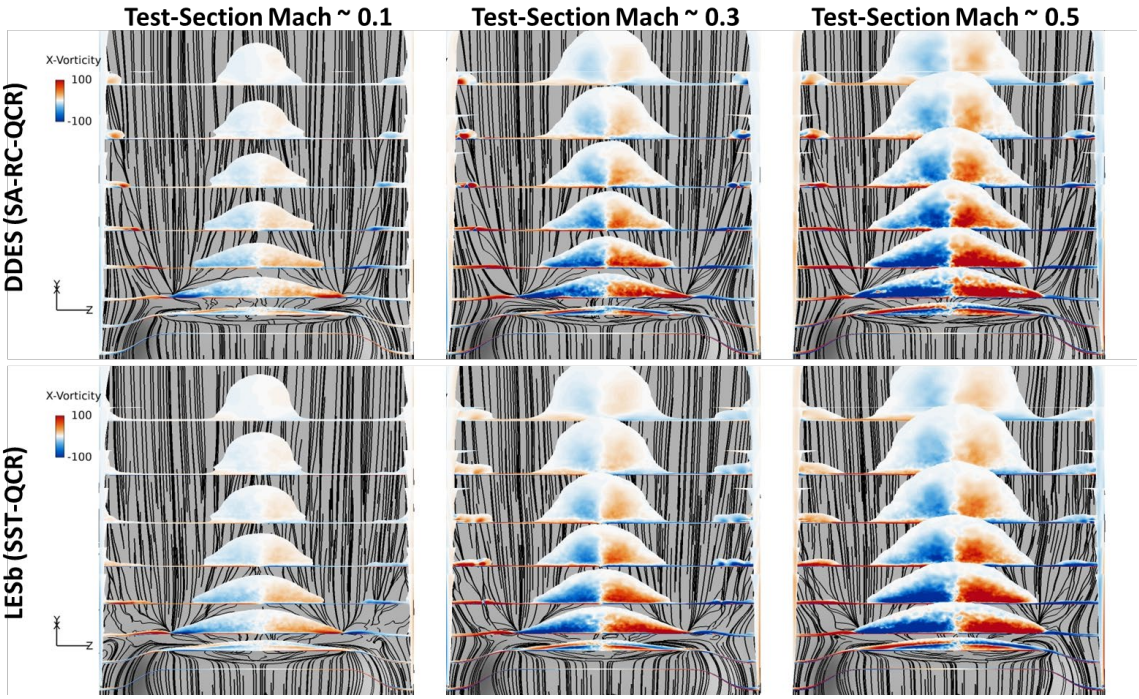

Figure 24: Constant x-coordinate cuts with a spatial threshold showing regions where Pt/Pt0 < 0.999, and colored by the time-averaged x-component of vorticity. View is sitting on the bump at the forward location looking downstream. Blue is the counter clockwise sense of vorticity and red is clockwise.

ONR Contract Number N00014-20-2-1002

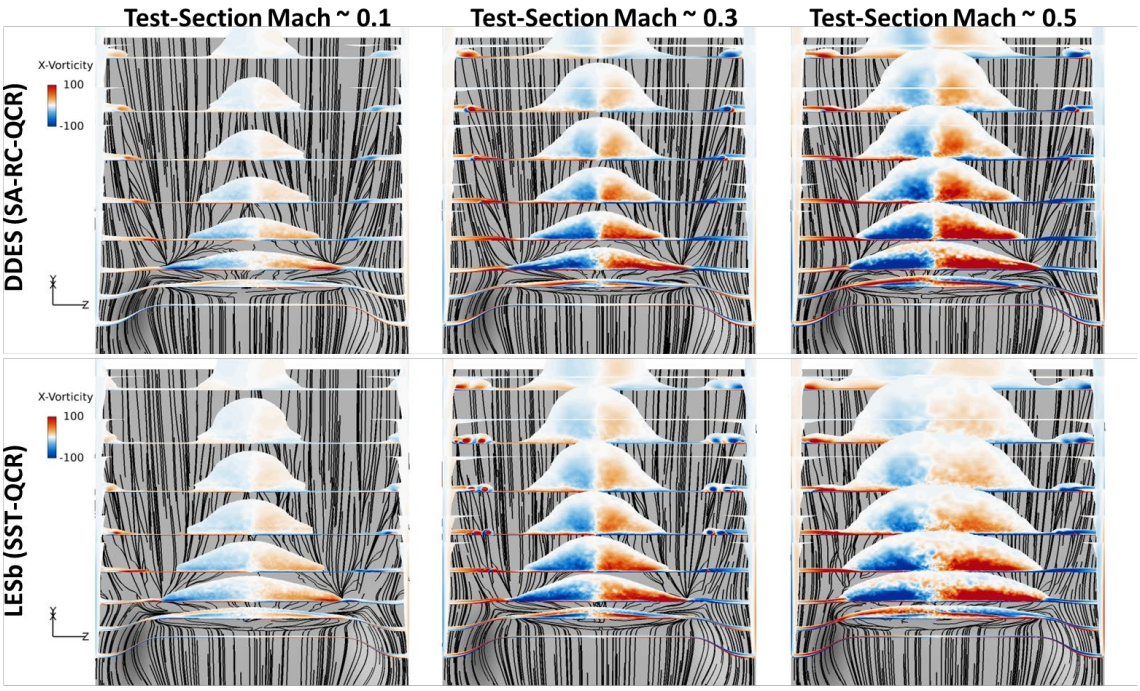

Figure 25: Constant x-coordinate cuts with a spatial threshold showing regions where Pt/Pt0 < 0.999, and colored by the time-averaged x-component of vorticity. View is sitting on the bump at the middle location looking downstream. Blue is the counter clockwise sense of vorticity and red is clockwise.

central separation and reattachment, and subsequent development of streamwise-oriented, counter-rotating vortices. These primary features are qualitatively insensitive to turbulence model, but increase in size and strength with increasing test-section Mach number. A secondary feature observed from Figure 24, which was not clearly present in the RANS simulations, is the pair of smaller vortices which develop outboard on either side of the bump. These vortices are very sensitive to turbulence model, where with DDES they develop and convect downstream before interacting with the corner flow, but with LESb they collide with the corner region shortly after they develop. It is also observed that the size and strength of these secondary vortices, along with the intensity of their interaction with the corner flows, increases with test-section Mach number.

Similar plots with the bump located at the middle and aft locations are given in Figure 25 and Figure 26, respectively. The sensitivities for the middle and aft locations are generally very similar to those observed at the forward location. One key difference is that the secondary vortices track more inboard and collide with the corner regions farther downstream from the bump than for the forward bump location. This effect appears to be generally insensitive to test-section Mach number for DDES, but is increasingly apparent for LESb for increasing test-section Mach number. Another difference, which is most clearly observed at Mach~0.5, is that the separation wake is wider for the middle and aft bump locations. This increase in spanwise extent of the primary wake causes it to interact with the secondary vortices and corner flows, and this interaction is more pronounced with LESb than DDES.

One particular oddity with the aft-bump solution is observed for Mach ~ 0.1 in Figure 26, where an asymmetry in the separation and subsequent wake can be seen. The asymmetry is most apparent for the DDES solution, and appears to stem from a bulge in the boundary layer on the right half of the bump. This boundary-layer distortion exists upstream of the separation, and upon closer inspection of the solution was found to develop far upstream of the bump. The distortion appears to be due at least in part to disturbances propagating upstream to the inflow boundary, causing non-uniformities to develop in total pressure on the inflow plane. The non-uniformities then generate low-magnitude (less than 0.02 psi in total pressure) disturbances which perturb and distort the boundary layer. This is possible because the shielding function in the LESb and DDES models allows the outer ~25% of the boundary layer, for these particular simulations, to be resolved with LES, making the boundary layer receptive to disturbances. It is assumed that the low convective Mach number and the long plate-approach length for the aft-bump position both contribute to an asymmetry showing up in Figure 26, where it did not for the forward and mid-bump positions. Based on this result, future simulations will make use of a different inflow boundary condition which allows for total pressure and total temperature to remain constant and uniform on the inflow plane.

Contours of root-mean-square fluctuations in each velocity component (u'-rms, v'-rms, and w'-rms) normalized by mean freestream velocity magnitude (Vinf) are plotted in Figure 27 through Figure 35. Freestream velocity magnitude values used for normalization at Mach 0.1, 0.3, and 0.5 were 112 ft/s, 340 ft/s, and 557 ft/s, respectively. In general, turbulence intensity is observed to increase with Mach number.

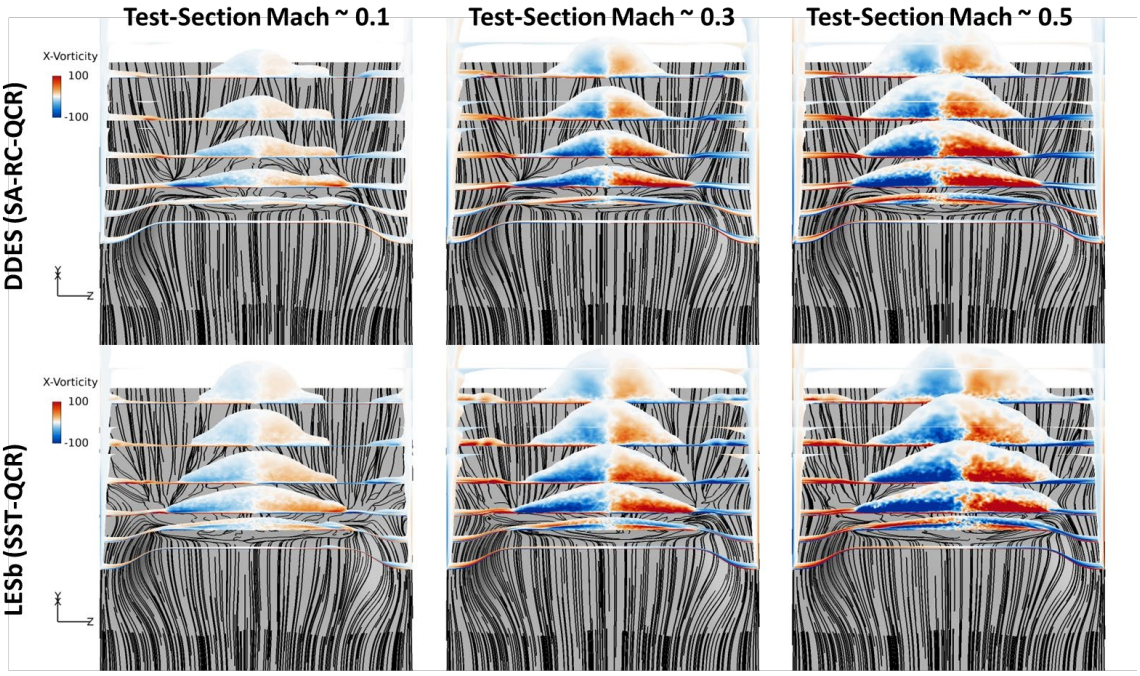

Figure 26: Constant x-coordinate cuts with a spatial threshold showing regions where Pt/Pt0 < 0.999, and colored by the time-averaged x-component of vorticity. View is sitting on the bump at the aft location looking downstream. Blue is the counter clockwise sense of vorticity and red is clockwise.

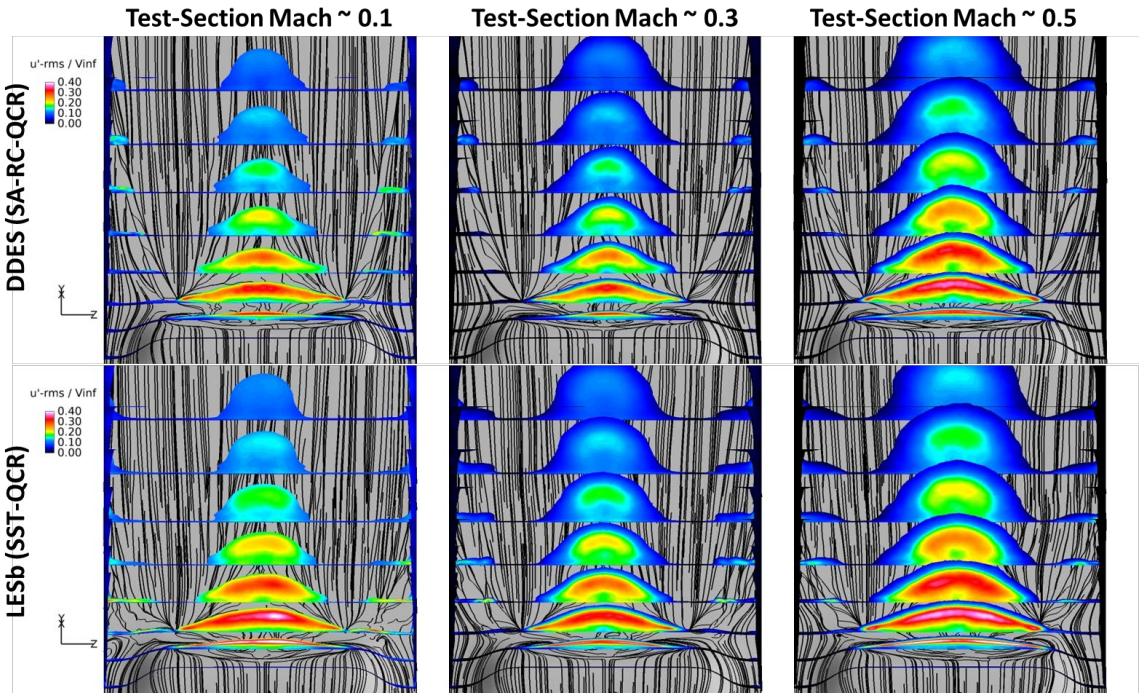

Figure 27: Constant x-coordinate cuts with a spatial threshold showing regions where Pt/Pt0 < 0.999, and colored by the root-mean-squared of the fluctuations in the x-component of velocity (u'-rms). View is sitting on the bump at the forward location looking downstream.

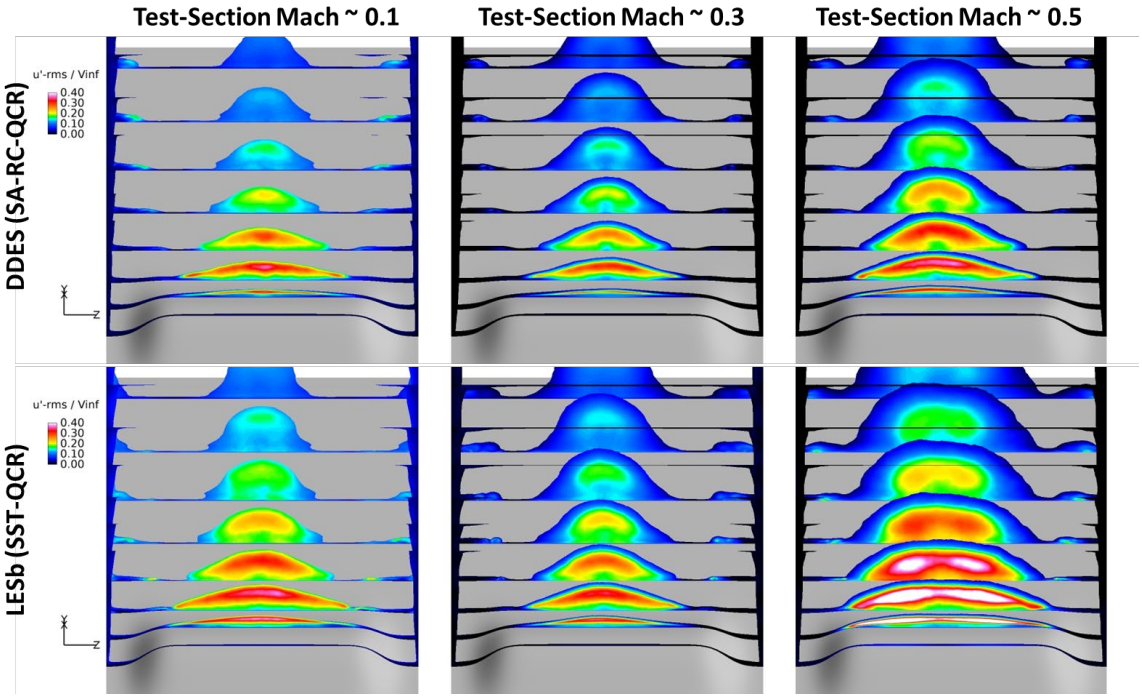

Figure 28: Constant x-coordinate cuts with a spatial threshold showing regions where Pt/Pt0 < 0.999, and colored by the root-mean-squared of the fluctuations in the x-component of velocity (u'-rms). View is sitting on the bump at the middle location looking downstream.

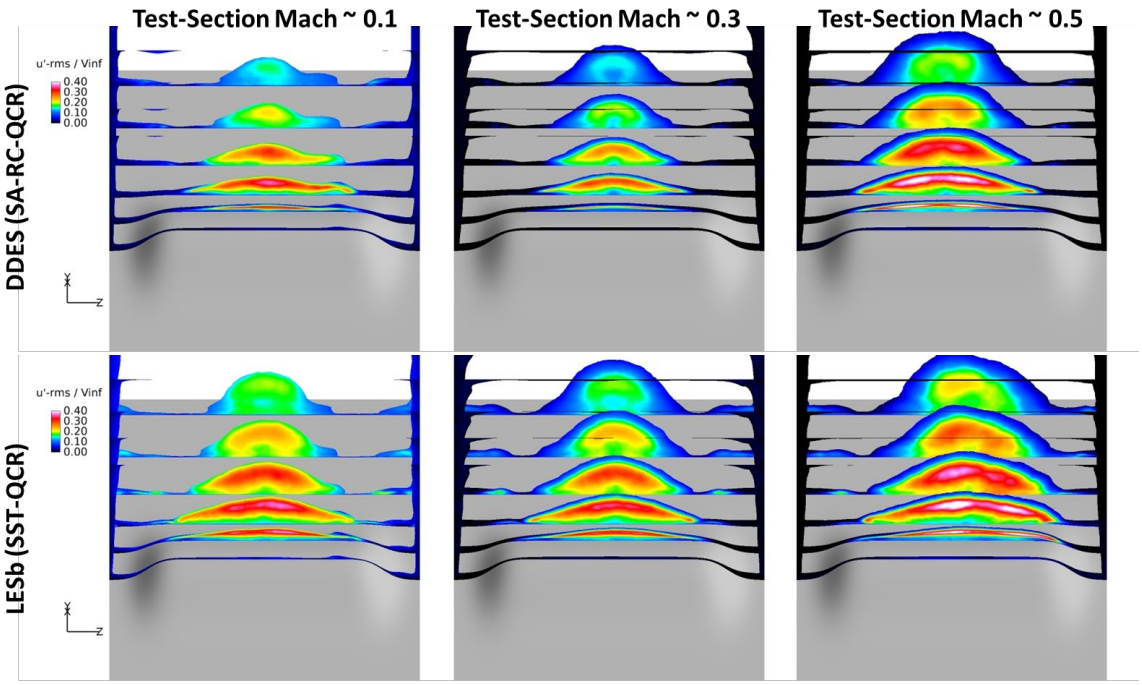

Figure 29: Constant x-coordinate cuts with a spatial threshold showing regions where Pt/Pt0 < 0.999, and colored by the root-mean-squared of the fluctuations in the x-component of velocity (u'-rms). View is sitting on the bump at the aft location looking downstream.

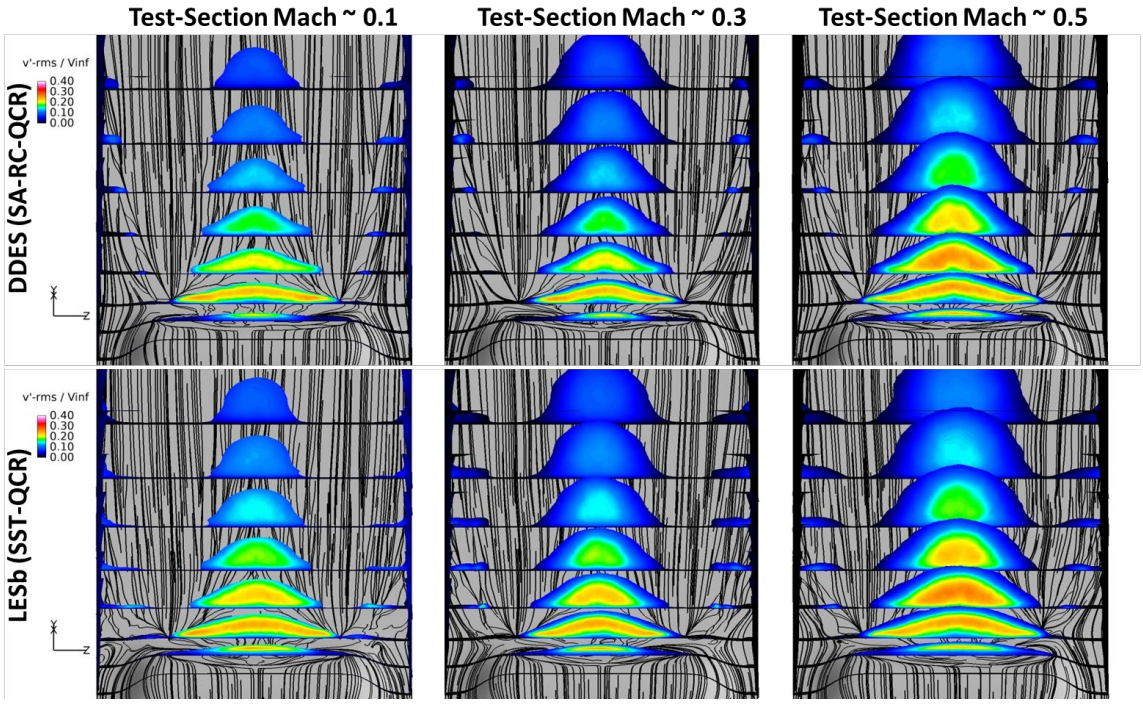

Figure 30: Constant x-coordinate cuts with a spatial threshold showing regions where Pt/Pt0 < 0.999, and colored by the root-mean-squared of the fluctuations in the y-component of velocity (v'-rms). View is sitting on the bump at the forward location looking downstream.

ONR Contract Number N00014-20-2-1002

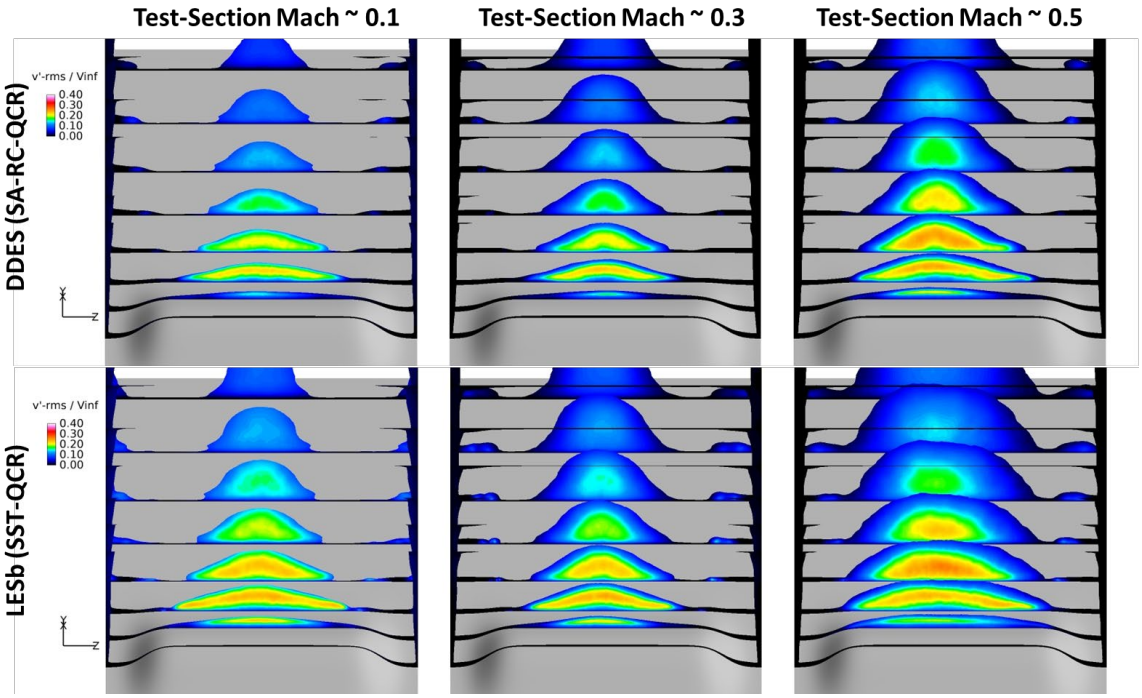

Figure 31: Constant x-coordinate cuts with a spatial threshold showing regions where Pt/Pt0 < 0.999, and colored by the root-mean-squared of the fluctuations in the y-component of velocity (v'-rms). View is sitting on the bump at the middle location looking downstream.

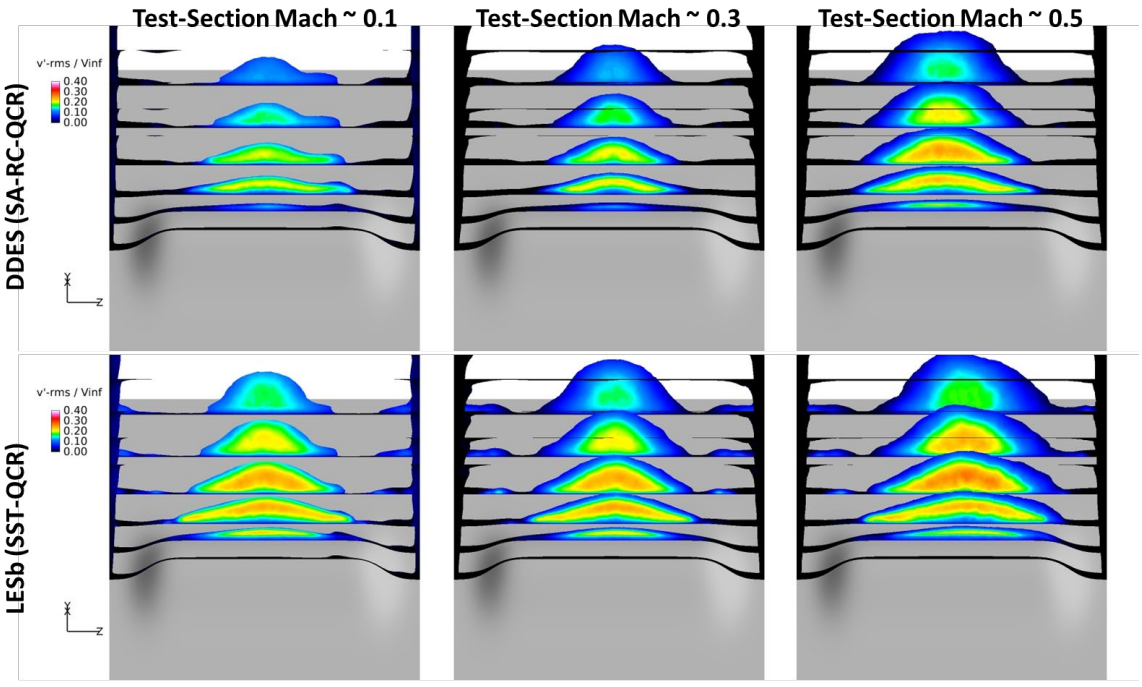

Figure 32: Constant x-coordinate cuts with a spatial threshold showing regions where Pt/Pt0 < 0.999, and colored by the root-mean-squared of the fluctuations in the y-component of velocity (v'-rms). View is sitting on the bump at the aft location looking downstream.

ONR Contract Number N00014-20-2-1002

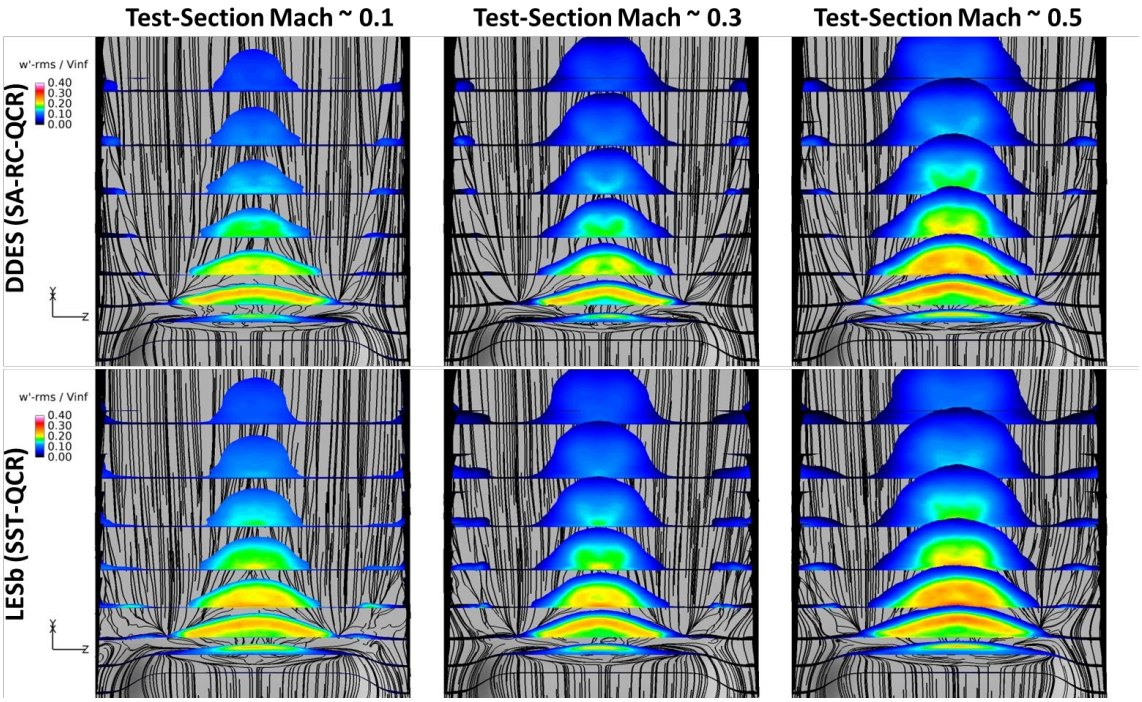

Figure 33: Constant x-coordinate cuts with a spatial threshold showing regions where Pt/Pt0 < 0.999, and colored by the root-mean-squared of the fluctuations in the y-component of velocity (w'-rms). View is sitting on the bump at the forward location looking downstream.

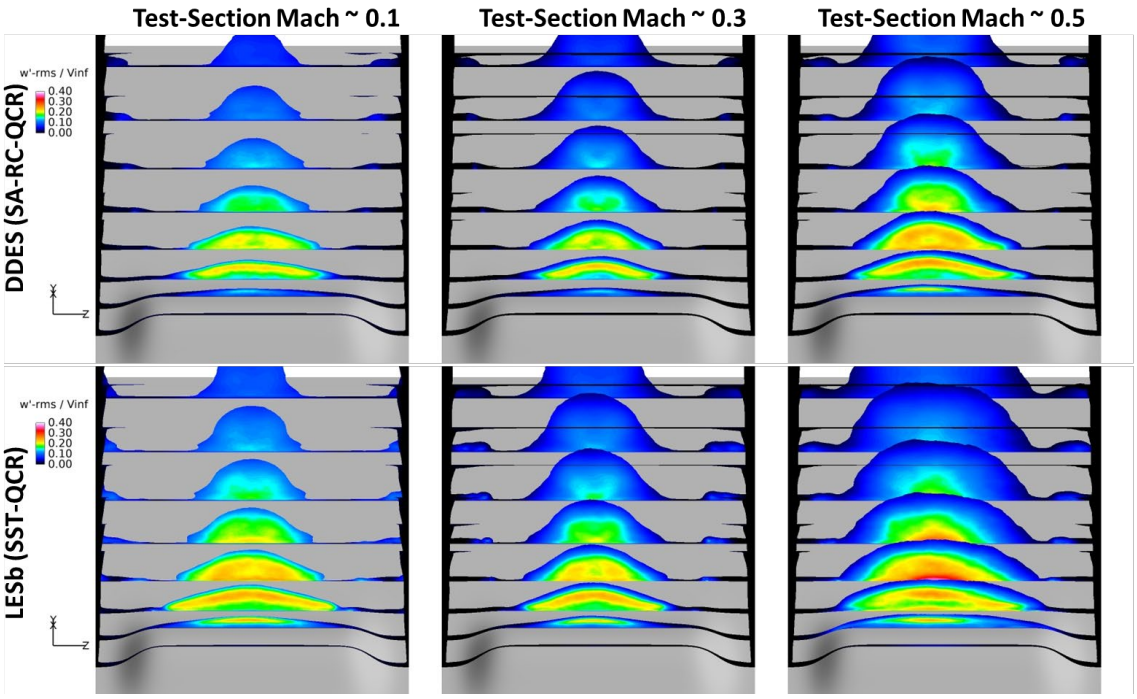

Figure 34: Constant x-coordinate cuts with a spatial threshold showing regions where Pt/Pt0 < 0.999, and colored by the root-mean-squared of the fluctuations in the y-component of velocity (w'-rms). View is sitting on the bump at the middle location looking downstream.

ONR Contract Number N00014-20-2-1002

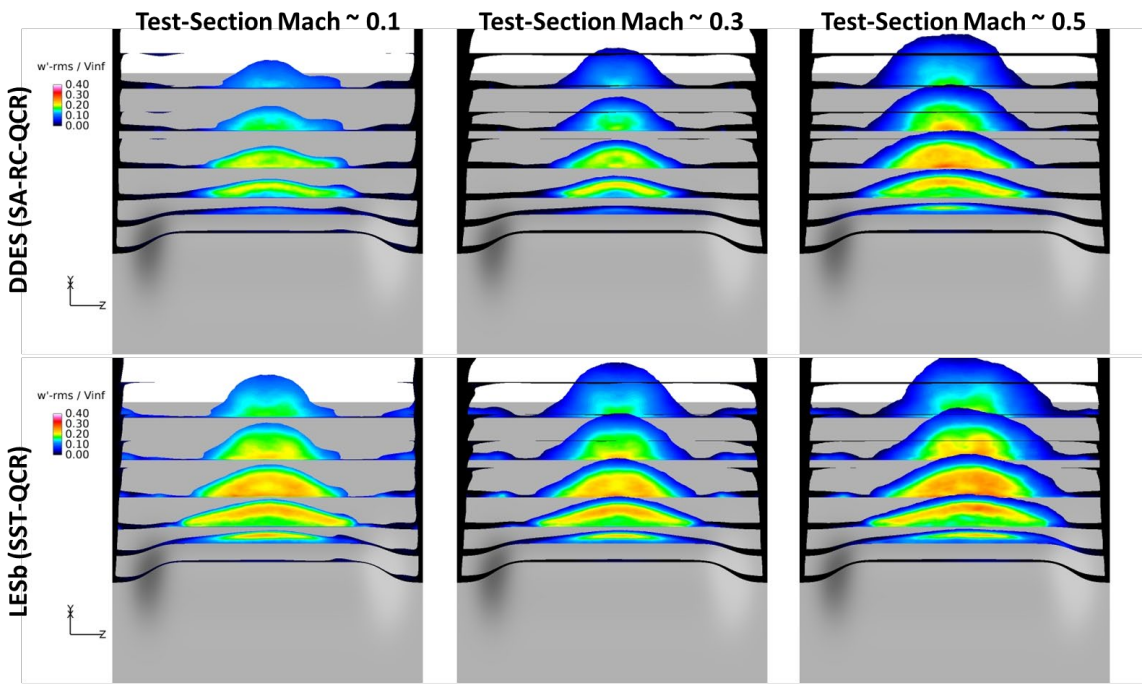

Figure 35: Constant x-coordinate cuts with a spatial threshold showing regions where Pt/Pt0 < 0.999, and colored by the root-mean-squared of the fluctuations in the y-component of velocity (w'-rms). View is sitting on the bump at the aft location looking downstream.

Value of u'-rms are observed to peak at 40-50%, whereas v'-rms and w'-rms peak at 20-30%. LESb is observed to predict greater u'-rms levels than DDES, but v'-rms and w'-rms are comparable between the two models. Variation in turbulence levels does not appear to be sensitive to bump location. Over the separation, the greatest levels of turbulence appear to be focused within the shear layer, whereas downstream of reattachment the highest turbulence concentration moves toward the wall in the regions interior to the primary streamwise vortices. Low levels of turbulence (~10%) are also predicted in the regions occupied by the secondary vortices and where they interact with the corners.

Instantaneous iso-surfaces of Q-criterion are plotted in Figure 37 and Figure 37 for each bump location, Mach number, and turbulence model. The plan views clearly illustrate the separation line, primary wake size, and secondary-vortex trajectory. Although there is no qualitative difference in the primary wake between the two turbulence models for the forward bump position, LESb clearly predicts a larger separation and wake than DDES for the middle and aft bump positions. It is also observed that while the primary wake does not significantly interact with the secondary vortices for the forward bump, the primary wake produced by the middle and aft bumps clearly interacts with the secondary vortices, particularly at Mach 0.5, and particularly for the LESb model. From the side views it can be seen that the wake protrudes farther into the freestream with increasing Mach number. As this happens, large-scale eddies are observed to develop in the shear layer between the freestream and the streamwise-oriented vortex pair. These eddies appear to be a secondary vortex that wraps around the primary vortex pair and terminates at the wall on either side. They also seem to appear at a regular spatial interval,

particularly at Mach 0.5, which may suggest an oscillatory ‘flapping’ of the wake in the wall normal direction, where the wrapping vortices are generated when the wake is farthest from the wall. No wrapping vortices are discernable at Mach 0.1.

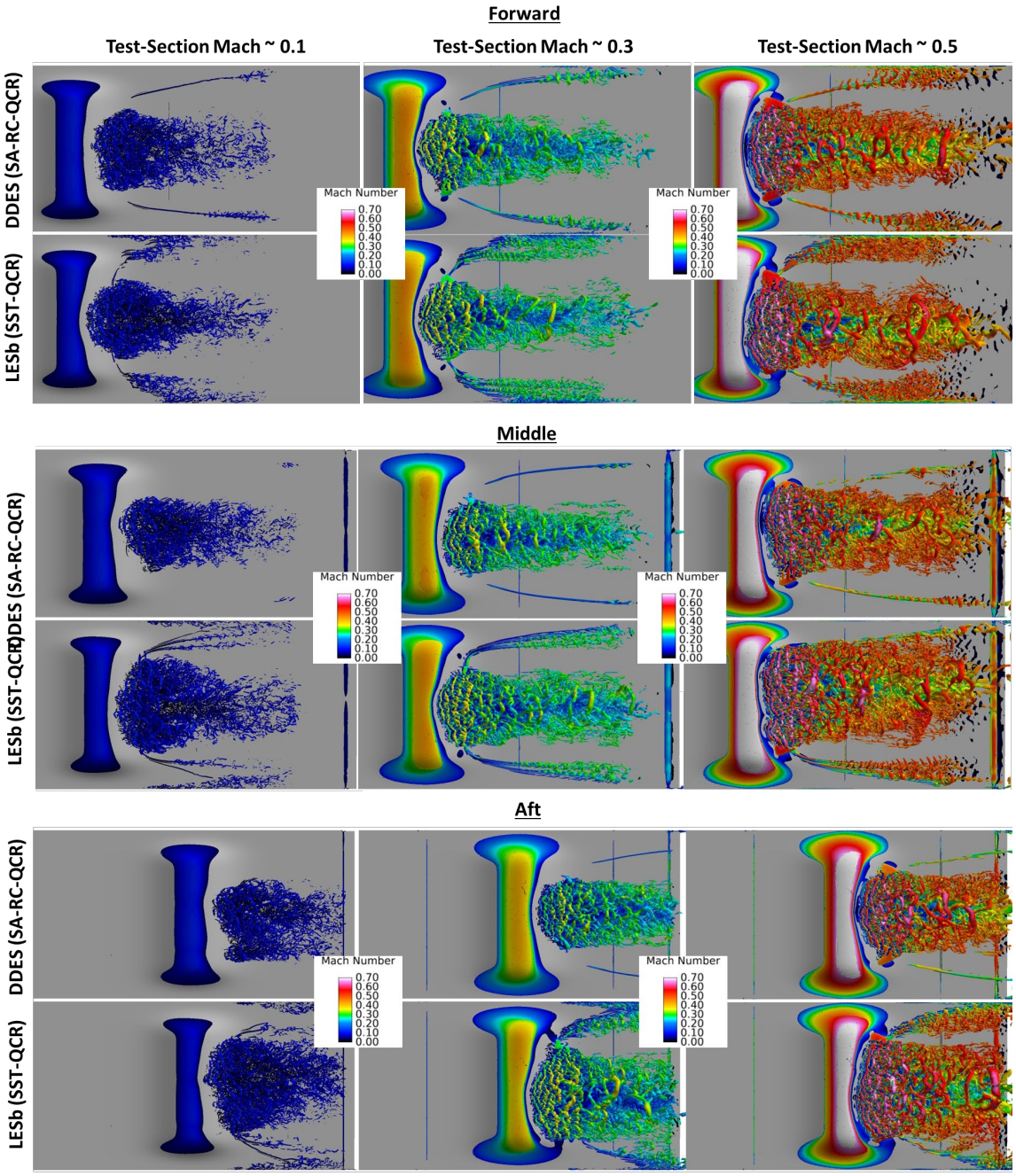

Figure 36: Q-criterion iso-surfaces at a value of 10,000 s^-2 colored by Mach number depicting separation, reattachment, primary wake development, and secondary vortices. Plan View.

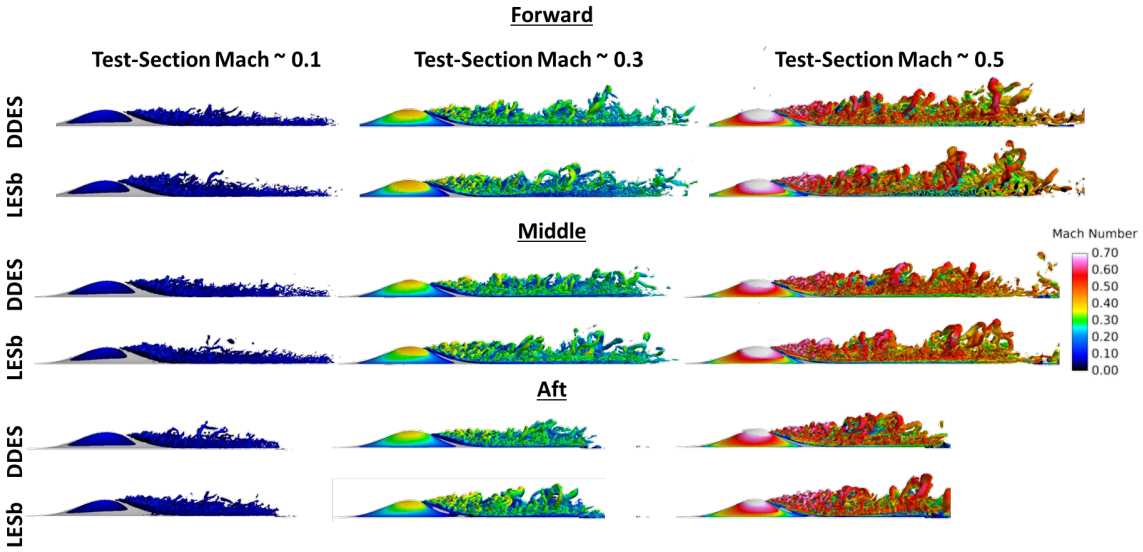

Figure 37: Q-criterion iso-surfaces at a value of 10,000 s^-2 colored by Mach number depicting separation, reattachment, primary wake development, and secondary vortices. Side view.

4) Comparisons with Particle Image Velocimetry (PIV) Measurements

Velocity measurements from PIV were compared with RANS and DDES along the center plane downstream of the bump apex for Mach 0.2. Solution results were interpolated onto a grid, which was created to exactly match PIV-measurement grid (Figure 38). Statistics were accumulated for ~0.7 seconds, which corresponds to fluid within the separated shear layer convecting approximately 30 bump lengths.

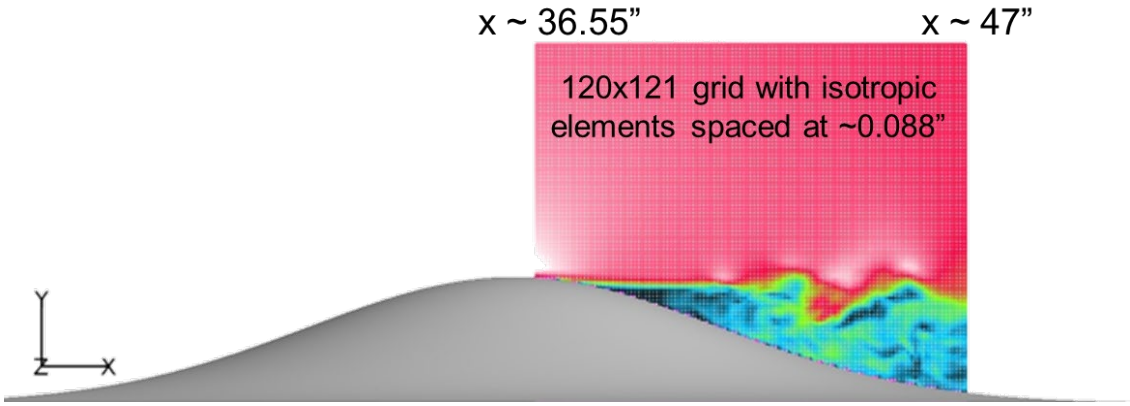

Figure 38: Depiction of the center-plane PIV window location relative to the bump. Instantaneous Mach-number contours from a DDES are plotted on the grid to illustrate the wall-normal extent of the wake.

Comparisons of u, v, and u’v’ are given in Figure 39 - Figure 41. These results indicate that RANS fails to accurately predict the flow downstream of the apex. DDES is in good qualitative agreement, but appears to slightly over-predict the shear-layer spreading rate (Figure 39), and under-predict the downwash outside of the separated shear layer. This under-prediction of downwash, particularly upstream of separation, seems to indicate that DDES separates too early. Figure 41 shows good agreement in both the distribution and magnitude of u’v’ in the separated shear layer, with DDES slightly over-predicting the size of the turbulent shear region.

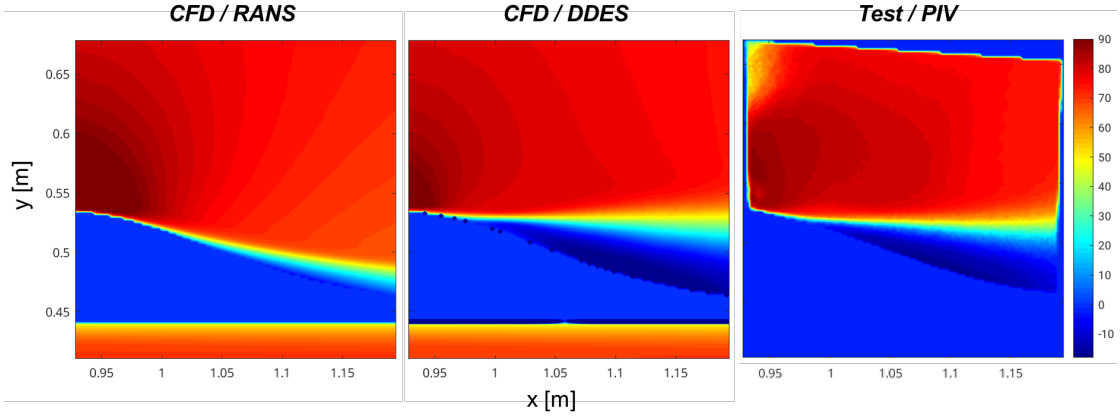

Figure 39: Comparison of the u-component of velocity, in m/s, between RANS (left), DDES (middle), and PIV (right).

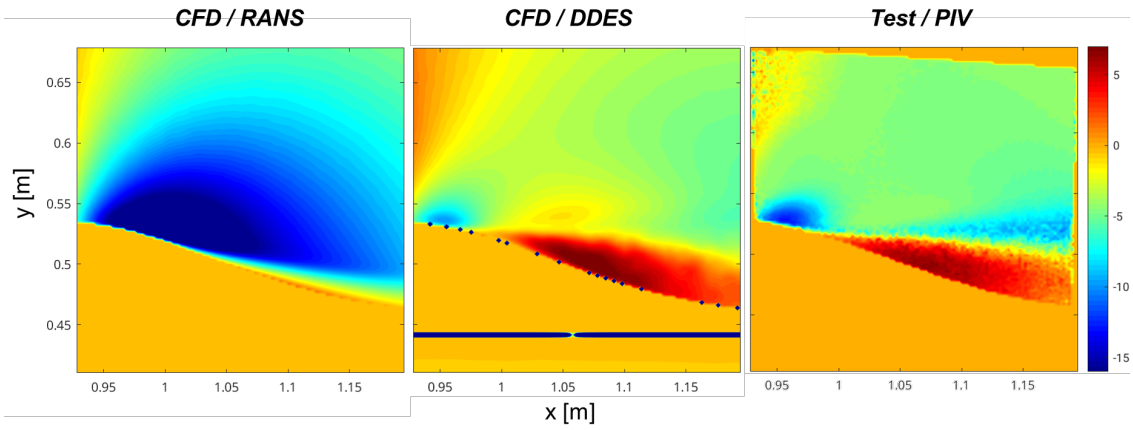

Figure 40: Comparison of the v-component of velocity, in m/s, between RANS (left), DDES (middle), and PIV (right).

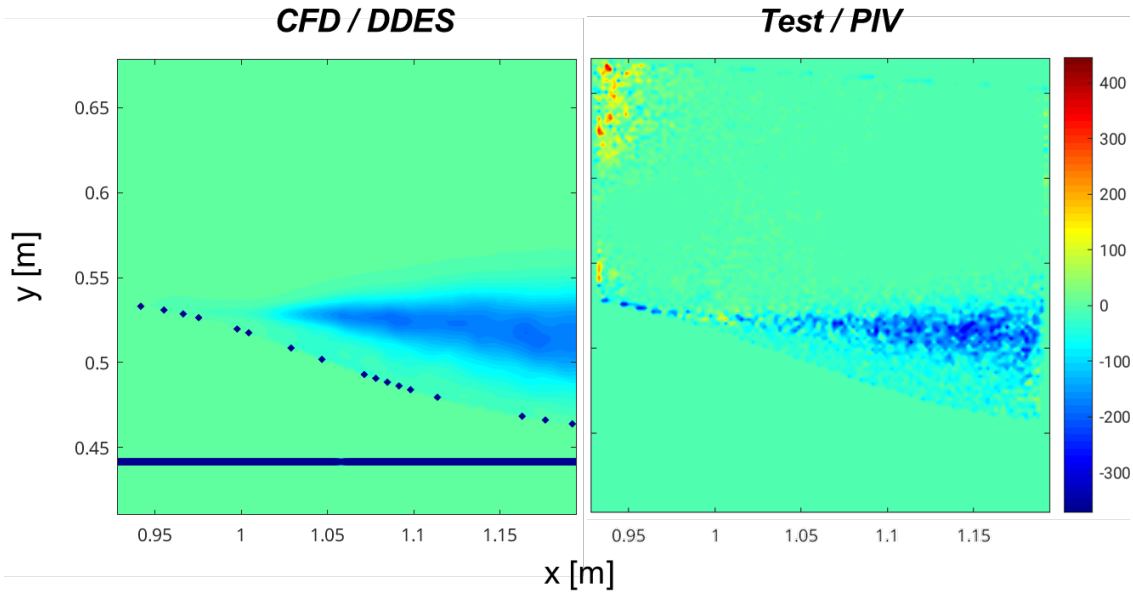

Figure 41: Comparison of u'v', in m^2/s^2, between DDES (left) and PIV (right).

ONR Contract Number N00014-20-2-1002

A more-comprehensive set of PIV measurements was made for forward and aft bump positions at Mach 0.05, 0.1, and 0.2 for various spanwise locations. The streamwise extent for this recent dataset covers from approximately the bump apex to just downstream of boundary-layer reattachment. The entire experimental dataset was processed in a manner consistent with that used for the CFD simulations, and comparisons were made for the forward bump at Mach 0.2 over the planar regions depicted in Figure 42. The first comparison shown in Figure 43 is for the u-component of velocity on the z = +/- 3" planes to assess the degree of symmetry across the bump centerline. From the test PIV images shown in the left column, asymmetry is clear from the off-body size of the recirculation as well as the separation and reattachment locations. For the CFD in the right column, while very subtle asymmetry is observed with the separation location, the time average is notably more symmetric than that observed from the PIV measurements. Comparisons of the remaining quantities along the center plane (Z = 0) are given in Figure 44 through Figure 46. Generally good qualitative agreement is observed between test and CFD, with CFD tending to predict earlier separation and later reattachment than what is measured.

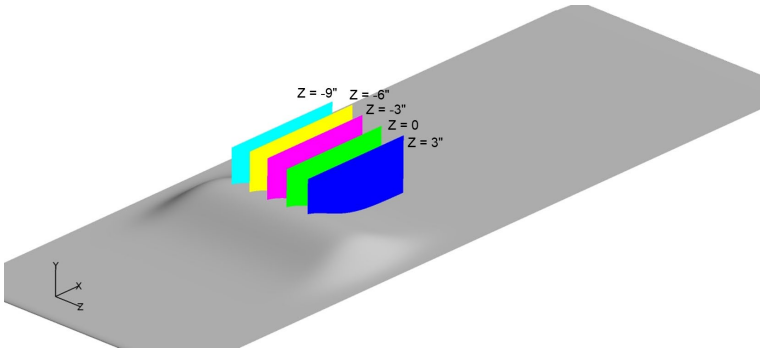

Figure 42: Forward-bump comparisons locations for PIV between test and

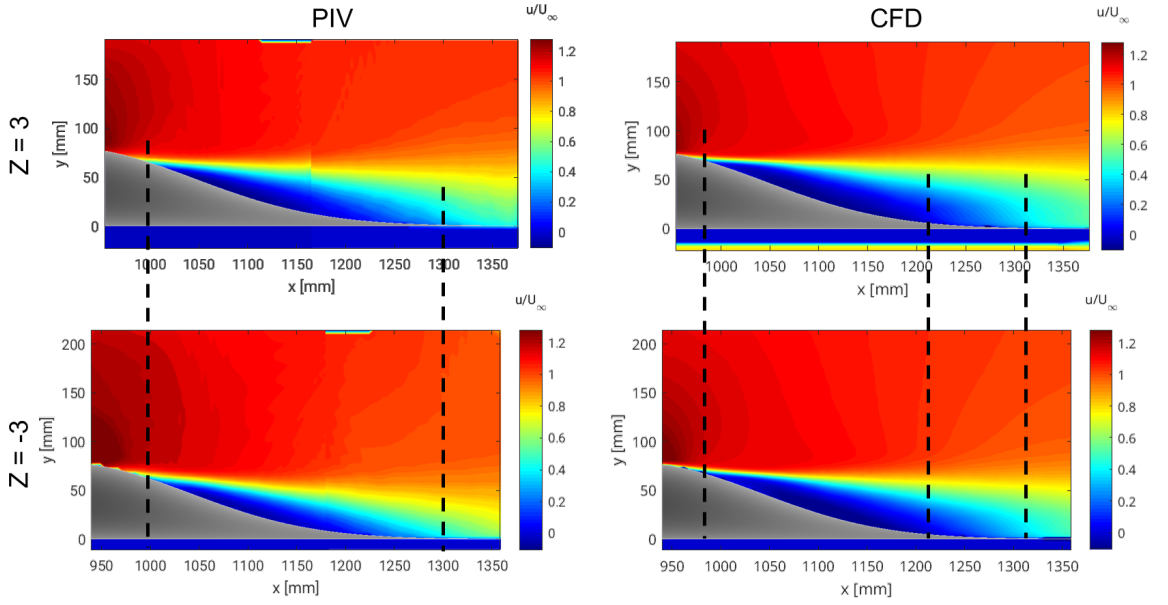

Figure 43: Comparison of symmetry between test and CFD 3 inches about the centerline using the u-component of velocity.

ONR Contract Number N00014-20-2-1002

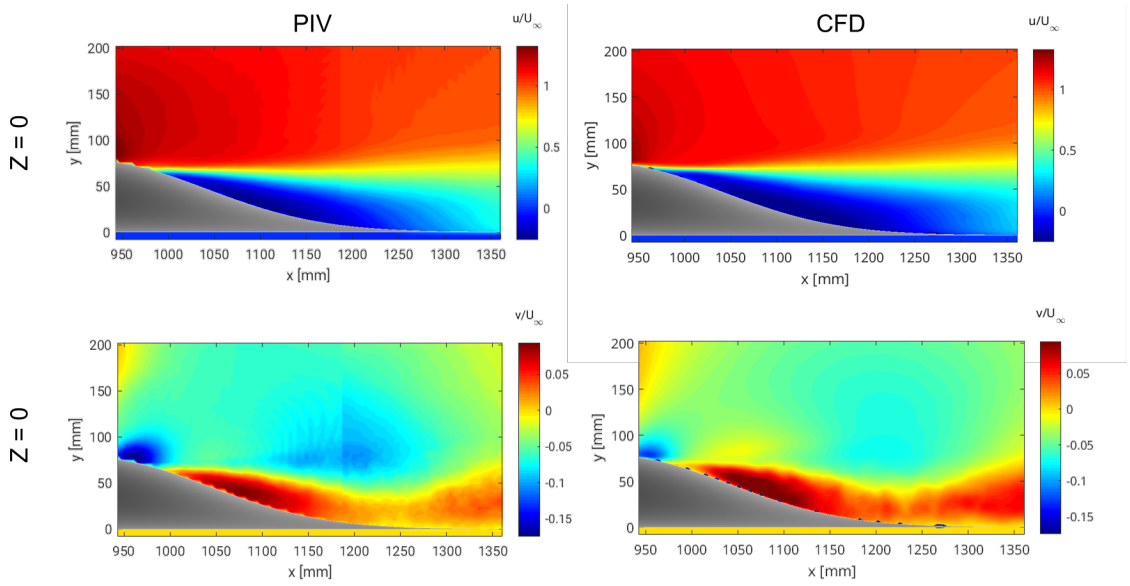

Figure 44: Comparison of u- and v-components of velocity along the center plane.

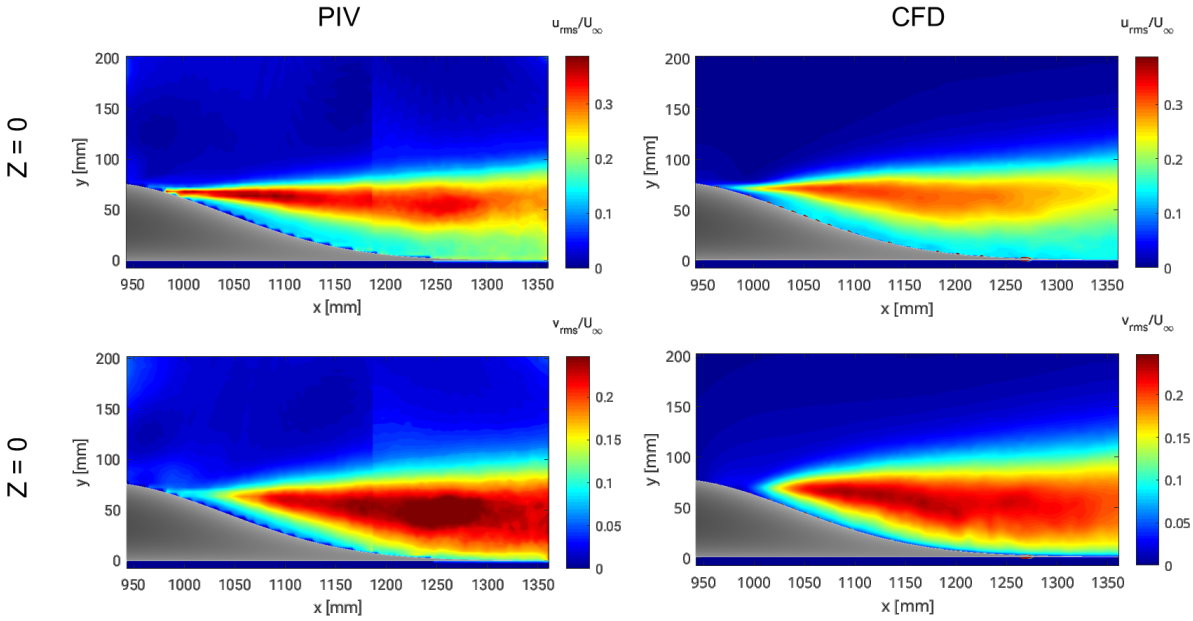

Figure 45: Comparison of fluctuations in u- and v-components of velocity along the center plane.

ONR Contract Number N00014-20-2-1002

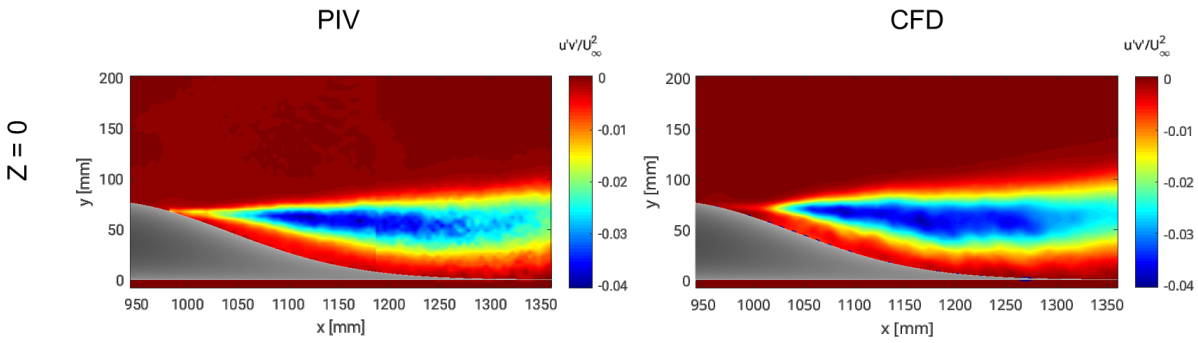

Figure 46: Comparison of Reynolds stress along the center plane.

5) Comparisons with Oil-Film Interferometry (OFI) Measurements

Time-accurate, DDES simulations were performed to match test-section Mach number as closely as possible with wind-tunnel runs from which skin-friction measurements were obtained. At the forward bump position (36" apex location), one condition corresponding to Mach 0.1 and ReL ~ 2e6 (L = 3') was compared. For the aft bump position (72" apex location), two conditions corresponding to Mach 0.1 and ReL ~ 2e6, and Mach 0.2 and ReL ~ 4e6, were compared. Skin-friction data used for comparison with wind-tunnel measurements was extracted from the simulations along the centerline (Station 7 in Figure 47), and spanwise cuts +/- 3 inches off centerline (Stations 6 and 8 in Figure 47). This was done to capture the spanwise range over which the OFI data was measured in the wind-tunnel tests.

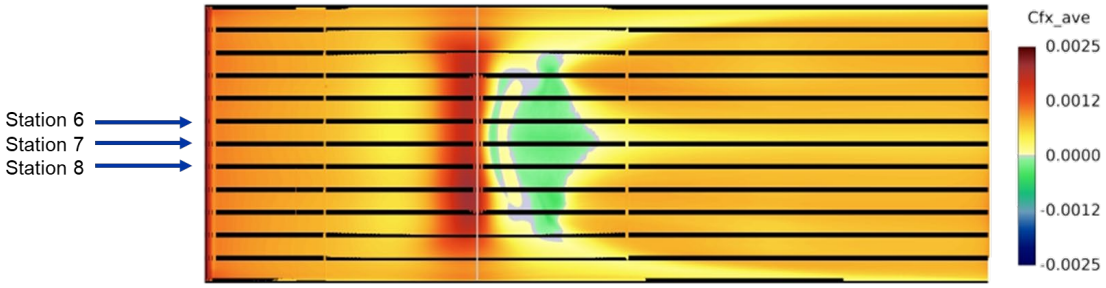

Figure 47: Plan view of forward-bump position colored by the time-averaged x-component of skin friction, and depicting the spanwise stations (horizontal black lines) at which skin friction was extracted from the simulation to compare with test data.

Comparisons at all three stations for the forward bump (Mach 0.1) results are shown in Figure 48-Figure 50. It should be noted that while the simulation results vary from Figure 48-Figure 50, the test data is a mix of measurements from stations 6-8, and is the same dataset plotted in Figure 48-Figure 50. DDES (blue line) matches the test data very well for all three stations at points far and immediately upstream of the apex (x/L=0), with particularly good agreement along Station 8. Downstream of reattachment, DDES along Stations 6 and 8 compares favorably with the test data. Along Station 7 (centerline), where there is significant upwash downstream of the bump due to the formation of a pair of streamwise-oriented, counter-rotating vortices, DDES under-

predicts the test data. It should be noted that the DNS results are for a two-dimensional extrusion of the centerline bump profile. Therefore, there is no significant spanwise variation in the time-averaged flow. This is somewhat analogous to the fully three-dimensional DDES results at Stations 6 and 8 (+/- 3" off centerline), where the upwash/downwash field is locally neutral near x/L = 0.5. This explains the good agreement between DDES and DNS downstream of the apex at Stations 6 and 8.

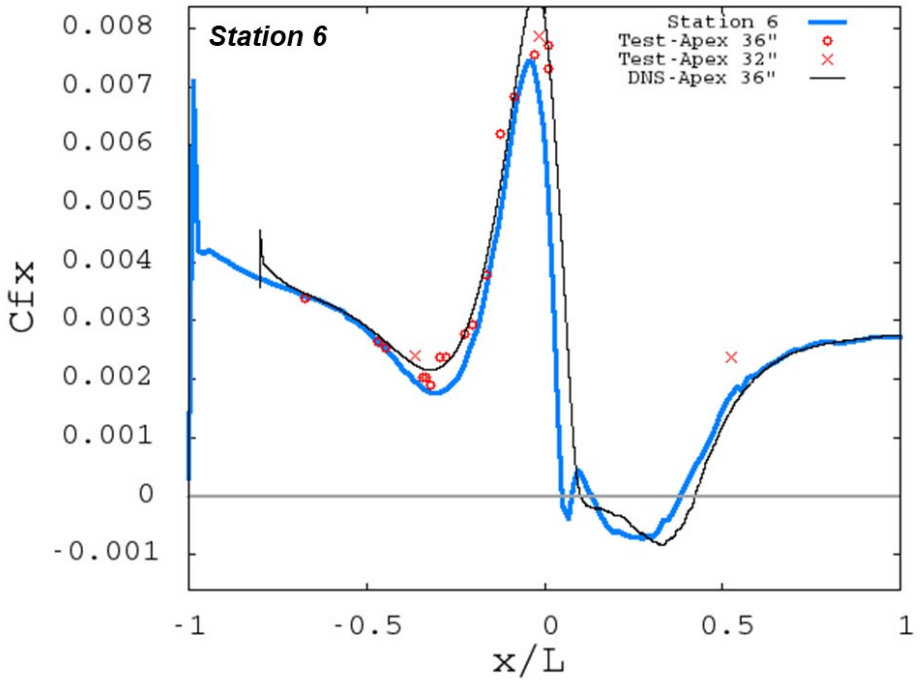

Figure 48: Time-averaged skin friction comparison along Station 6 between the 32" and 36" bump apex locations from test (x and o, respectively), the 36" bump location from DDES (blue line), and the 36" bump location from DNS by Uzun and Malik (black line).

Similar comparisons between DDES and OFI for the aft bump (72" apex location) at Mach 0.1 and Mach 0.2 are given in Figure 51 and Figure 52, respectively. It should be noted that while the simulation results vary from one station sub-plot to the next, the test data is a mix of measurements from stations 6-8, and is the same dataset plotted in on each station sub-plot. At Mach 0.1 (Figure 51), exceptional agreement between DDES and test is realized upstream of the bump, at the apex, and downstream of reattachment along Stations 6 and 8. At Station 7 DDES is once again observed to under-predict the data, which suggests that this OFI data point was taken closer to Stations 6 or 8, where upwash is nearly neutral. At Mach 0.2 (Figure 52) the comparison matches the foregoing discussion, with the exception of the upstream-most comparison point. It is observed that for x/L ~ -0.75 the test point falls below the DDES curve. Given the good agreement at this location for the forward and aft bumps at Mach 0.1, it seems this particular OFI measurement may have been compromised. However, this is speculation and the cause of this difference is currently not known.

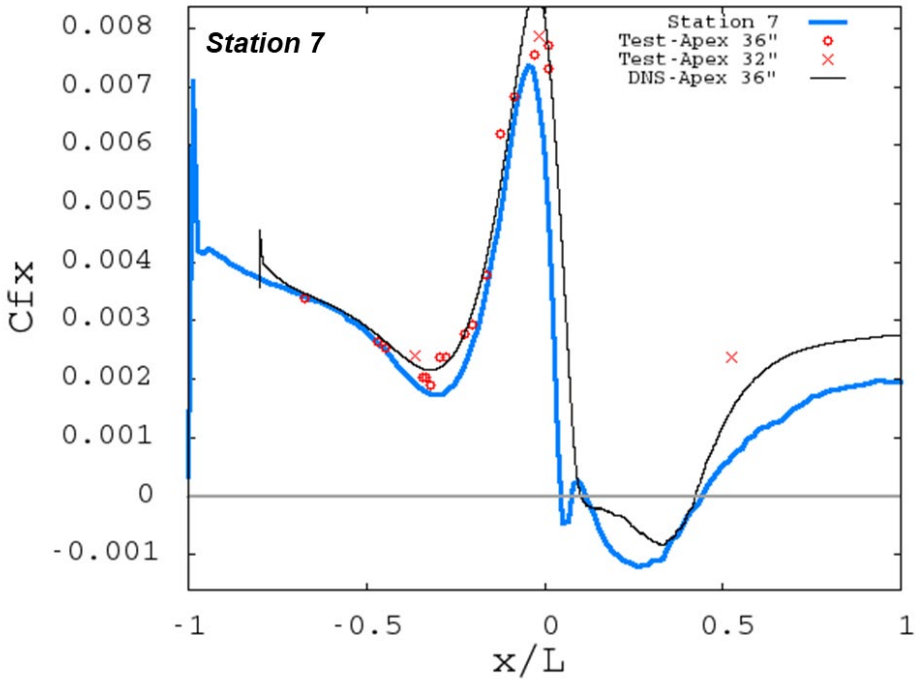

Figure 49: Time-averaged skin friction comparison along Station 7 between the 32" and 36" bump apex locations from test (x and o, respectively), the 36" bump location from DDES (blue line), and the 36" bump location from DNS by Uzun and Malik (black line).

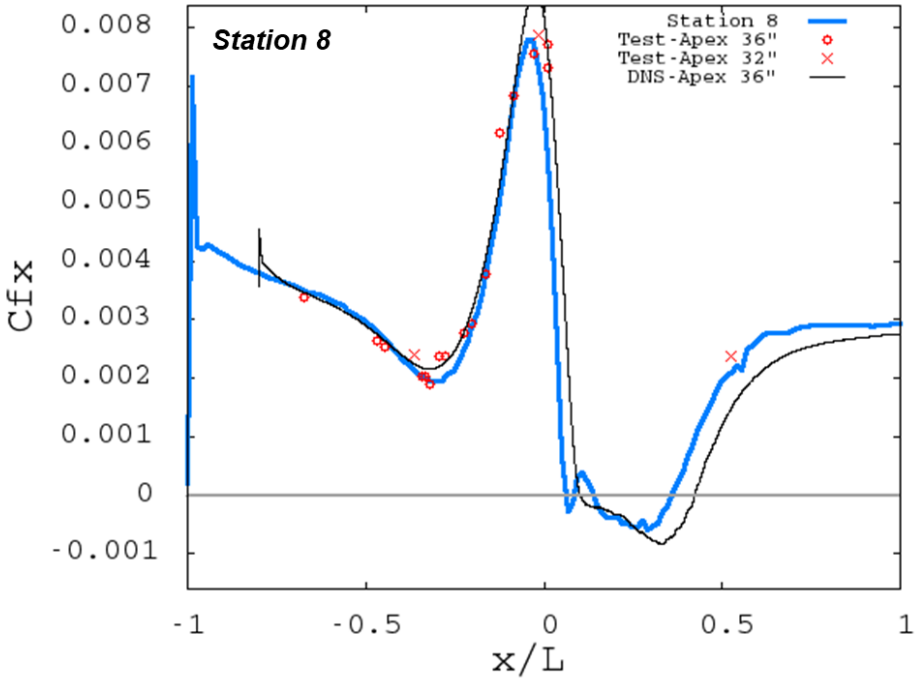

Figure 50: Time-averaged skin friction comparison along Station 8 between the 32" and 36" bump apex locations from test (x and o, respectively), the 36" bump location from DDES (blue line), and the 36" bump location from DNS by Uzun and Malik (black line). Mach 0.1.

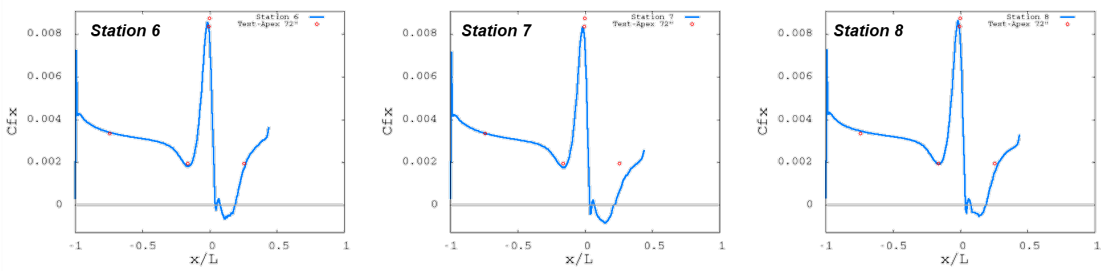

Figure 51: Time-averaged skin friction comparison along Stations 6-8 between the 72" bump apex location from test (red o symbols), and the 72" bump location from DDES (blue line). Mach 0.1.

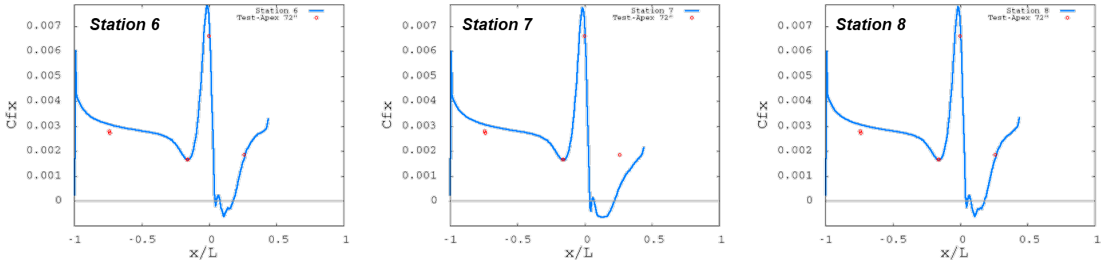

Figure 52: Time-averaged skin friction comparison along Stations 6-8 between the 72" bump apex location from test (red o symbols), and the 72" bump location from DDES (blue line). Mach 0.2.

Following comparison to the aforementioned preliminary OFI measurements, additional OFI measurements were taken with greater spatial resolution along the bump. Figure 53 shows a collection of all the experimental OFI measurements taken for Mach 0.05, 0.1, and 0.2 at the forward and aft bump positions. The trends in skin friction upstream of the bump for Mach 0.1 and 0.2 vary as expected with changes in Mach number and bump location (i.e., Reynolds number), however the Mach 0.05 skin friction ahead of the bump is unexpectedly low, and was therefore assumed to have not been effectively tripped to turbulence. For this reason, comparisons were only made to the Mach 0.1 and 0.2 data shown in Figure 53. At the forward bump position (36" apex location), two conditions corresponding to Mach 0.1 and ReL ~ 2e6 (L = 3'), and Mach 0.2 and ReL ~ 4e6, were compared. For the aft bump position (72" apex location), two conditions corresponding to Mach 0.1 and ReL ~ 2e6, and Mach 0.2 and ReL ~ 4e6, were compared. The time-averaged, x-component of skin friction was

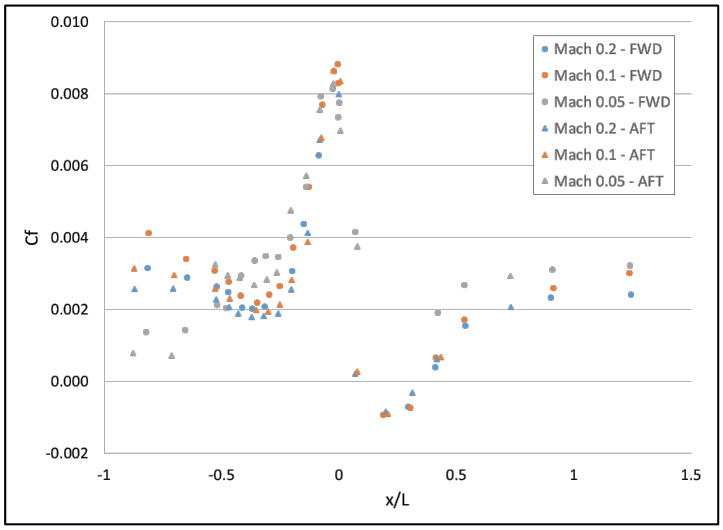

Figure 53: Skin friction data plotted for all experimental OFI

ONR Contract Number N00014-20-2-1002

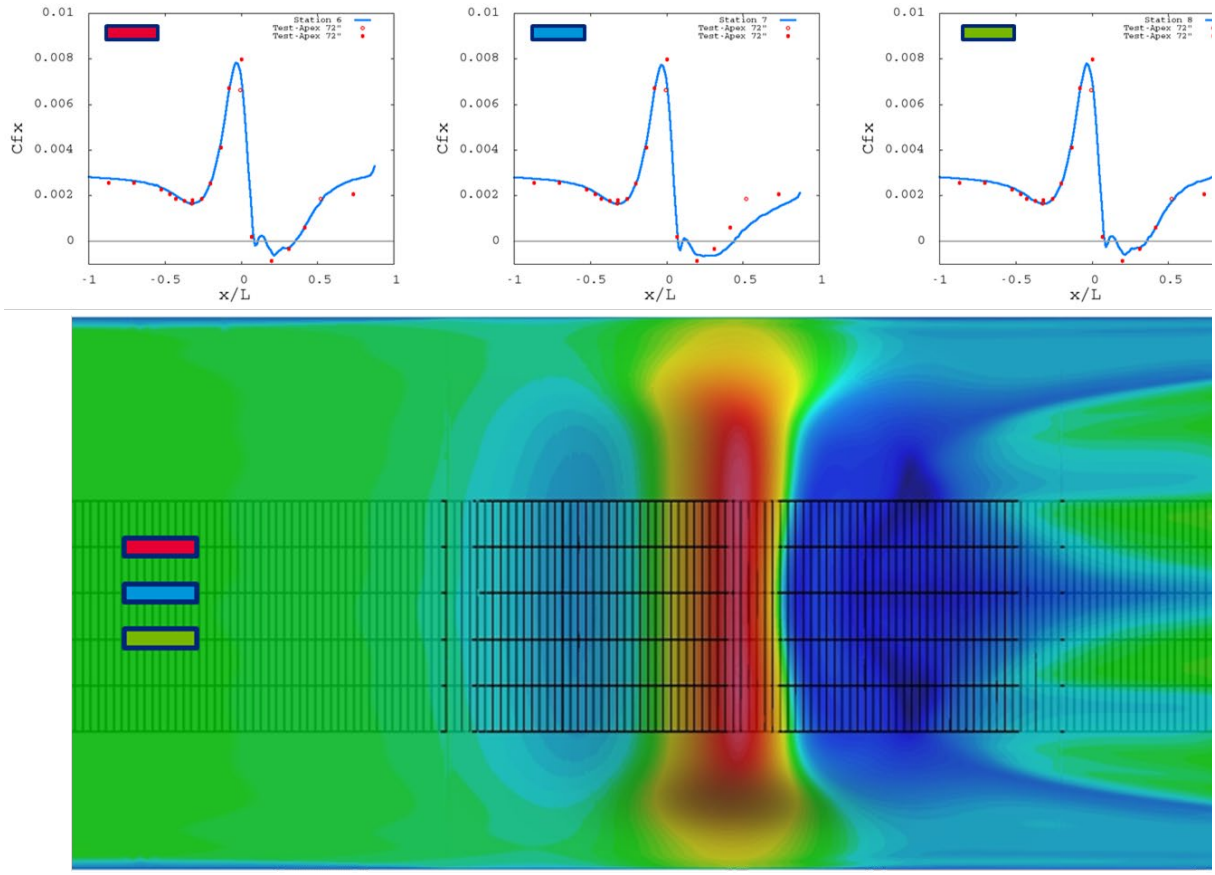

Figure 54: Skin-friction profiles (top) and contours (bottom) for the aft-mounted bump at Mach 0.2. Experimental measurements (red symbols) are the same for each top plot, while the DDES results (blue curves) change spanwise location as indicated by the colored rectangles.

extracted from the DDES along the centerline and stations +/- 3 inchess off-centerline, and compared with the test data. Figure 54 shows one such comparison made for the aft-mounted bump (i.e., apex at 72 inches downstream of plate leading edge) at Mach 0.2. Boundary-layer conditions upstream of the bump are observed to agree well between test and CFD. Excellent agreement continues to the point of separation just downstream of the apex, with the exception of the peak-Cf location, which is predicted to occur just upstream of the apex, while the test measurement indicates nearly exact alignment of the Cf peak with the apex. It is interesting to note that agreement downstream of separation, including reattachment and subsequent Cf rise, matches nicely (except for the downstream-most experimental data point) for the stations +/- 3 inches off centerline, but not quite as well at the centerline. The current working hypothesis is that this may be due to a difference in the trailing-edge flap setting, which is neutral in the simulation, but deflected 2-degrees upward in the test. Simulations with the flap deflected upward 2 degrees will be conducted to test this hypothesis.

Simulations were also performed for the other 3 conditions (i.e., forward bump at Mach 0.1 and 0.2, and aft bump at Mach 0.1) but plots of skin friction on the plate revealed asymmetries in the boundary layer ahead of the bump, such as those seen in Figure 55.

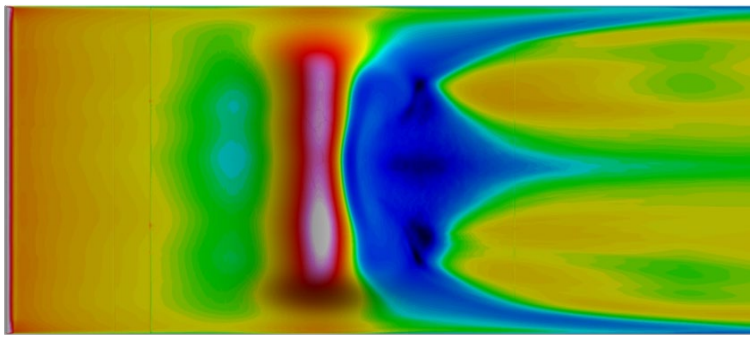

Figure 55: Time-averaged skin-friction contours revealing asymmetries developing upstream of the bump, caused by non-physical flow perturbations.

After some investigation it was determined that non-physical, very-low-frequency perturbations developing near the inflow boundary were causing unsteady forcing of the flow upstream of the plate, thereby introducing waves into the flat-plate boundary layer which manifest as the upstream asymmetries observed in Figure 55. Subsequent investigation has led to findings which suggest that lack of convergence caused by interaction of very low inflow Mach numbers and the low-dissipation, inviscid-flux scheme is the cause of these non-physical perturbations.

A comparison between skin-friction contours generated with (left) and without (right) the low-dissipation flux scheme is presented in Figure 56. Contours were generated with non-identical color map levels so the legend is omitted, but the point is to illustrate that simulating without the inviscid flux scheme results in a more physically reasonable upstream distribution. Despite using the default, upwinded second-order flux calculation, skin-friction predictions are still reasonable as shown in Figure 57.

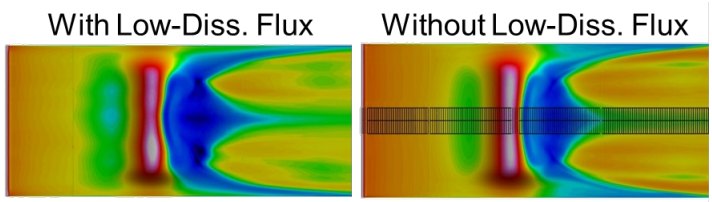

Figure 56: Skin friction contours for the forward bump at Mach 0.1.

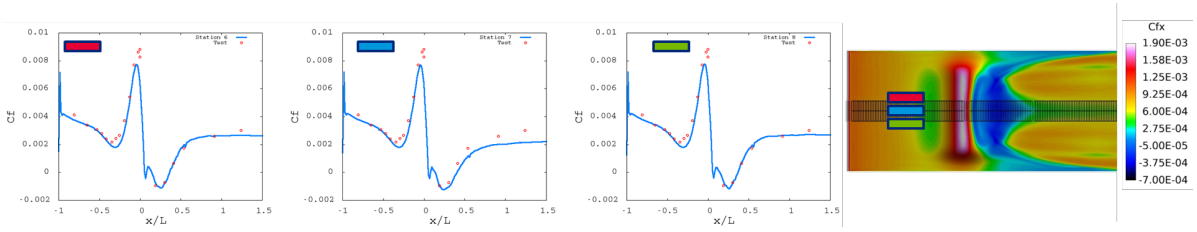

Figure 57: Skin friction distributions for the forward bump at Mach 0.1.

One area where the predictions exhibit some difference from test is at the apex (x/L = 0), where the simulations are sometimes observed to under predict the measured peak skin friction. To investigate this further, sensitivity to RANS model was explored by repeating the simulation using SA in the RANS region, instead of SA-RC-QCR as plotted previously. Skin-friction distributions for the aft-bump location at Mach 0.2 are shown in Figure 58 for three spanwise locations using both SA and SA-RC-QCR for the RANS region of the DDES simulation. Upstream of the apex both sets of simulations match the test data and each other very closely. SA clearly does a better job of predicting the peak skin-friction value, however SA-RC-QCR

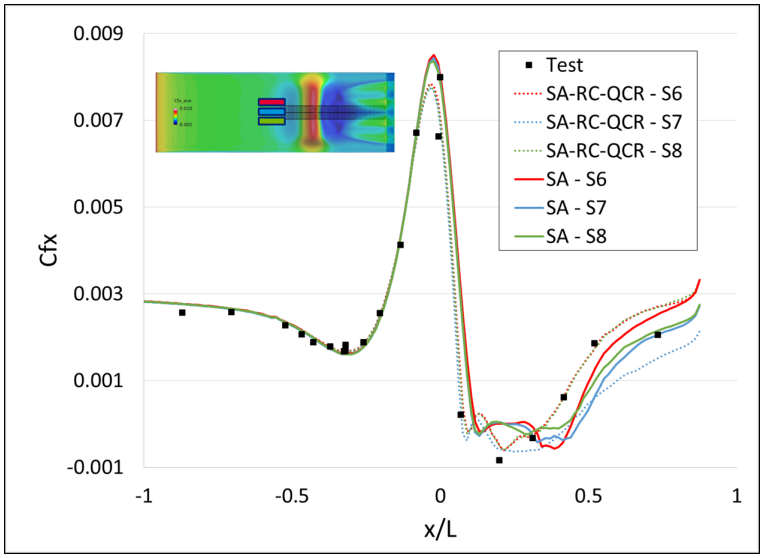

Figure 58: Time-averaged DDES skin friction distributions and OFI measurements for the aft bump at Mach 0.2. The three line colors correspond to the three spanwise locations denoted in the insert.

agrees better with the test downstream of the apex. Given the well-known result that use of the streamline-curvature correction reduces eddy viscosity, it is not surprising to see that the DDES result using SA predicts a greater peak skin friction than the DDES results using SA-RC-QCR. It is presumed that QCR has a negligible impact on this result, and that the RC changes to the SA model are primarily responsible for this sensitivity.

6) Comparisons with Hot-Wire Measurements

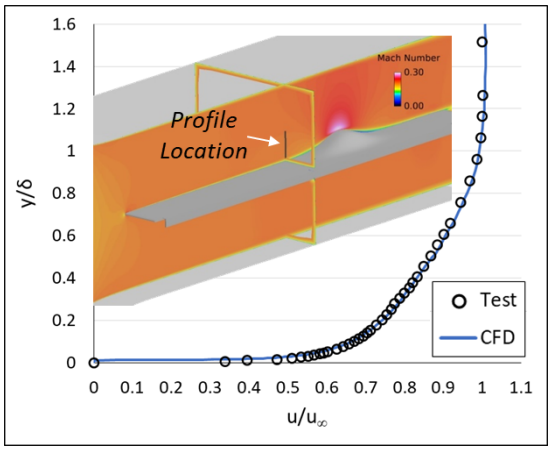

Figure 59: Comparison of boundary-layer profile along the upper surface of the splitter plate.

Figure 59 shows a comparison between test and CFD for the splitter-plate boundary layer at a test-section Mach number of approximately 0.2. The measurement from test was taken without the bump present, while the profile from CFD was from an SST-QCR simulation with the bump installed at the aft-most location along the plate. Despite this geometry difference, the boundary-layer profiles at the measurement location, which is just upstream of the bump test article in the CFD, are in excellent agreement.

For the case of the bump located in the aft-most position, hotwire measurements were taken at the seven stations shown in Figure 60 at Mach~0.2.

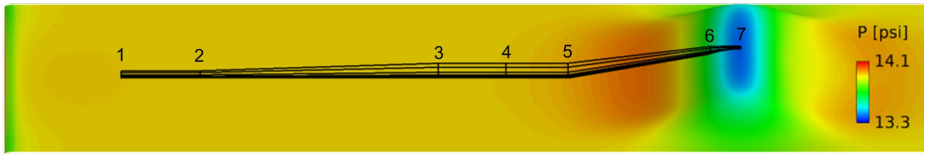

Figure 60: Hotwire-measurement stations for the aft bump at Mach ~0.2.

ONR Contract Number N00014-20-2-1002

Comparisons between CFD and hotwire are shown in Figure 61 for each of the seven stations. The 'RANS' profiles shown in each plot are from simulations made with the SA-RC-QCR turbulence model, the 'DDES' profiles used SA-RC-QCR for the RANS portion of the simulations, and 'SA-DDES' used SA for the RANS portion of the simulation. The comparisons for stations 1 and 2 suggest that the experimental boundary

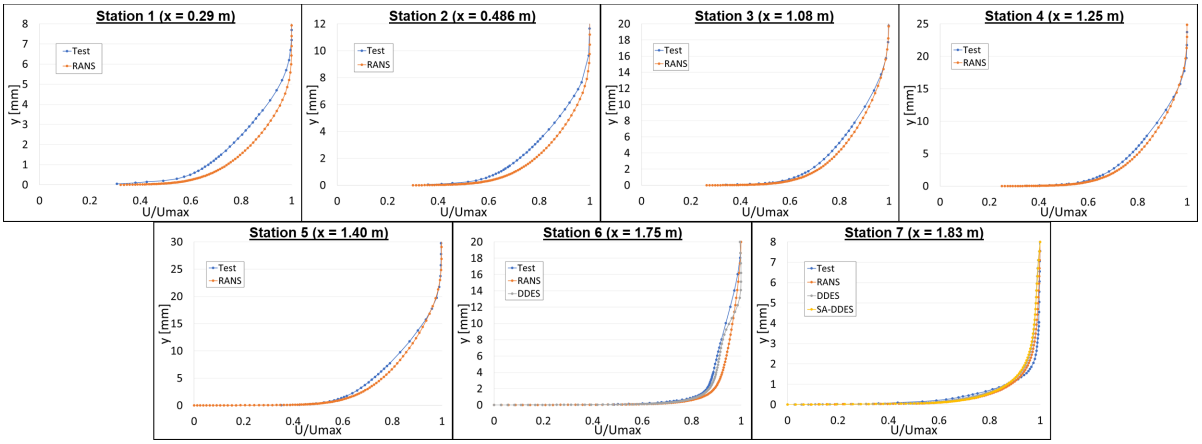

Figure 61: Hotwire compared with CFD for the aft bump at Mach ~0.2.

hasn't fully developed to a canonical turbulent state, particularly because of the shallower near-wall gradient relative to the fully turbulent RANS profiles. At station 3 the profile appears to be fully turbulent, with only a slight mismatch between Test and RANS in the middle portion of the boundary layer. Based on the results from Section 1, this difference is likely nearly if not completely accounted for by the experimental uncertainty, however another potential cause is a wake effect induced by the trips in the experiment. Moving downstream to stations 4 and 5, it can be seen from Figure 60 that the flow has entered the region of adverse pressure gradient upstream of the bump. The comparisons between Test and RANS for stations 4 and 5 echo the findings at station 3. At station 6 the flow has entered the strong favorable pressure gradient approaching the apex which is observed from Figure 61 to produce the expected reduction in boundary-layer thickness. This is also the first station since the flow became fully turbulent that RANS is unable to produce satisfactory agreement with the Test profile. The DDES profile plotted in Figure 61 for station 6 shows very good agreement with Test up to y ~ 9 mm, at which point the profile experiences a rapid increase in velocity toward the edge of the boundary layer. This has been demonstrated previously to be an artifact of the wall-normal transition between the RANS and LES portions of the DDES simulation.

The fact that DDES is superior to RANS below y ~ 9 mm suggests that the dynamic nature of the boundary-layer separation downstream of the apex is influencing boundary-layer development upstream of the apex. This explanation seems plausible because the recirculation predicted by RANS is confined very close to the wall and does not develop to the level observed in Test and predicted with DDES. Finally, at station 7 (i.e., the bump apex), the flow is leaving the favorable pressure gradient and entering the adverse

gradient downstream of the apex. The boundary-layer thickness is observed to have decreased dramatically from station 6, and all CFD results over-predict the Test velocity below y ~ 1 mm, and under-predict the Test velocity between y ~ 1 mm and the freestream. It is also worth noting that there is very little difference in the profiles predicted by RANS, DDES, and SA-DDES at this station. Despite the aforementioned differences between Test and CFD at station 7, the magnitude of the differences is quite small, and could very well be within the experimental uncertainty.

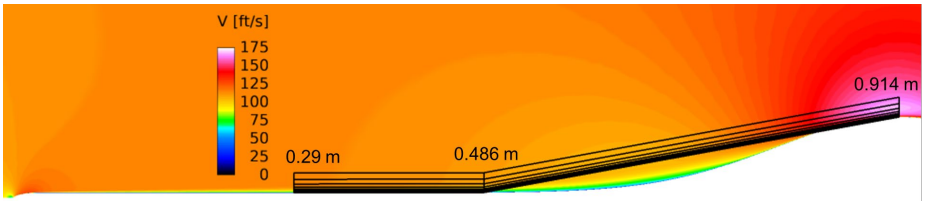

Figure 62: RANS Mach contours for Mach ~ 0.1 test-section Mach number.

For the case of the bump apex located at 36", hotwire measurements were taken at the three stations shown in Figure 62 and Figure 63 for oncoming Mach numbers of 0.1 and 0.2, corresponding to Re/L ~ 2e6 and 4e6. The distances depicted in these figures are measured in the x-direction downstream of the leading edge of the splitter plate. Comparisons between CFD and hotwire are shown in Figure 64 for each of the three stations at Mach 0.1, and in Figure 65 for each of the three stations at Mach 0.2. The 'RANS' profiles shown in each plot are from simulations made with the SA-RC-QCR turbulence model, the 'DDES' profiles used SA-RC-QCR for the RANS portion of the simulations, and 'DDES-fine' used a mesh where the surface-element spacing was reduced from 0.2 inches (i.e., the resolution used in the mesh that generated the 'DDES' profiles) to 0.06 inches ahead of the bump apex.

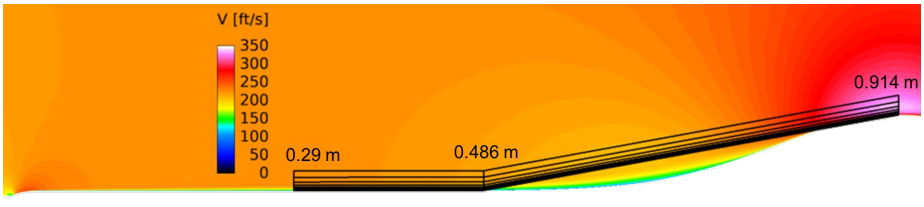

Figure 63: RANS Mach contours for Mach ~ 0.2 test-section Mach number.

The Mach-0.1 comparisons shown in Figure 61 exhibit overall good agreement between RANS and hotwire measurements. At x = 0.29 m the RANS profile matches well near the wall and then farther away from the wall presents as a fuller profile, or perhaps a

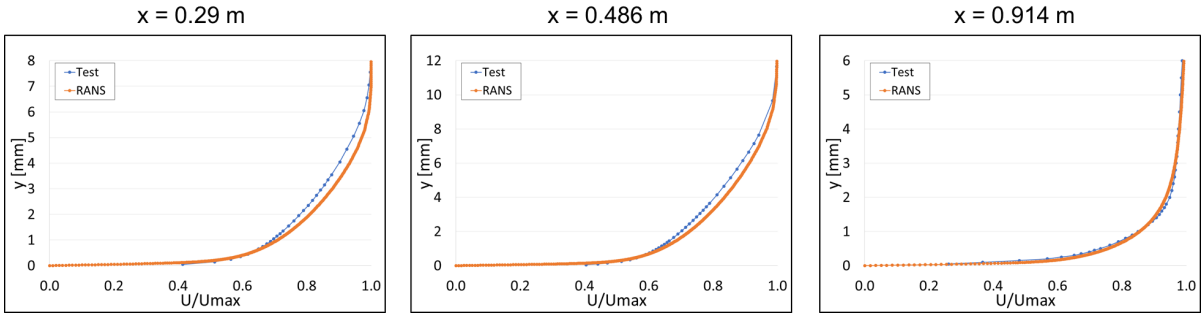

Figure 64: Hotwire compared with CFD for the forward bump at Mach ~0.1.

ONR Contract Number N00014-20-2-1002

thinner boundary layer than what was measured in the test. At x = 0.486 the comparison is qualitatively similar to that at x = 0.29 m but the difference between RANS and test is less pronounced, and both RANS and test profiles show approximately 4 mm of growth in the boundary-layer thickness from x = 0.29 m. Based on previous analysis for the aft-located bump, there is a strong likelihood that the observed difference between RANS and test at these stations is due primarily to the wake generated by the boundary-layer trips, which are not included in the RANS analysis. This theory is consistent with the diminishing difference observed between RANS and test at locations farther from the leading edge of the splitter plate, but still upstream of the bump. At x = 0.914 m RANS agrees very well with the hotwire measurement, and the boundary layer is thinned considerably due to the strong favorable pressure gradient approaching the apex.

Mach 0.2 comparisons are presented in Figure 65. At x = 0.29 m the three CFD simulations predict the same results, which like the Mach 0.1 comparison, slightly over-predict velocity throughout much of the profile measured by hotwire. At x = 0.486 m the difference between test and CFD generally increases throughout the profile relative to the comparison at x = 0.29 m. RANS and DDES predict the same profile, and DDES on the fine grid predicts slightly lower velocities up to y ~ 6 mm, and slightly greater velocities for y > 6 mm. Previous analysis has demonstrated that the distinct 'jog' in the fine-grid DDES profile near y = 6 mm is caused by the transition from the RANS region to the LES region of the simulation. The overall greater difference between test and CFD at this station contrasts the results at Mach 0.1, which showed better agreement moving away from the leading edge of the splitter plate. This is explained by the larger and more dynamic separation downstream of the apex at Mach 0.2 compared to Mach 0.1, which has a more noticeable impact on the profiles near the apex, and even farther upstream in the region of adverse pressure gradient around x = 0.486m. Finally, at x = 0.914 RANS and DDES once again agree very closely with one another, and with the hotwire measurements for y above approximately 1.5 mm. Below 1.5 mm the measured profile is less full than the RANS and DDES predictions. One possible reason for this is that the simulations made with RANS and DDES tend to under-predict the size of the separated-flow region downstream of the apex, and of course RANS completely neglects any dynamics of the separation. The fine-grid DDES, however, does a better job of predicting flow downstream of the apex in the separation/reattachment region, and also

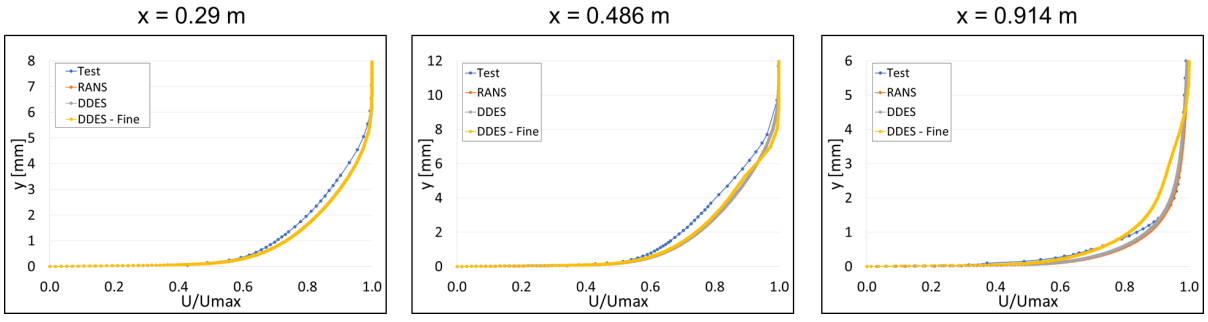

Figure 65: Hotwire compared with CFD for the forward bump at Mach ~0.2.

does a better job of predicting the near-wall profile (y < 1 mm) than RANS and the

ONR Contract Number N00014-20-2-1002

coarser-grid DDES. This suggests that at Mach 0.2 (and likely Mach greater than 0.2), in order to accurately predict boundary-layer development on the windward half of the bump, the separation on the leeward half must be accurately predicted because of its tendency to influence the upstream pressure-distribution.

7) Comparisons with Surface-Pressure Measurements

Measurements of surface pressure were taken along the three streamwise-running paths, and the two spanwise-running paths depicted in Figure 66. Simulations were made with RANS (SA-RC-QCR) and DDES using SA-RC-QCR in the RANS regions on grids with two resolution levels. The baseline, or 'fine' grid, used triangular surface elements over the plate and bump measuring ~1.6 mm (0.0625") on each side. The 'coarse' grid is topologically identical to the fine grid except that the plate upstream of the apex was coarsened such that the triangles measured ~5 mm (0.2") on each side. This was motivated by previous studies indicating that modeled stress depletion caused the approach boundary layer, predicted by DDES, to develop in a way not consistent with the experiment. Therefore, the coarser approach mesh serves to more fully shield the boundary layer within the RANS region of the simulation upstream of the apex. The RANS results are largely insensitive to differences between the coarse and fine grids used here.

Comparisons for Z = 0 are shown in Figure 67. On the coarse grid both RANS and DDES agree with one another and the test data ahead of the apex. At the apex RANS over-predicts DDES, which in turn over-predicts the experimentally measured suction peak. Downstream of the apex RANS fails to predict separation, while DDES captures the test trend reasonably well, predicting separation slightly farther downstream. On the fine grid DDES is observed to differ slightly from RANS ahead of the apex, owing to modeled stress depletion, and now under-predicts the suction peak relative to test. Downstream of the apex DDES is observed to separate slightly upstream of the test, and exhibits very good agreement with pressure variations farther downstream.

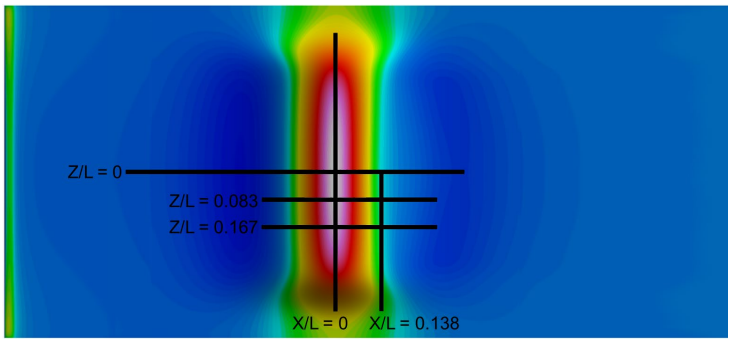

Figure 66: Five surface-pressure measurement paths used for comparison

ONR Contract Number N00014-20-2-1002

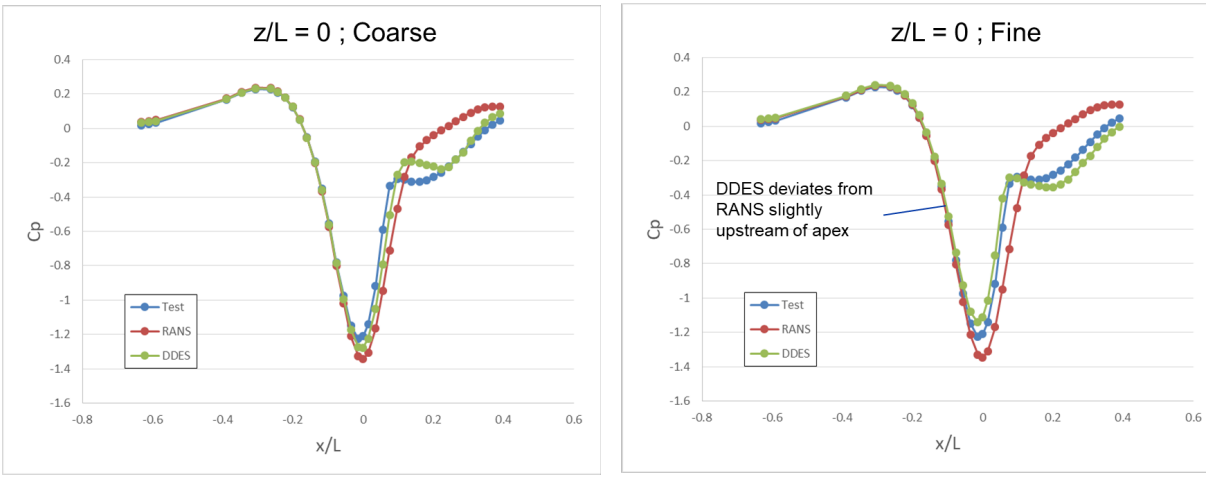

Figure 67: Surface-pressure comparisons along the bump centerline.

The comparison at the first off-centerline station is shown in Figure 70. RANS once again over-predicts the suction peak and fails to predict separation, but on the coarse mesh DDES agrees well with the test data up until separation and then loosely agrees with the test data following separation. On the fine mesh DDES under-predicts the peak, separates just upstream of the test data, and then captures the experimental trend in pressure rise downstream of reattachment.

Moving to the second off-centerline station in Figure 68 we once again observe RANS over-predicting the suction peak, but only very slightly in this case. Furthermore RANS does a very good job of matching the pressure downstream of the apex up to x/L ~ 0.1. The reason for this more favorable agreement downstream of the apex at this spanwise location becomes clearer when you consider that the test data indicates no obvious separation. DDES on the other hand under-predicts the suction peak, a problem which is only exacerbated on the fine mesh, and predicts separation on both the coarse and fine grids, inconsistent with the test data. DDES has been shown in previous PIV comparisons to generally over-predict the streamwise and spanwise extent of the

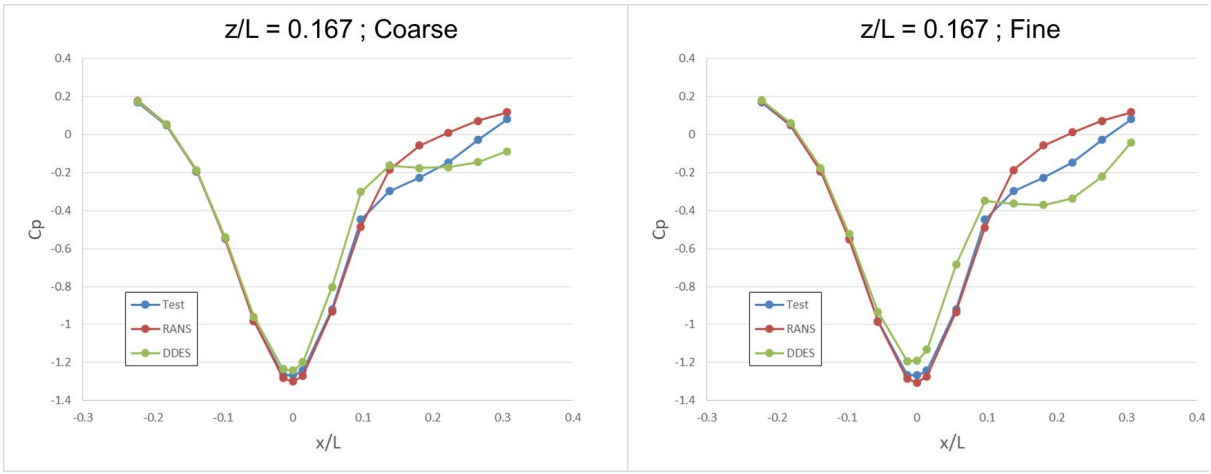

Figure 68: Surface-pressure comparisons along the bump 152.4 mm (6") off centerline.

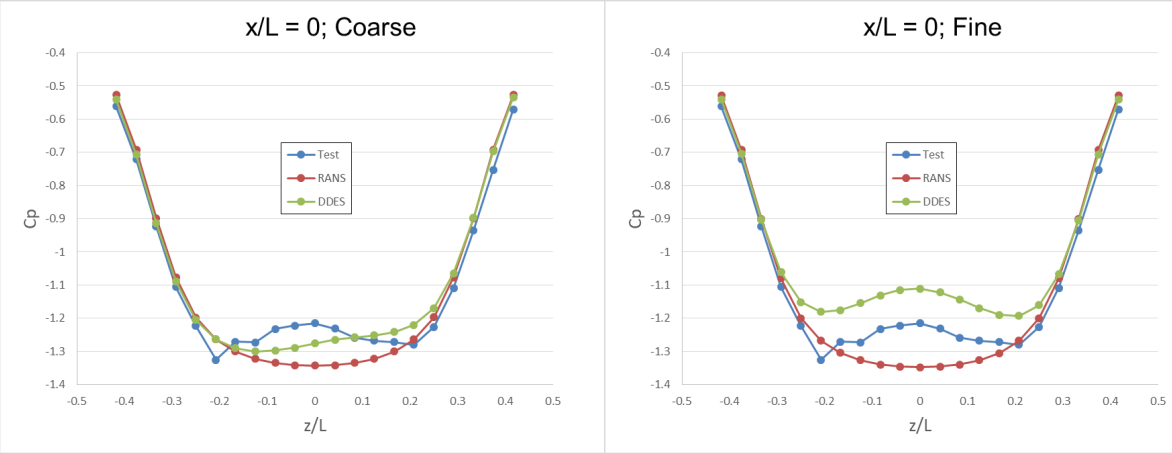

Figure 69: Surface-pressure comparisons along the bump apex.

separated-flow region, which is reflected in the comparisons of test and DDES between z/L = 0.038 and z/L = 0.167.

Switching to spanwise-running pressure data, Figure 69 shows the comparison at the apex. The test data exhibits two suction peaks near |z/L| ~ 0.2 with a local maximum at the centerline (i.e, z/L = 0). On the coarse grid, both RANS and DDES predict similar pressures for |z/L| > 0.2, and agree very well with the test data for |z/L| > 0.25. However, RANS misses the dual suction peaks prominent in the test data, while DDES appears to predict two asymmetric suction peaks. The clear asymmetry in the time-averaged DDES data is the result of the proximity of the apex to the change in surface-mesh resolution, which causes spanwise variation in the wall-normal transition location between the RANS and LES regions of the simulation, which is in turn reflected in the spanwise asymmetry observed in the DDES results on the coarse mesh. On the fine mesh DDES only agrees closely with test for |z/L| > 0.3, but the spanwise variation is capture very nicely, and the result exhibits a high degree of symmetry. Indeed, the difference between DDES and test on the fine mesh appears to be a nearly constant offset for |z/L| < 0.2 of approximately ΔCp = 0.1. This suggests that DDES is capturing the salient physical aspects of the experimental flow field downstream of the apex, with a slightly different separation location.

Finally, the spanwise-running comparison over half of the bump at x/L = 0.138 is shown in Figure 71. On the coarse mesh the Cp magnitude of both RANS and DDES are similar and in generally poor agreement with the test, but DDES exhibits some similarity to test in terms of the spanwise pressure variation. On the fine mesh DDES agrees more closely with the test than on the coarse mesh both in terms of pressure magnitude and spanwise variation, with the most notable qualitative discrepancy being that DDES predicts the suction peak farther from centerline. Another interesting qualitative feature of all profiles (i.e., Test, RANS, and DDES) on either mesh is a distinct change in the nature of spanwise variation near z/L = 0.25. That is, the pressure appears to be dominated by one thing, likely recirculation, inboard of |z/L| ~ 0.25, and another thing, likely geometry, outboard of |z/L| ~ 0.25. This is made clearer by considering the time-averaged pressure and skin-friction contours for DDES on the fine mesh plotted in Figure 72. From the pressure contours we can clearly see the dual suction peak at x/L = 0 and 0.138, which plainly shows that the peak migrates toward the centerline moving downstream away from the apex. From Figure 73, which is just Figure 72 overlaid with skin-friction lines, we can see that the suction peaks corresponds to the symmetrically located critical points near x/L = 0.138. We can also see that the change in spanwise pressure variation near z/L = 0.25 correlates with the edge of the recirculation region depicted by skin-friction lines in Figure 73.

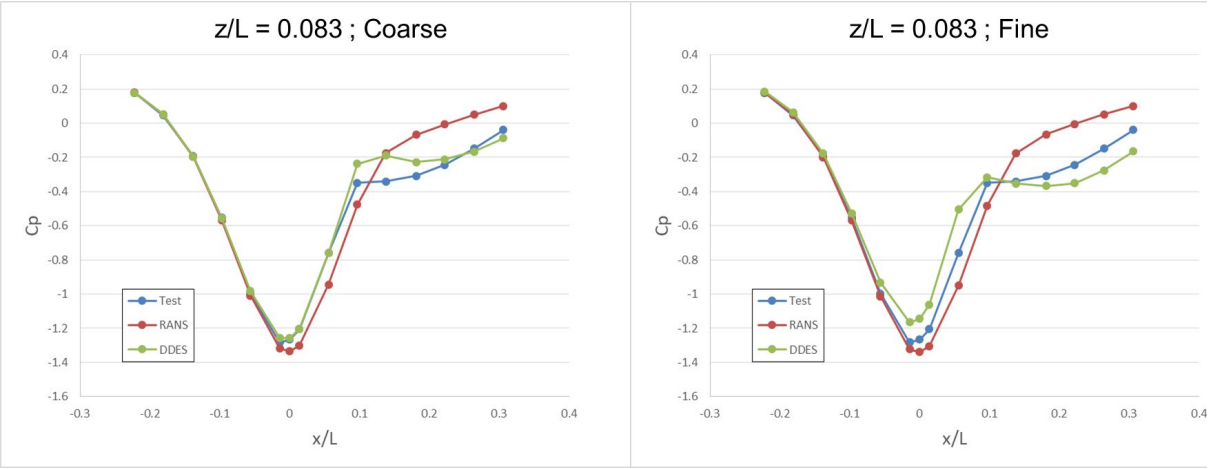

Figure 70: Surface-pressure comparisons along the bump 76.2 mm (3") off centerline.

To briefly summarize the surface-pressure comparisons, DDES on the coarse mesh does the best overall job of reproducing the test data, with the exception of the apex and the recirculation-dominated region downstream of the initial separation where the fine mesh excels. This highlights the sensitivity of accurate prediction of the separation location and subsequent flow development to the incoming state of the boundary layer, which is more accurately preserved on the coarse mesh due to better shielding of the boundary layer within the RANS portion of the simulation upstream of the apex. There is likely an 'optimal' mesh where coarsening would begin somewhere between the apex and the initial separation front. Based on the asymmetry observed in the current coarse-grid results care would need to be taken to ensure a spanwise-uniform RANS/LES transition location to avoid the development of asymmetries in the downstream flow. However, this goes down the path of tuning the grid to achieve known results for a particular flow,

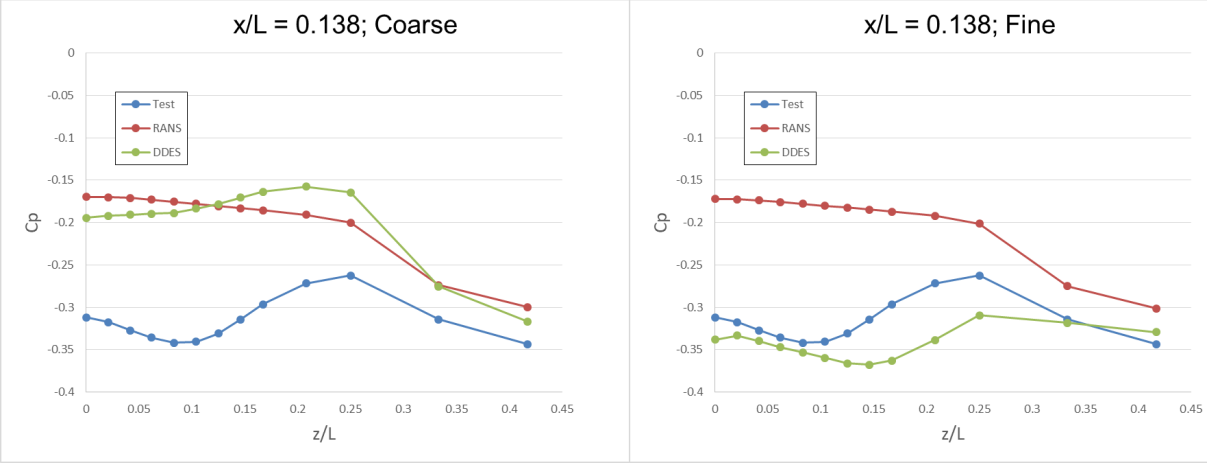

Figure 71: Surface-pressure comparisons along half of the bump 127 mm (5") downstream of the apex.

and will not ultimately result in a predictive simulation technique.

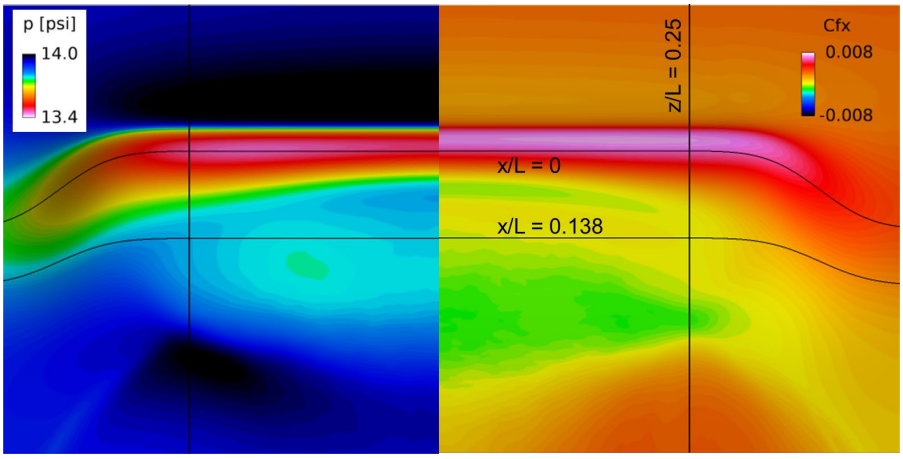

Figure 72: Surface-pressure contours (left) and contours for the x-component of skin friction (right) from DDES of the forward bump on the fine mesh. View is looking upstream.

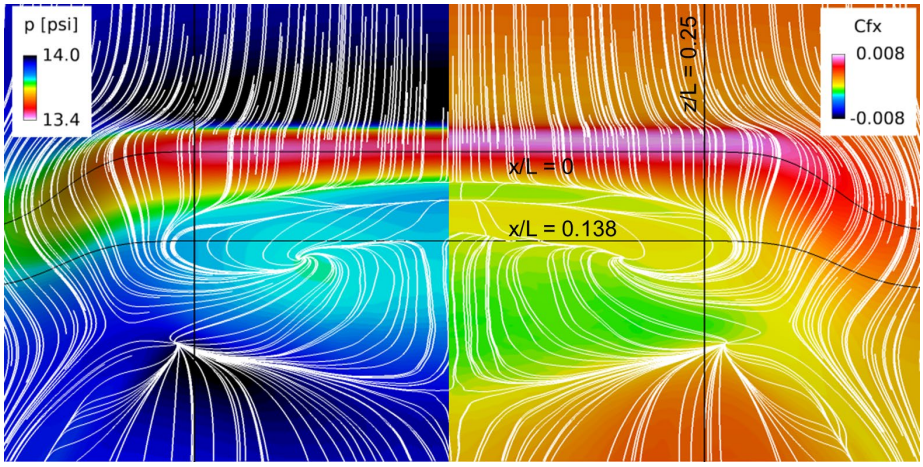

Figure 73: Surface-pressure contours (left) and contours for the x-component of skin friction (right) with skin-friction lines from DDES of the forward bump on the fine mesh.

8) Comparisons with Laser Doppler Velocimetry (LDV) Measurements

BCFD simulations of the forward (i.e., apex at x = 0.914 m) and aft (i.e., apex at x = 1.83 m) bumps were performed using RANS and DDES. SA-RC-QCR was used as the turbulence model in the RANS regions of these simulations. Total pressure and total temperature were set to nominally 14.3 psi and 533 R, and the test-section Mach number was approximately 0.2, providing close agreement with corresponding wind-tunnel entries used to acquire LDV measurements. Comparisons between CFD and LDV were made at five stations ahead of the forward-bump apex, and seven stations ahead of the aft-bump apex, as depicted in Figure 74.

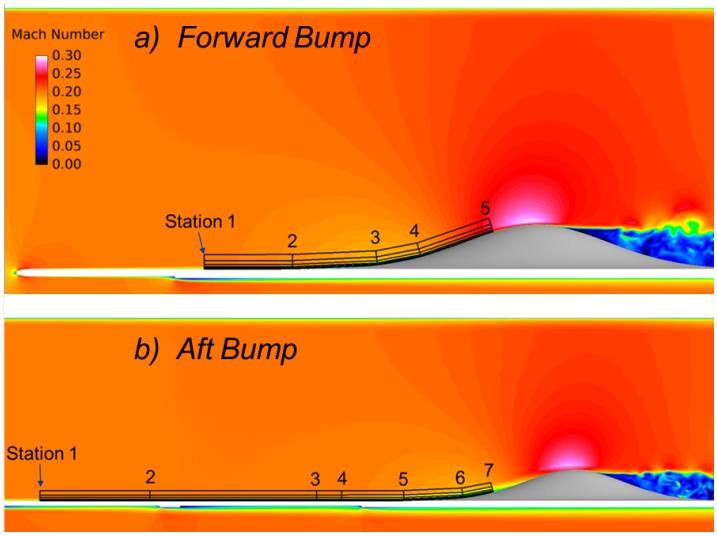

Figure 74: LDV measurement locations ahead of a) the forward-located bump, and b) the aft-located bump.

ONR Contract Number N00014-20-2-1002

RANS comparisons to the forward-bump LDV profiles were made for the Cartesian u and v components of velocity, and are shown in Figure 75. At the first two stations, u-velocity profiles indicate that the measured boundary layer is thinner than that predicted by RANS. Station 3 (x = 0.635 m) exhibits better agreement between LDV and CFD,

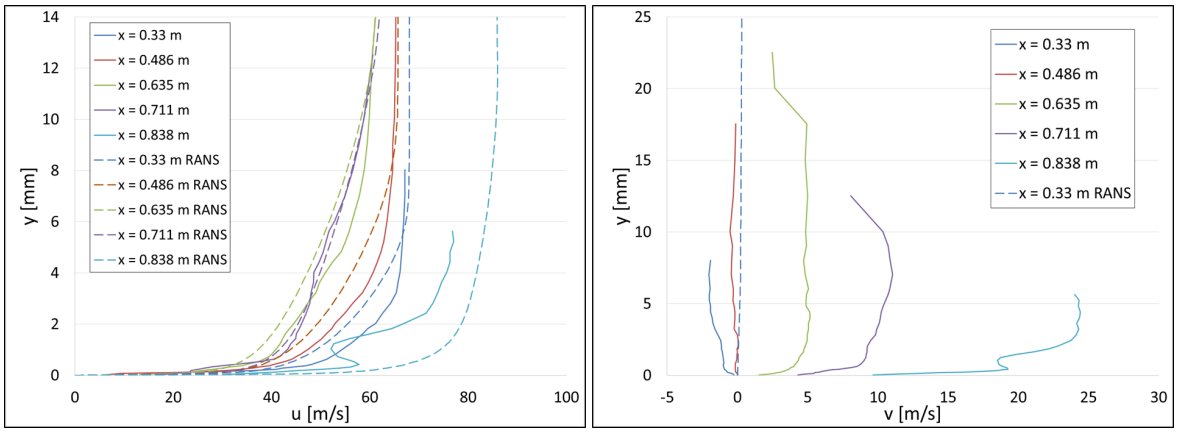

Figure 75: LDV (solid) and RANS (dashed) profiles of the u and v components of velocity at several stations ahead of the forward bump.

although the LDV profile is consistently more full, or faster, than the RANS profile. Very reasonable agreement is realized at station 4. At station 5, however, RANS and LDV differ greatly. One possibility for this is the proximity of station 5 to the more-unsteady portion of the flow downstream of the bump, and the inability of RANS to capture these unsteady effects. For the v-component of velocity, RANS is plotted for station 1, and has the expected flat-plate behavior of near-zero wall-normal velocity. This is in contrast to LDV which measures a significant flow toward the wall. The source of this downwash in the wind-tunnel test was determined to likely be caused by interference from the LDV seeding apparatus ahead of the splitter plate. Based on this finding, further comparisons with the forward-bump data were placed on hold, and focus was given to comparisons with the aft-bump measurements. Measurements of downwash

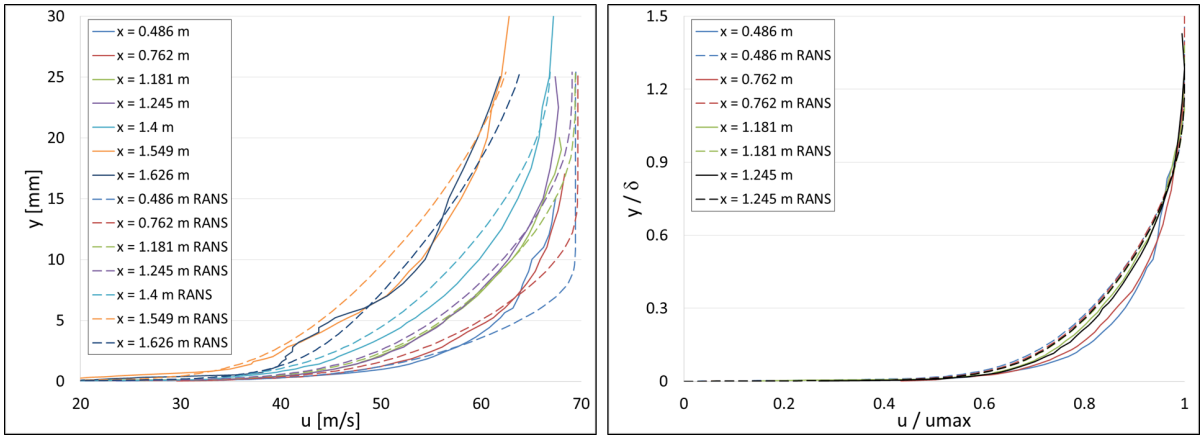

Figure 76: LDV (solid) and RANS (dashed) profiles of the dimensional (left) and scaled (right) u component of velocity at several stations ahead of the aft bump.

for the aft-bump max out at ~-0.5 m/s for stations 1-5, which is more consistent with the level of downwash at station 2 for the forward bump, and therefore more believable from physical or measurement-uncertainty perspectives. Comparisons between RANS and LDV for the aft bump are shown in Figure 76. Considering the dimensional data in the left plot of Figure 76, the velocity profiles at stations 1 and 2 measured by LDV are considerably slower than those predicted by RANS. Stations 3 and 4 are in very good agreement except for the outer-most portion of the profile, and stations 5-7 agree reasonably well. The data in the right plot of Figure 76 was scaled by the local boundary-layer thickness and maximum u-component of velocity. RANS for stations 1-4, as well as LDV for stations 3 and 4 collapse very well, whereas LDV profiles for stations 1 and 2 are fuller. This corroborates the observations from the dimensional profiles, and suggests that interference from the LDV seeding apparatus has contaminated these two profiles nearer the leading-edge of the splitter plate. The inner scaling of profiles from stations 1 and 3 is plotted in Figure 77. LDV data from station 1 (x = 0.486 m) was fit to the log layer by prescribing the necessary wall shear stress, and retains the log-layer slope both into the laminar sublayer and the freestream. This is in contrast to RANS which clings to the law of the wall from the viscous sublayer to y+ ~ 200, at which point it departs from the log layer. At station 3 (x = 1.181 m) the skin friction measured using OFI was used to scale the LDV data, which results in an offset from the log layer of roughly 1-2 u+ units. Near the wall, the LDV tends to follow the viscous sublayer better than at station 1, and departs from the log-layer slope near y+ ~ 500, which agrees well with RANS.

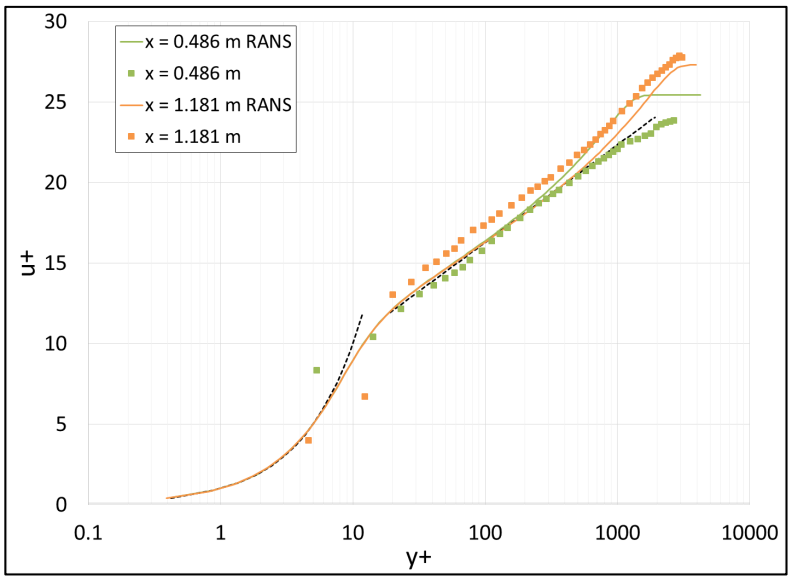

Figure 77: Velocity profiles ahead of the aft-located bump at Mach 0.2 from RANS (lines) and LDV (symbols).

In an effort to better understand the LDV measurements, comparisons of the aft-bump LDV were made with the year-1 hotwire measurements of the splitter-plate boundary layer with no bump installed. A 'no-bump' RANS simulation was also conducted and compared with LDV and hotwire at four stations in Figure 78. Due to alignment of LDV and hotwire measurement stations, LDV is only co-plotted at x = 0.49 m and x = 1.37 m. At x = 0.49 m the aft-bump (AB) and no-bump (NB) RANS profiles fall on top of each other, and lie between the LDV and hotwire profiles, which are significantly different from one another. The disagreement with LDV and hotwire at this station is unexpected given that it is sufficiently far upstream (Station 2 in Figure 74 b) that very little influence

of the bump should be felt. At x = 1.02 m the AB and NB RANS profiles are again indistinguishable and more full than the hotwire profile. At x = 1.37 m (Station 5 in Figure 74 b) the AB flow is in a region of adverse pressure gradient, which is reflected in the AB RANS profile having a deficit relative to the NB RANS profile. This trend, however, is reversed when considering the measurements, which show that the NB hotwire has a deficit relative to the AB LDV. Finally, at x = 1.73 m the NB hotwire exhibits a deficit relative to NB RANS similar to what is seen at the other stations.

Comparisons between inner scaling of RANS, hotwire, LDV and DNS are presented in Figure 79 for the first two stations shown in Figure 78. DNS was taken from Sillero et al. (https://torroja.dmt.upm.es/turbdata/blayers/high_re/profiles/). At x = 0.49 m, where Re-theta ~ 4000, RANS agrees very favorably with the DNS for Re-theta = 4000. LDV exhibits an elongated log layer while hotwire shows only a very thin log layer. This is in contrast to x = 1.02 m where the hotwire profile looks more like a canonical turbulent boundary layer, with a small offset from the zero pressure gradient log layer, and other minor differences above and below the log layer.

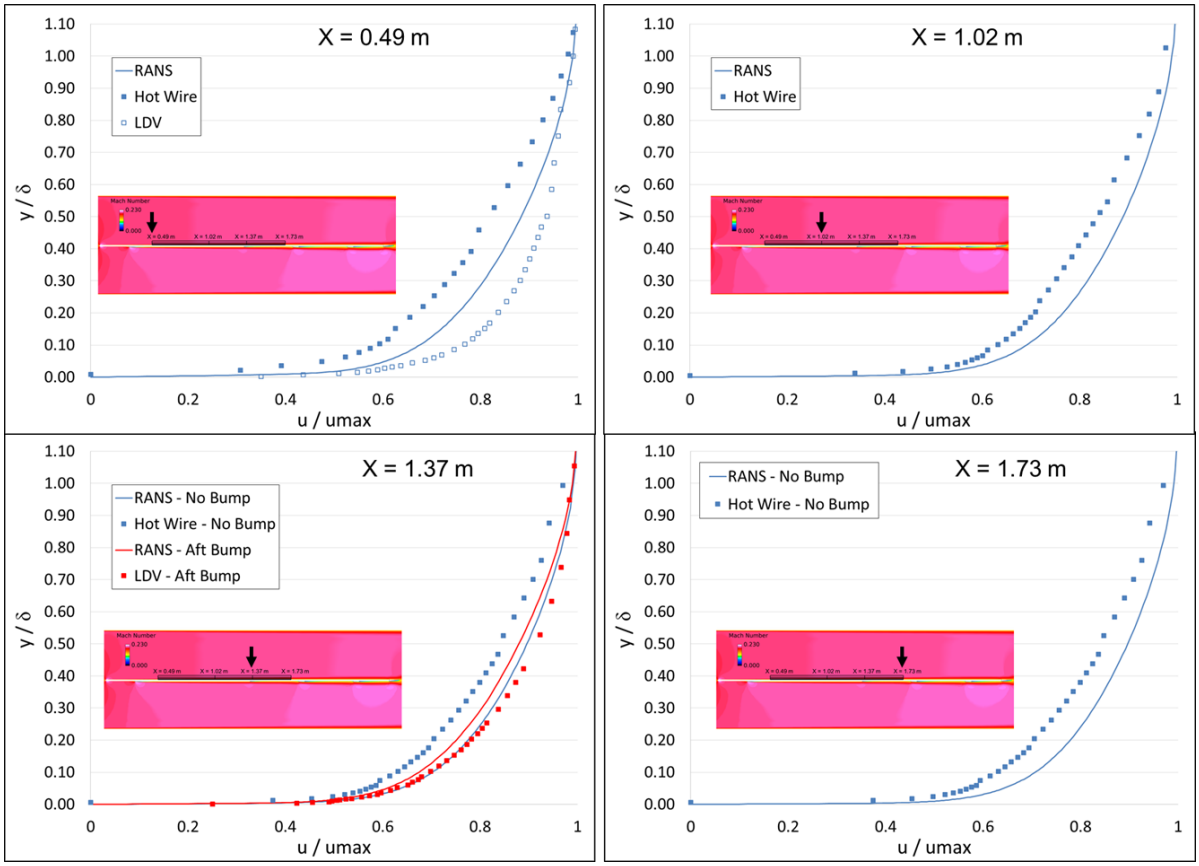

Figure 78: RANS, LDV, and hotwire velocity profiles compared at four stations along the splitter plate.

The sum of observations from Figure 77 through Figure 79 suggests that the RANS profiles are consistent with fully developed, zero pressure gradient, turbulent boundary layers, and that the hotwire measurements differ from this by a seemingly systemic u/umax deficit along the length of the plate. One possible contribution to this deficit is the presence of the hotwire apparatus in the wind tunnel, which is discussed in Section 10.

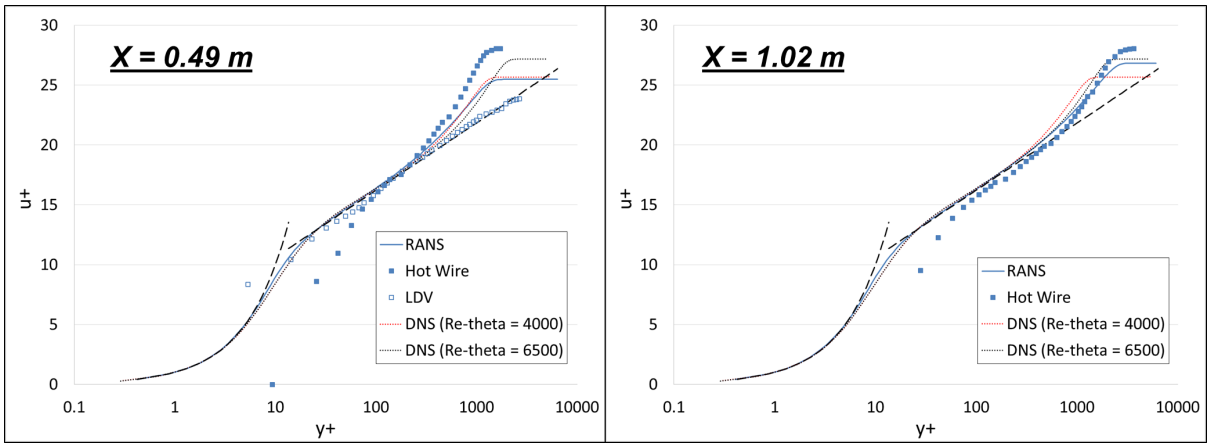

Figure 79: RANS, LDV, DNS, and hotwire velocity profiles compared at the two upstream stations along the splitter plate.

ONR Contract Number N00014-20-2-1002

Finally, comparisons of RANS, DDES, and LDV ahead of the forward bump are presented in Figure 80. At x = 0.33 m RANS and DDES produce nearly identical profiles, but the two predictions deviate increasingly farther downstream on the plate. There is also a distinct and abrupt increase in velocity in all DDES profiles downstream of x = 0.33 m. This increase occurs at a height which correlates with the location at which DDES transitions from RANS to LES, as indicated by the jump from zero to one in LES Width plotted in Figure 80. In order to confirm that the RANS-to-LES transition location is the sole cause of this behavior, a grid was generated where the surface spacing upstream of the bump apex was increased from 0.06" to 0.2". This effectively pushes the transition location farther from the wall, as can be seen from the plots of LES Width in Figure 81 relative to those in Figure 80. The velocity profiles on the coarsened grid, plotted in Figure 81, are very similar between RANS and DDES, which is to be expected upstream of the bump where the boundary layer is steady and attached. The coarse-mesh profiles also lack the sharp velocity increase present on the finer mesh, which confirms that the RANS-to-LES transition is responsible for this behavior.

Ensuring the upstream boundary layer is fully encompassed within the RANS region also has a profound impact on the peak skin friction and separation/reattachment behavior downstream of the apex. Figure 82 shows contours of time-averaged skin-friction coefficient over the forward bump from RANS on the fine grid, and DDES on both the fine and coarse grids. The horizontal black line in each image indicates the spanwise centerline, and the vertical black line is located at measurement station 5 (Figure 74 a). Note that the coarse-grid DDES exhibits some regions of asymmetry downstream of the apex, which is believed to be primarily due to small spanwise non-uniformities in the wall-normal location at which DDES transitions from RANS to LES. Another difference between coarse and fine mesh DDES is that the coarse mesh maintains higher skin friction along the upstream portion of the plate through the bump apex. Based on previous comparisons of skin friction it was shown that fine-mesh DDES under predicted the peak skin friction measured by OFI, therefore it can be said that the

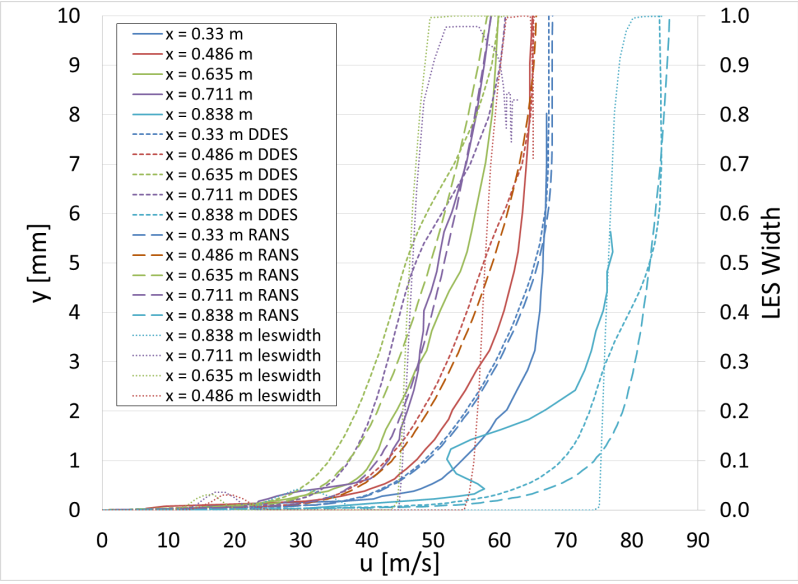

Figure 80: RANS (long dash), DDES (short dash), and LDV (solid line) plotted on the left axis. RANS-to-LES transition location ('LES Width') plotted on the right

coarse upstream grid does a better job of predicting the skin friction between the leading edge of the plate and the bump apex. The other item worth noting is that the separation predicted by the coarse mesh is smaller than that predicted by the fine mesh. The coarse-mesh separation begins farther downstream, reattaches earlier, and is narrower in the spanwise direction. Based on prior comparisons, it was shown that the fine mesh predicted separation earlier, reattachment later, and over a broader spanwise extent than what was measured by PIV. Therefore, it can be said that the coarse mesh more accurately predicts separation and reattachment downstream of the bump apex.

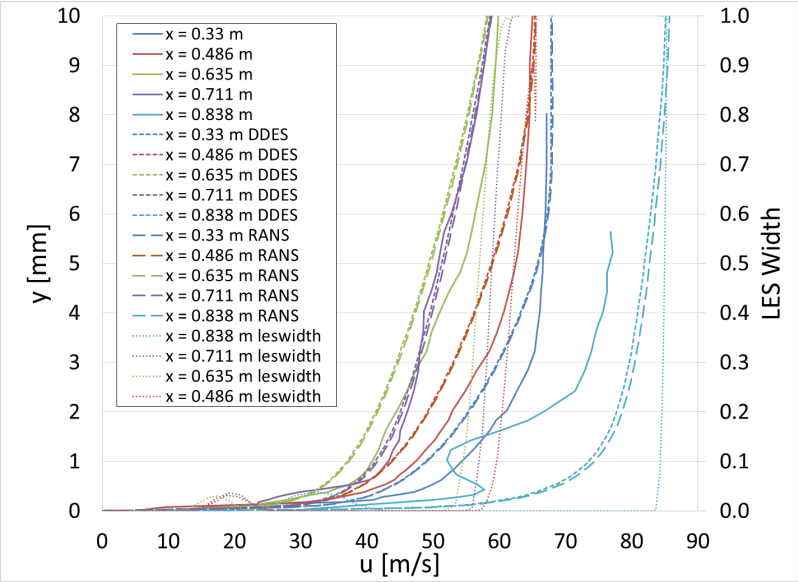

Figure 81: RANS (long dash), DDES (short dash), and LDV (solid line) plotted on the left axis for the coarser plate grid upstream of the bump apex. RANS-to-LES transition location ('LES Width') plotted on the right axis.

These results suggest that in order to produce the most accurate possible prediction with DDES, the boundary layer upstream of the apex needs to be completely shielded within the RANS region. This is not surprising given the sensitivity of the separation to the state of the incoming boundary layer. It was also observed that complete RANS shielding of the boundary layer broke down increasingly the more the surface normal pointed opposite the freestream, as with the forward portion of the bump. This gives a way to assess regions of the geometry, prior to simulating, where a coarser mesh may be needed to attain complete RANS shielding of the boundary layer.

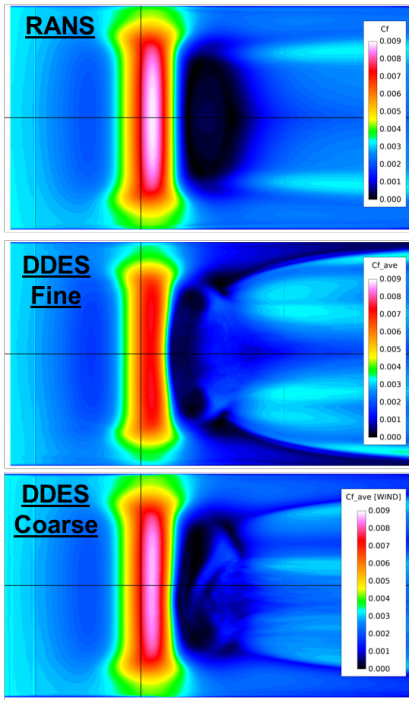

Figure 82: Time-averaged skin-friction coefficient over the forward bump

ONR Contract Number N00014-20-2-1002

9) Embedded Shear-Layer Scaling

The outer-layer scaling described by Schatzman and Thomas (JFM 2017 Vol. 815, pp. 592-642) was applied to mean velocity profiles from Mach 0.1 RANS and DDES simulations at several stations downstream of the bump, where the bump apex was located at 36". The stations considered are depicted in Figure 83, where the values shown for x are at the wall, and the profiles are taken in the wall-normal direction.

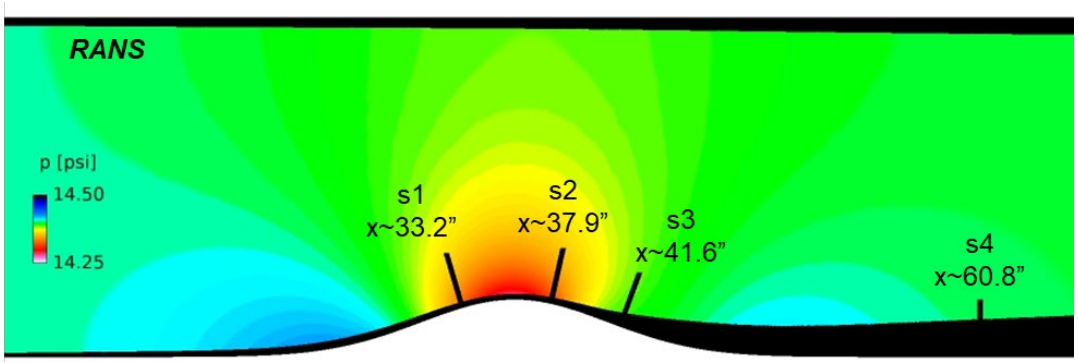

Figure 83: RANS pressure contours on the center plane of a Mach 0.1 simulation. The black overlays near the walls depict regions of significant viscous interaction, e.g., attached and separated boundary layers, and wake flow.

The result of this scaling is shown in Figure 84, where good collapse in the streamwise and wall-normal directions is observed for RANS, particularly downstream of station 2 ('s2') for eta greater than approximately -0.5. Improved collapse in the wall-normal direction is observed for time-averaged DDES profiles at stations 3 and 4, while station 2 remains largely unchanged compared to RANS. These results indicate that the centerline flow in the wake of the bump is dominated by an inflectional instability between the two streamwise-oriented, counter-rotating vortices.

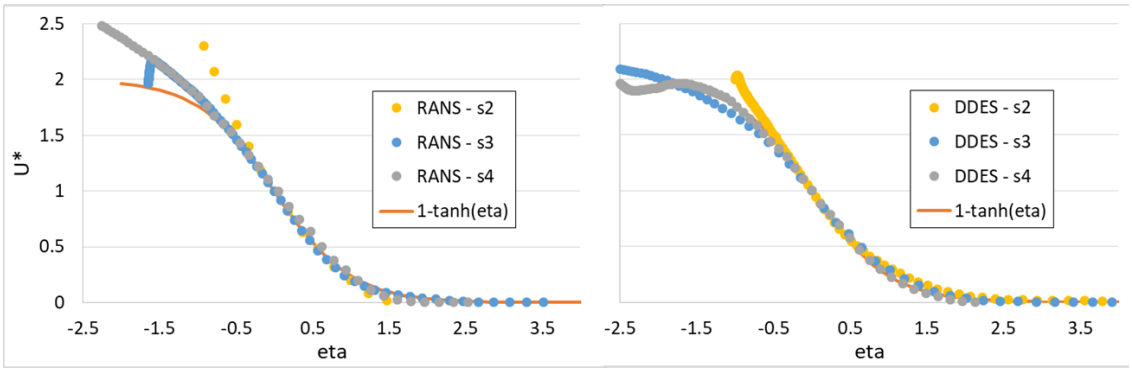

Figure 84: RANS (left) and time-averaged DDES (right) velocity profiles in the adverse pressure gradient downstream of the bump, presented in terms of embedded shear layer scaling.

ONR Contract Number N00014-20-2-1002

10) Potential Impact of Hotwire Apparatus on Measured Velocity

In an attempt to understand some of the differences previously observed between CFD and hotwire measurements on the splitter with no bump, RANS (SA-RC-QCR) simulations were used to quantify the sensitivity of velocity at the measurement location to the presence of the hotwire-measurement apparatus. Figure 85 shows the hotwire geometry (in gray), included in the computational mesh, comprising the traverse, isolator arm, and hotwire probe. The hotwire itself, which is connected between the two prong tips visible in Figure 85-b, is not included in the mesh.

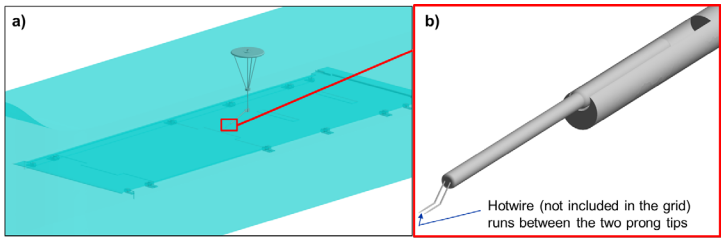

Figure 85: Hotwire geometry (gray) included in computational mesh. a) Complete hotwire apparatus installed above the splitter with no bump, inside the wind tunnel (cyan) at x = 1.37 m and b) the tip of the probe where the hotwire is located.

Simulations with and without the hotwire apparatus were performed at Mach ~ 0.2, Re/m ~ 4.3e6, and Tt ~ 300 K. In Figure 86, Mach-number contours on the center plane of the tunnel show the wake downstream of the apparatus, as well as the influence felt on the upper wall and in the core flow upstream of the apparatus. Although the overall influence of the apparatus is significant, the impact at the measurement location is expected to be small due to the use of the isolator arm, which places the hotwire probe far upstream of the traverse geometry. To more precisely estimate this influence at the measurement location, velocity profiles were extracted from solutions without the hotwire, with the hotwire located 6.22 mm above the plate, and with the hotwire located 2.16 mm above the plate. Mach-number contours along with their grids for these three cases are shown in Figure 87. For the case with the hotwire located 6.22 mm above the plate, care was taken to ensure the grid was as similar as possible to the case with no hotwire. For instance, in Figure 87 it can be seen that the prism layer near the wall as well as the tetrahedra farther from the wall are qualitatively the same between the top and middle images, with the exception of the hotwire presence in the middle image. In the case of the hotwire located closer to the wall (2.16 mm) the prism layer is locally interrupted near the probe tip, but care was taken to ensure that the tetrahedra used to fill the region were similar in size to the adjacent prisms.

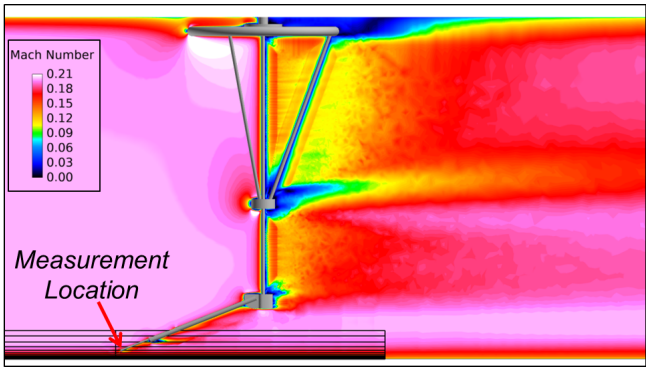

Figure 86: Wake and upstream perturbations caused by the hotwire apparatus. Black grid lines at the bottom represent the interpolation mesh used to extract profiles from the CFD solution.

ONR Contract Number N00014-20-2-1002

When comparing the three contour plots in Figure 87, there is clearly a difference in Mach number near the probe, but at the tip of the prongs where the hotwire is located there is ostensibly no difference with the hotwire apparatus present. To make a more precise assessment, velocity profiles were taken at the same station as the hotwire and compared with the solution where no hotwire is present.

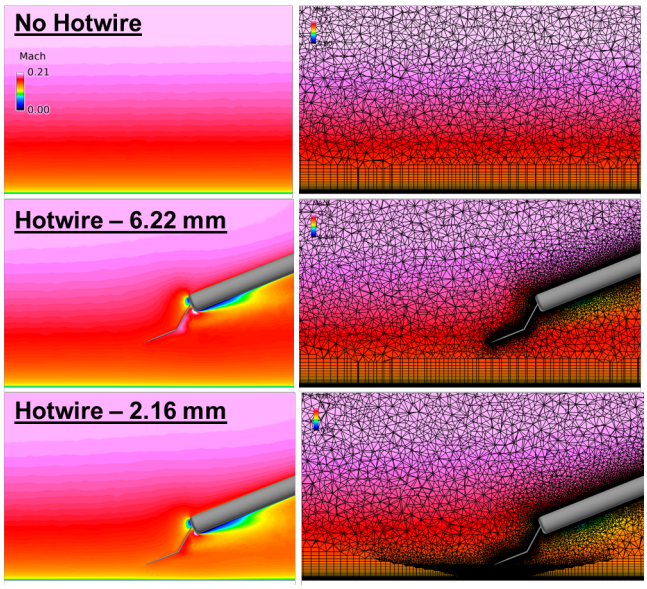

Figure 87: Mach-number contours (left column) and grids (right column) for the simulations without the hotwire (top row), hotwire 6.22 mm above the plate (middle row), and 2.16 mm above the plate (bottom row).

The results with the hotwire 6.22 mm above the plate are shown in Figure 88. The profiles with and without the hotwire are essentially the same below the hotwire location, where a sharp decrease in velocity is observed. Above the hotwire a near-uniform deficit is present in the profile with the hotwire present. Looking very near the hotwire location in the right plot of Figure 88 it is shown that the presence of the hotwire results in a ~1 m/s deficit in the velocity relative to the case with no hotwire. A similar comparison is made in Figure 89 for the case where the hotwire is lowered to 2.16 mm above the plate, and a deficit of ~1 m/s at the hotwire height is once again observed. Based on these results, an additional + 1 m/s was added to the uncertainty bars on the experimentally obtained hotwire measurements, which are plotted in Figure 90. Two other sources of uncertainty which may account for differences between RANS and hotwire, but are not included in the uncertainty bars, are the laminar-to-turbulent transition process in the experiment, and the potential for the hotwire to move from the expected position due to flexure of the hotwire apparatus. Considering the latter, a

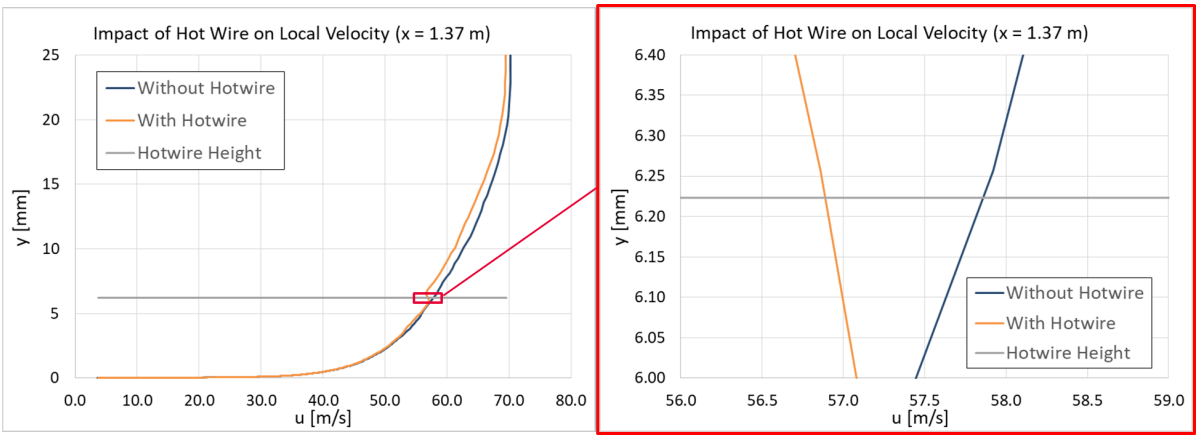

Figure 88: Velocity profiles throughout the boundary layer (left) and focused near the hotwire height (right). Hotwire is located 6.22 mm above the plate.

ONR Contract Number N00014-20-2-1002

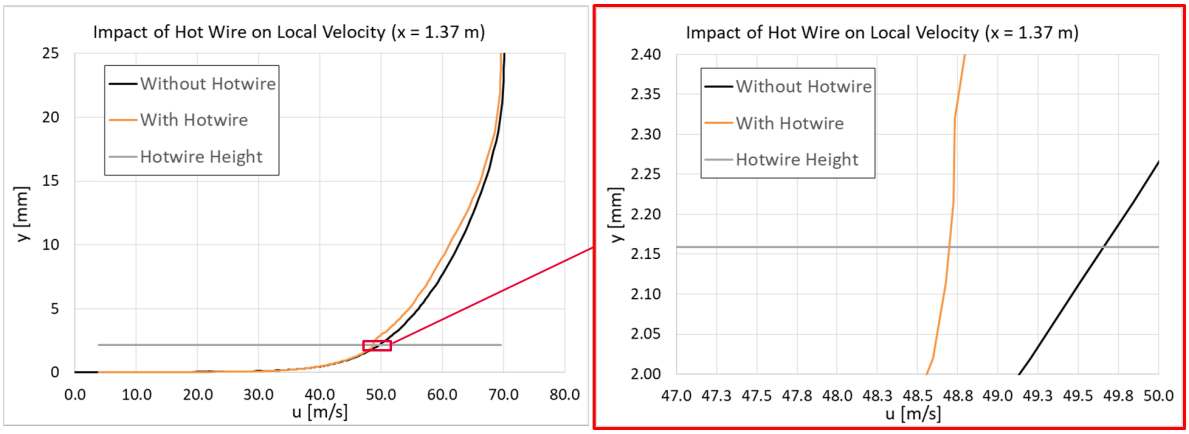

Figure 89: Velocity profiles throughout the boundary layer (left) and focused near the hotwire height (right). Hotwire is located 2.16 mm above the plate.

downward deflection in the hotwire of only 0.2 mm would account for the remaining difference between hotwire and RANS below $y/\delta \sim 0.3$. The issue of transition could be explored numerically in several ways, the least computationally expensive of which would be to prescribe a distance downstream of the leading edge where the turbulence model switches from 'off' to 'on'. The sensitivity of the RANS profile to various 'transition' locations could then be quantified. The drawback of this approach comes from its simplicity and that it neglects the particulars of instability growth and non-linear breakdown to turbulence, and therefore may not adequately represent the trip-induced transition experienced in the wind-tunnel. The only way to fully capture all of this in a simulation is through DNS, which is beyond the scope of the present numerical work.

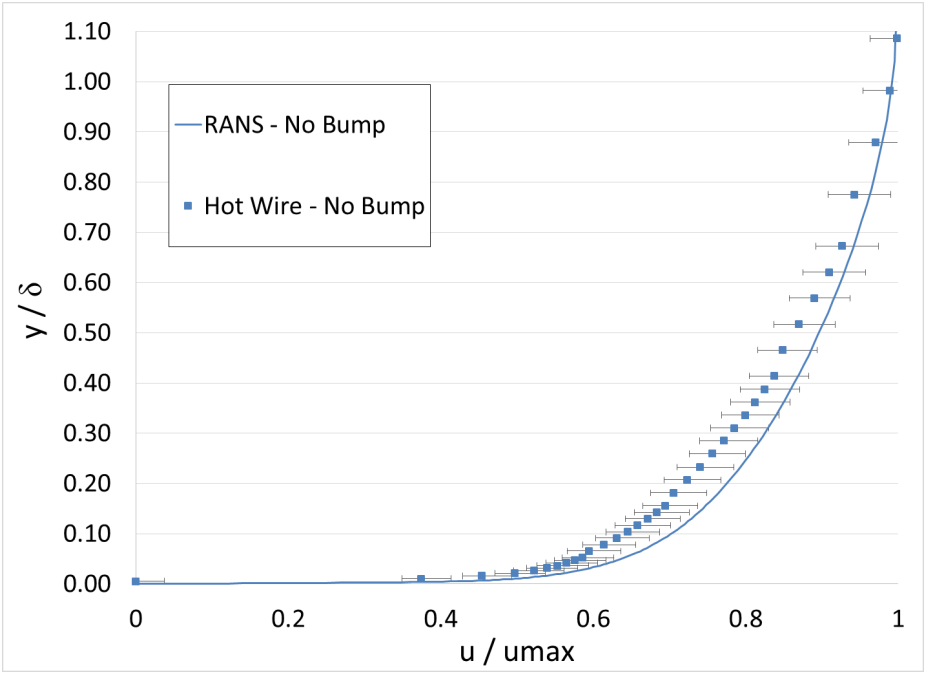

Figure 90: Velocity profiles for the splitter plate with no bump at Mach ~ 0.2.

11) References

1. A. Cary, A. Dorgan, and M. Mani. Toward accurate flow predictions using unstructured meshes. AIAA Paper 2009-3650,2009.
2. Spalart, P. R. and Allmaras, S. R., “A One-Equation Turbulence Model for Aerodynamic Flows,”Recherche Aerospatiale, No. 1, 1994, pp. 5–21.10
3. Shur, M. L., Strelets, M. K., Travin, A. K., and Spalart, P. R., “Turbulence Modeling in in Rotating and Curved Channels: Assessing the Spalart-Shur Correction,” AIAA Journal, Vol. 38, No. 5, 2000, pp. 784–792.11
4. Mani, M., Babcock, D. A., Winkler, C. M., and Spalart, P. R., “Predictions of a Supersonic Turbulent Flow in a Square Duct,” AIAA Paper 2013-0860, January 2013
5. Menter, F. R., “Two-Equation Eddy-Viscosity Turbulence Models for Engineering Applications," AIAA Journal, Vol. 32, No. 8, 1994, pp. 1598-1605.
6. P. R. Spalart, S. Deck, M. L. Shur, and K. D. Squires, “A new version of detached-eddy simulation, resistant to ambiguous grid densities,” Theor. and Comput. Fluid Dyn., 20:181–195, 2006.
7. R. H. Bush and M. Mani, “A two-equation large eddy stress model for high sub-grid shear,” AIAA Paper 2001-2561, 2001.
8. Winkler, C., Dorgan, A., and Mani, M., “A Reduced Dissipation Approach for Unsteady Flows on Unstructured Grids," AIAA Paper 2012-570, January 2012.
9. Marcum, D. L., “Advancing-Front/Local-Reconnection (AFLR) Unstructured Grid Generation," Vol. 1, Computational Fluid Dynamics Review, World Scientific, Singapore, 1998, p. 140.
10. Uzun, A. and Malik, M., “Simulation of a Turbulent Flow Subjected to Favorable and Adverse Pressure Gradients,” AIAA Paper 2020-3061, 2020.